Title
Large-scale network activity and circuit connections in the developing mouse hippocampus

Permalink
https://escholarship.org/uc/item/0cq3r4s2

Author
Shi, Yulin

Publication Date
2014

Peer reviewed|Thesis/dissertation

`

UNIVERSITY OF CALIFORNIA,
IRVINE

Large-scale network activity and circuit connections in the developing mouse hippocampus

DISSERTATION

submitted in partial satisfaction of the requirements
for the degree of

DOCTOR OF PHILOSOPHY

in Biomedical Sciences

by

Yulin Shi

Dissertation Committee:
Associate Professor Xiangmin Xu, Chair
Professor Diane O'Dowd
Professor John Weiss

2014

`

DEDICATION

To

my parents, Xiansheng and Jianan,
my fiancée Meng,
my friends, Jun, Ru, Xiaogang and Sharon,

"It is good to have an end to journey toward; but it is the journey that matters, in the end."

---- Ursula K. Le Guin

`

TABLE OF CONTENTS

Page

`

LIST OF FIGURES

`

`

`

LIST OF TABLES

Page

`

ACKNOWLEDGMENTS

`

CURRICULUM VITAE

EDUCATION

September, 2014 **Ph.D. in Biomedical Science,**
Doctoral Advisor: Dr. Xiangmin Xu, Department of Anatomy and
Neurobiology, UC Irvine.

December 2007 **M.S. Degree in Electrical & Computer Engineering, Purdue Calumet,**

June 2005 **B.S. in Computer Science, Huazhong U. of Science and Technology, China**

RESEARCH POSITIONS

2009-2014 **Graduate Researcher. Department of Anatomy & Neurobiology, UC Irvine**

> *Advisor*: Dr. Xiangmin Xu

- Use combined approaches of electrophysiology, optical stimulation and imaging to map cortical circuit organization and function. [Whole cell recordings, glutamate uncaging, voltage sensitive dyes imaging, hippocampus, network activity, development]

- Apply advanced mathematics and engineering techniques to biological data processing, design and implement large-scale data analysis programs.

2008 **Software Developer, Computational Fluid Dynamics Lab, Purdue University Calumet**

Developed 3D blast furnace modeling and simulating program to assist furnace design.

2006-2007 **Software Developer, Energy Lab, Purdue University Calumet**

Developed portable device software with Visual C++. Design and implement algorithm to identify abnormal electric surge and wave distortion.

TEACHING EXPERIENCE

Fall, 2011, 2012 **Teaching Assistant of Bio 93, DNA to Organism. UC Irvine**
Create innovative activities to help students practice the biological concepts from lecture.

2012 **Teaching Assistant of Bio 94, Organisms to Ecosystem. UC Irvine**
Lead student discussion session to help review and practice concepts from lecture.

2005   *Teaching Assistant of CIS 288, LAN Technology. Purdue University Calumet*
Design lab sessions which give students the hands-on experience of fundamental network operations.

ACADEMIC PUBLICATIONS

Y. Shi, A. Veidenbaum, A. Nicolau, and X.Xu (2014) large scale neural circuit mapping data analysis accelerated with the graphical processing unit (GPU). *Front Neural Circuits* (*In Review)*

E. Ozkan, T. Creson, E. Kramár, C. Rojas, R. Seese, A. Babyan, **Y. Shi**, R. Lucero, X. Xu, J. Noebels, C. Miller, G. Lynch, G. Rumbaugh (2014), Reduced Cognition in Syngap1 Mutants Is Caused by Isolated Damage within Developing Forebrain Excitatory Neurons. *Neuron,* doi: 10.1016/j.neuron.2014.05.015

Y. Shi, T.Ikrar, N.D.Olivas, and X.Xu (2013) Bi-directional global spontaneous network activity immediately precedes the canonical unidirectional circuit organization in the developing hippocampus. *Journal of Comparative Neurology.* doi: 10.1002/cne.23528

S. Ahrar, T. Nguyen, **Y. Shi,** T. Ikrar, X. Xu and E. Hui (2012) Optical Stimulation and Imaging of Functional Brain Circuitry in a Segmented Laminar Flow Chamber. *Lab on a Chip* 13:536-41.

J. Clement, M. Aceti, T. Creson, E. Ozkan, **Y. Shi,** N. Reish, A. Almonte, B. Miller, B. Wiltgen, C. Miller, X. Xu and G. Rumbaugh (2012) Pathogenic SYNGAP1 mutations impair cognitive development by disrupting maturation of dendritic spine synapses. *Cell* 151:709-723.

T. Ikrar, **Y. Shi,** T. Velasquez, M. Goulding and X. Xu (2012) Cell-type specific regulation of cortical excitability through the allatostatin receptor system. *Front Neural Circuits* 6:2. doi:10.3389/fncir.2012.00002

T. Ikrar, N. D. Olivas, **Y. Shi**, and X. Xu (2011) Mapping local inhibitory circuits by laser scanning photostimulation. *Journal of Visualized Experiments* (56), e3109, doi: 10.3791/3109.

Y. Shi, Z. Nenadic and X. Xu (2010) Novel use of matched filtering for synaptic event detection and extraction, *PLoS ONE* 5(11): e15517. doi:10.1371/journal.pone.0015517.

SELECTED PRESENTATIONS

Y. Shi, Local circuit development of hilar mossy cells in the mouse hippocampus, (platform presentation). *Society for Neuroscience 2013 annual meeting, San Diego*

`

Y. Shi, Novel use of matched filtering for synaptic event detection and extraction, (platform presentation). *Society for Neuroscience 2010 annual meeting, San Diego*

Y. Shi, Novel use of matched filtering for synaptic event detection and extraction*, UCI ReMIND emerging Scientists 2011 symposium.*

HONORS

2013   Graduate Fellow Award, HHMI-UCI Teaching Fellows Program, UC Irvine,

2005   Sino funds Fellowship, Purdue University Calumet

2005   Best Paper Award for Senior Design, Huazhong University of Science and Technology

`

Abstract of Dissertation

Large-scale network activity and circuit connections in the
developing mouse hippocampus
By

Yulin Shi

Doctor of Philosophy in Biomedical Sciences

University of California, Irvine, 2014

Associate Professor Xiangmin Xu, Chair

Developing neuronal circuits have many interesting properties; understanding the development process can give us insights on functioning of complex adult neural circuits. One of major features of immature neural circuits is the spontaneous activity, which has also been considered a driving force of circuit maturation. Giant Depolarizing Current (GDP) is the major spontaneous activity at single neuron level of developing hippocampus. What is missing, however, is whether hippocampus has large scale network level spontaneous activity that precedes the formation of mature hippocampal circuits, i.e. unidirectional trisynaptic flow. In chapter 1 of this study, we use Voltage Sensitive Dye Imaging to investigate the initiation and propagation of global network activity (GNA) in developing hippocampus. GNA originates in distal CA3 and propagates both forward to CA1 and backward to DG. Single-cell and local field potential recording confirmed GNA is closely related to neuronal activation. Further, enhancement of local circuit connections to excitatory pyramidal neurons occurs over the same time course as GNA. Thus Bi-directional GNA precedes the maturation of the mouse hippocampal circuit, and it is correlated to maturation of functional circuit

`

connections. To further understand the underlying pathway for back-projection from CA3 to DG in the developing hippocampus, in the study of chapter 2, we use laser scanning photostimulation technique to map synaptic circuit development of mossy cells. We observed major regional sources of circuit excitation and inhibition to hilar mossy cells were changed from CA3 to DG during development. The excitatory back projection from CA3 to mossy cell were greatly reduced in adult hippocampus. Thus, hilar mossy cells can play important role in circuit signal back-propagation from CA3 to DG. In chapters 3 and 4, we demonstrate an innovative technology which automatically detects and extracts EPSC and IPSC events in electrophysiological recording. We also present our GPU based computing system and our modification of the previous technology to utilize the power of GPU computing. GPU computation could greatly improve the speed of computation while retaining data precision. Taken together, my dissertation studies contribute new and important knowledge to the field of hippocampus circuit studies, using our newly developed techniques.

`

Introduction

Hippocampal circuitry has been the center of neuroscience research to understand learning and memory, and temporal lobe epilepsy; considerable efforts have been focused on its development and organization. The hippocampus has a distinctive trisynaptic organization that is strongly feed-forward in the directionality of its information flow (i.e., dentate gyrus, DG-> CA3-> CA1), which contributes to both normal function and pathology. There have been considerable efforts to understand the developmental processes that lead to the adult hippocampal circuit organization. Spontaneous network activity in many developing neural circuits, including the hippocampus, contribute to circuit formation in many important ways (Behrens et al., 2005; Gonzalez-Islas and Wenner, 2006; Ben-Ari et al., 2007). In the early developing hippocampus, spontaneous-recurring network events termed giant depolarizing potentials (GDPs) (Ben-Ari et al., 1989; Ben-Ari et al., 2007) are well known, and GDPs are generally believed to be GABAergic events mediated by $GABA_A$ receptor transmission (Ben-Ari, 2002; Ben-Ari et al., 2007) (however, see (Bolea et al., 1999; Sipila et al., 2005)). Similar to GDPs observed in vitro, spontaneous sharp waves (SPWs) visible in extracellular field potential recordings also have been observed in the hippocampus of neonatal and adult rats in vivo (Buzsaki, 1986; Leinekugel et al., 2002; Buhl and Buzsaki, 2005) – some of these researchers suggest that SPWs and GDPs are essentially the same phenomena measured under different experimental conditions. GDPs or SPWs recorded at the microscopic level indicate that spontaneous activity is important for developing hippocampus; however, studies to date have not provided a macroscopic network-level view of the spatial and temporal dynamics of spontaneous

1

`

neural activity, and the spontaneous network activity in the developing hippocampus immediately precedes the unidirectional trisynaptic circuit organization that characterizes adult hippocampus.

Underlying the spontaneous network activity are the immature hippocampal circuitry, comprising dentate granule cells, hilar mossy cells, CA3 and CA1 pyramidal neurons. In mature circuits, these neurons form complex recurrent network that are innervated by hippocampal interneurons. So far the developing neural circuitry in hippocampus was not fully understood, especially during the period in which the spontaneous network activity is still active. Investigation of the connection development of these excitatory neurons might help understand the initiation and propagation of spontaneous network activity, and also provide more information for epileptogenesis. Within this context, we used a set of experiments with a multidisciplinary approach including fast voltage-sensitive dye (VSD) imaging of neuronal activity and laser scanning photostimulation by the uncaging of neurotransmitters to examine the developing circuit activity and connections in slice preparations of mouse hippocampus. This combined approach allows for high spatiotemporal-resolution imaging of the entire circuit including the dentate gyrus (DG), CA3 and CA1, and also enables effective mapping of local functional circuit connections. We have identified the spontaneous network activity we term Global Network Activation (GNA) in the developing mouse hippocampal slices measured macroscopically by fast VSD imaging. Then we continued to record from CA3 pyramidal neurons and hilar mossy cells at different developmental ages to map developmental changes of circuit connections using laser scanning photostimulation-based techniques. To facilitate data processing and analysis for the

2

large scale circuit mapping studies, we also developed new computer algorithms and tools in aiding data analysis and quantification. This series of studies are described in my dissertation including the subsequent four chapters.

In chapter 1 (published as a research article, 'Shi et al, 2010'), fast voltage-sensitive dye(VSD) imaging of neuronal activity will be used to identify and characterize spontaneous network activity in developing hippocampus slices at different ages (postnatal days 1-18 (P1-P18)) and the timing of spontaneous network activity will be examined in relation to the development of mature circuit connectivity. We further use Laser scanning photostimulation and whole cell recording to examine developmental enhancement of local synaptic connections to excitatory neurons of CA3 at different time points (P2-P14).

In Chapter 2, we further test the hypothesis that the circuit connections of mossy cells develop as the hippocampus maturation. As the formation of unidirectional trisynaptic circuits, the back-projection from CA3 to mossy cell should be greatly reduced. The photostimulation approach will be used to examine local circuit connections to mossy cells in the hilus at different developmental ages (P6-P7, P13-P14, and p21-p28). We found that mossy cell received most excitatory input from DG at P14, and slightly less at P21-P28. The input from CA3 and Hilus decreases as the animal ages. Similarly, inhibitory input from DG, Hilus and CA3 to Mossy cell is weak at P7. The input strength increased significantly at P14 and goes down at P21-28. DG provides dominant inhibition comparing to other areas.

In Chapter 3 (published as a research article 'Shi et al, 2013'), we tested the hypothesis that the synaptic events (EPSCs and IPSCs) can be detected through

`

automatic software processing, which expedited the photostimulation data processing significantly. We developed a novel matched filtering technique which enables dependable automatic detection of synaptic events with minimal human supervision. The current technique has overcome the limitations of previously described threshold and template comparison techniques in detection of complex evoked synaptic signals with variable amplitudes and superimposed events. An important innovation of our technique is utilization of a bank of matched filters for the detection stage, which offers several advantages (including improved sensitivity and specificity) over previous techniques of template comparison.

In Chapter 4, we further improve the software in chapter 3 with cutting edge GPU-computing technology. Modern neuroscience studies produce large amount of data and require intensive computation for post-hoc processing and analysis. In this chapter, we designed and implemented a cost-effective desktop computer system for accelerated experimental data processing with recent GPU computing technology. In addition, we show how GPUs can be effectively adapted to improve the performance of commercial image processing software such as Adobe Photoshop. The experimental results show that GPU enabled computation enhances our ability to process large-scale data sets derived from neural circuit mapping studies, allowing for significantly increased processing speeds while retaining data precision and minimizing programming effort. To our best knowledge, our work is the first demonstration in this subfield of neuroscience.

Finally, in Chapter 5, I provide concluding remarks regarding the circuit development of hippocampus and describe the future directions that should be pursued

`

to better understanding the relation between spontaneous activity and circuit

maturations. Also, I review the techniques described in chapter 3 and 4 and discuss

their further applications.

Chapter 1:
Bi-directional global spontaneous network activity precedes the canonical unidirectional circuit organization in the developing hippocampus

Spontaneous network activity is believed to sculpt developing neural circuits. While spontaneous giant depolarizing potentials (GDPs) were first identified with single cell recordings from rat CA3 pyramidal neurons, here we identify and characterize a large-scale spontaneous network activity we term Global Network Activation (GNA) in the developing mouse hippocampal slices which is measured macroscopically by fast voltage-sensitive dye imaging. The initiation and propagation of GNA in the mouse is largely GABA-independent and dominated by glutamatergic transmission via AMPA receptors. Despite the fact that signal propagation in the adult hippocampus is strongly unidirectional through the canonical trisynaptic circuit (dentate gyrus, DG to CA3 to CA1), spontaneous GNA in the developing hippocampus originates in distal CA3 and propagates both forward to CA1 and backward to DG. Photostimulation-evoked GNA also shows prominent backward propagation in the developing hippocampus from CA3 to DG. Mouse GNA is strongly correlated to electrophysiological recordings of highly localized single cell and local field potential events. Photostimulation mapping of neural circuitry demonstrates that the enhancement of local circuit connections to excitatory pyramidal neurons occurs over the same time course as GNA, and reveals the underlying pathways accounting for GNA backward propagation from CA3 to DG. The disappearance of GNA coincides with a transition to the adult-like unidirectional circuit organization at around two weeks of age. Taken together, our findings strongly suggest a critical link between GNA activity and maturation of functional circuit connections in the developing hippocampus.

`

Introduction

The hippocampal circuit underlies learning and memory processes, and mediates

pathological conditions such as temporal lobe epilepsy. The hippocampus has a

distinctive trisynaptic organization that is strongly feed-forward in the directionality of its

information flow (i.e., dentate gyrus, DG-> CA3-> CA1), which contributes to both

normal function and pathology. There have been considerable efforts to understand the

developmental processes that lead to the adult hippocampal circuit organization.

Spontaneous activity in many developing neural circuits, including the hippocampus,

contributes to circuit formation. In the early developing hippocampus, GABA actions are

depolarizing and excitatory, coinciding with spontaneous-recurring network events

termed giant depolarizing potentials (GDPs) (Ben-Ari *et al.*, 1989; Ben-Ari *et al.*, 2007).

GDPs were initially identified with single cell recordings from CA3 pyramidal neurons in

slices of neonatal rats; further studies have continued mostly in rat hippocampal

preparations with single cell and local field electrophysiological recordings and Ca^{2+}

imaging methods (Ben-Ari et al., 1989; Bonifazi et al., 2009; Garaschuk et al., 1998;

Leinekugel et al., 1998; Leinekugel et al., 1997). Propagating network events related to

GDPs also have been examined using fast voltage-sensitive dye imaging in rat

hippocampal slices (Bolea *et al.*, 2006). GDPs are believed to be GABA dependent

events mediated by $GABA_A$ receptor transmission (Ben-Ari, 2002; Ben-Ari et al., 2007;

Ben-Ari et al., 1997) (however, see (Bolea et al., 1999; Sipila et al., 2005; Xie et al.,

1994)). Similar to GDPs observed *in vitro*, spontaneous sharp waves (SPWs) visible in

extracellular field potential recordings also have been observed in the hippocampus of

neonatal and adult rats *in vivo* (Buhl and Buzsaki, 2005; Buzsaki, 1986; Leinekugel et

`

al., 2002) – some of these researchers suggest that SPWs and GDPs are essentially the same phenomena measured under different experimental conditions. GDPs or SPWs recorded at the microscopic level indicate that spontaneous activity is important for developing hippocampus; however, studies to date have not provided a macroscopic network-level view of the spatial and temporal dynamics of spontaneous activity or addressed the relative timing compared with the development of mature circuit connectivity.

To provide a macroscopic global view of these processes in developing hippocampus, we combined fast voltage-sensitive dye (VSD) imaging of neuronal activity and laser photostimulation by the uncaging of neurotransmitters to examine the developing circuit activity and connections in slice preparations of mouse hippocampus. This approach allows for high spatiotemporal-resolution imaging of the entire circuit including the dentate gyrus (DG), CA3 and CA1, along with functional mapping of circuit connections. Herein, we describe spontaneous global network activation (GNA) measured by VSD imaging, which propagates from distal CA3 to DG as well as to CA1 in the trisynaptic circuitry. Spontaneous and evoked mouse GNA have similar spatiotemporal properties as assessed by VSD imaging and laser photostimulation in the developing circuitry. Bi-directional GNA precedes the maturation of the mouse hippocampal circuit, as GNA disappears immediately before the emergence of the unidirectional trisynaptic circuit organization that characterizes adult hippocampus.

Methods

Slice preparation and experimental conditions

`

All animals were handled and experiments were conducted in accordance with the procedures approved by the Institutional Animal Care and Use Committee at the University of California, Irvine. Seventy-five C57/B6 background mouse pups (either sex) of postnatal (P) day 1 (P1) – P18 were used for the experiments.

Hippocampal slices of 400 μm thick were cut at the angle optimized to conserve the intrahippocampal axonal projections (Bischofberger *et al.*, 2006), in well oxygenated (95% O2-5% CO2), ice-cold sucrose-containing cutting solution (in mM: 85 NaCl, 75 sucrose, 2.5 KCl, 25 glucose, 1.25 NaH_2PO_4, 4 $MgCl_2$, 0.5 $CaCl_2$, and 24 $NaHCO_3$) or in the artificial cerebrospinal fluid (ACSF) (in mM: 126 NaCl, 2.5 KCl, 26 $NaHCO_3$, 2 $CaCl_2$, 2 $MgCl_2$, 1.25 NaH_2PO_4, and 10 glucose) with a broad-spectrum excitatory amino acid antagonist kynurenic acid (0.2 mM). On average, one or two morphological intact slices (as illustrated at the horizontal plates of 147-150 in (Paxinos and Franklin, 2001)) between dorsal and ventral hippocampus from each hemisphere was used for experiments. For VSD imaging experiments, slices were first incubated in the cutting solution for 30 minutes at 32°C, and then transferred for dye staining at room temperature (22°C) for 1 hour in oxygenated ACSF containing 0.12 mg/ml of the absorption voltage-sensitive dye, NK3630 (Kankoh-Shikiso Kenkyusho Co., Japan), then maintained in regular ACSF before use. We used standard open recording chambers which maintained slice health and viability well, as evidenced by measurement of GNA activity for periods lasting more than 6 hours. A majority of imaging experiments were conducted at room temperature. Further experiments were conducted at 32 °C with an in-line solution heater (Warner Instruments, Hamden, CT).

9

`

The characteristics of spontaneous and evoked network activity did not differ at different temperatures. The data obtained were pooled together for analysis.

Voltage-sensitive dye imaging

Our overall system of electrophysiological recordings, photostimulation and imaging was described previously (Xu *et al.*, 2010). Unless otherwise specified, optical recording of VSD signals was performed under the 4x objective with a sampling rate of 4.4 ms per frame (frame resolution 88 (w) x 60 (h) pixels). The field of view covered the area of 1.28 x 1.07 mm^2 with a spatial resolution of 14.6 x 17.9 µm^2/pixel. To image spontaneous network activity, 5-10 sessions (9 trials per session) were conducted with 3 minutes of off-illumination intervals between sessions. For each trial, the VSD imaging duration was 2000 frames (i.e., 8.8 seconds) with an inter-trial interval of 12 seconds (i.e., 8.8 seconds for data recording plus 3.2 seconds for saving data). Each session lasts for 9 x 12 seconds (108 seconds total). Due to the known concern of dye photo-toxicity from prolonged illumination, we chose not to image stained slices continuously, and instead we used spaced sessions to detect GNA events for a total duration of up to 18 minutes, which is sufficient in terms of total acquisition times. We measured the total GNA events from all these sessions against the total imaging time to derive the GNA frequency (events per minute). For the imaging of photostimulation-evoked activity, MNI-caged glutamate (Tocris Bioscience, Ellisville, MO) or CNB-caged GABA (Invitrogen, Carlsbad, CA) was added to the ACSF at 0.2 mM. A UV laser unit (DPSS Lasers, Santa Clara, CA) was used to generate 355 nm pulses (e.g., 1 ms, 20 mW) for glutamate or GABA uncaging. VSD imaging of photostimulation-evoked activity was triggered and synchronized with laser photostimulation.

Figure 1.1
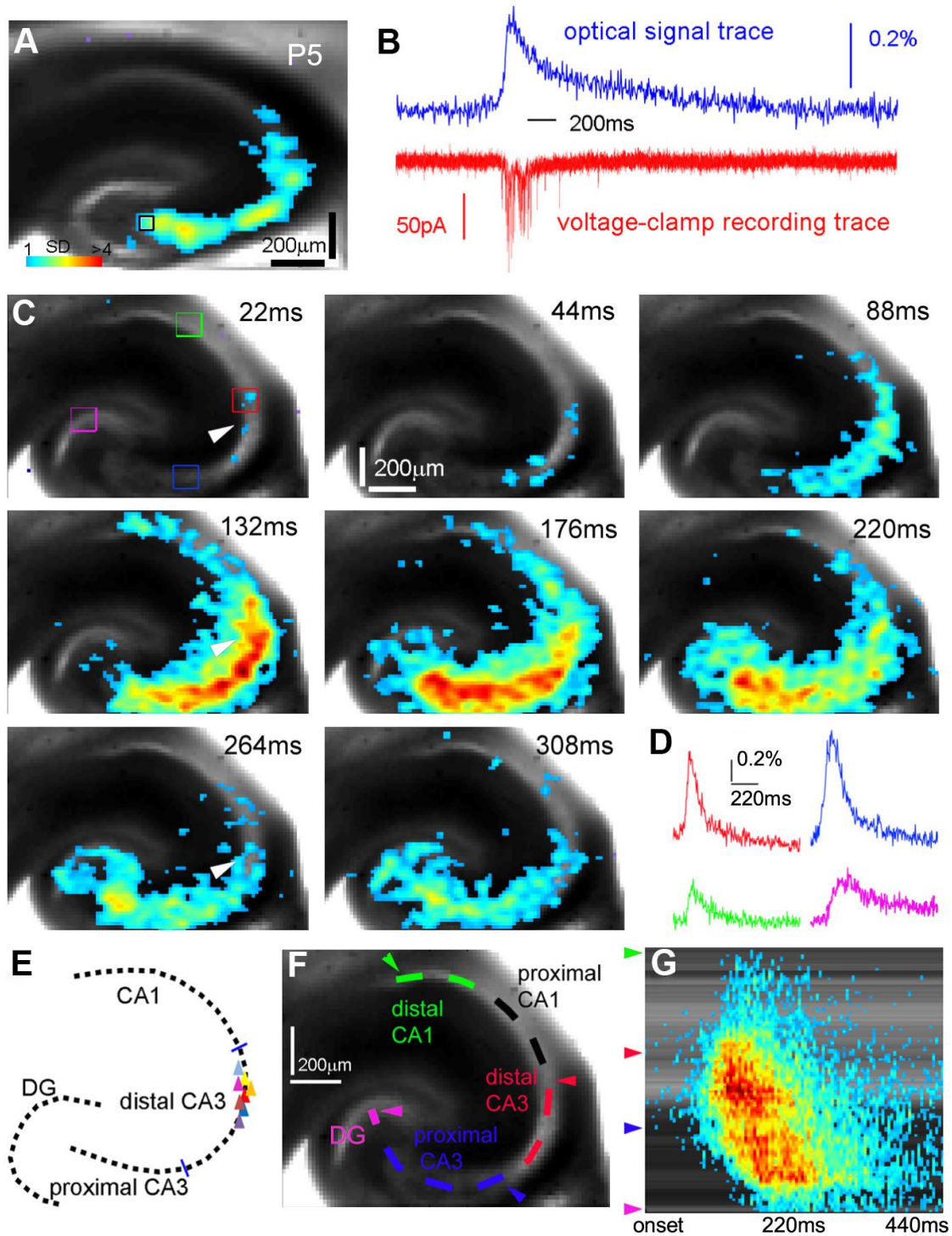
Figure. 1.1. Spontaneous global network activation (GNA) in the developing mouse hippocampus exhibits both strong forward and backward propagation from distal CA3. A-B. Voltage-sensitive dye (VSD) imaging and simultaneous whole

cell recording indicate that GNA is tightly correlated with single neuronal activity. The measurements were taken from a proximal CA3 site as indicated by the small black square. The VSD image frame in **A** was plotted beginning at the peak of excitatory synaptic input to the recorded neuron. Color-coded activity is superimposed on the background slice image. The color scale codes VSD signal amplitude expressed as SD (standard deviation) multiples above the mean baseline. **B** shows the aligned optical signal trace (VSD signal in the percent change of pixel intensity [ΔI/I %]) and voltage-clamp recording trace. **C**. Time series data from VSD imaging of spontaneous GNA. The white arrowhead indicates the initiation site in distal CA3. **D**. The time courses of VSD signal from the regions of interest indicated by the colored rectangles in **B** are plotted from GNA onset. **E**. Schematic distribution of spontaneous GNA initiation zones (8 representative slices). Each triangle represents one slice sample. **F-G**. Space-time analysis of GNA propagation shown in **B**. **F** shows an analysis curve aligned with the hippocampal circuitry in the slice image, and **G** is the space-time map with the y-axis indicating the location along the analysis curve shown in **F** (e.g., the green, red, blue and pink arrowheads correspond to those sites indicated in **F**) and with the x-axis denoting the time progression from the activity onset.

VSD signal amplitudes were originally measured by the percent change in pixel light intensity (ΔI/I %), and expressed as standard deviations (SD) above the mean baseline signal for display and quantification. The activated pixel was empirically defined as the pixel with the amplitude ≥ 1 SD above the baseline (equivalent to the detectable signal level in the original VSD maps of Δ*I/I* %). VSD images were smoothed by convolution with a Gaussian spatial filter (kernel size: 5 pixels; standard deviation (σ): 1 pixel) and a Gaussian temporal filter (kernel size: 3 frames; δ: 1 frame). In the present study, single-trial VSD signals were of sufficiently high amplitudes and could be discerned from background noise; no averaging over multiple trials was used for data presentation unless specified. Images were displayed and analyzed using custom-made MATLAB programs. To quantify VSD response strength of spontaneous or photostimulation-evoked GNA, the average number of activated pixels and average response amplitude within the defined window of analysis were measured for each trial.

`

We follow the basic nomenclature of Lorente de Nó (1934) and Ishizuka et al. (1990) for hippocampal subfields. We do not distinguish the CA2 region as it is not well defined in early postnatal hippocampal slices (Grove and Tole, 1999; Tole et al., 1997), however, the presumptive CA2 identified in some slices appears to be part of the GNA initiation zone. The terms of proximal (nearer the dentate gyrus) and distal (further away from the dentate gyrus) are used to designate positions along the transverse axis of the CA3 (Ishizuka et al., 1990). The mid-line of the fimbria divides CA3 into the distal and proximal portions.

For statistical comparisons across more than two groups, we used the Kruskal-Wallis test (nonparametric 1-way ANOVA) and the Mann-Whitney U test for group comparisons. Alpha levels of $p \leq 0.05$ were considered significant. All the values were presented as mean ± SE.

Electrophysiology and laser scanning photostimulation

For electrophysiology and photostimulation mapping experiments, the slices did not go through the dye staining unless specified. To perform whole cell recordings, cells were visualized at high magnification (60× objective) and patched with glass electrodes of 4–6 MΩ resistance that were filled with an internal solution containing (in mM) 126 K-gluconate, 4 KCl, 10 HEPES, 4 ATP-Mg, 0.3 GTP-Na, and 10 phosphocreatine (pH 7.2, 300-305 mOsm). The internal solution also contained 0.1% biocytin for cell labeling and morphological identification. The glass electrodes with the same resistance parameters as noted above were also used for extracellular field potential recording. Raw electrophysiological data were digitized at 10 kHz, and stored on data acquisition computers. Once stable whole cell recordings were achieved with good access

13

`

resistance (usually <20 MΩ), the microscope objective was switched from 60× to 4× for

laser scanning photostimulation (LSPS).

Figure 1.2

A — GNA event frequency
B — Duration
C — Peak amplitude
D — Propagation speed
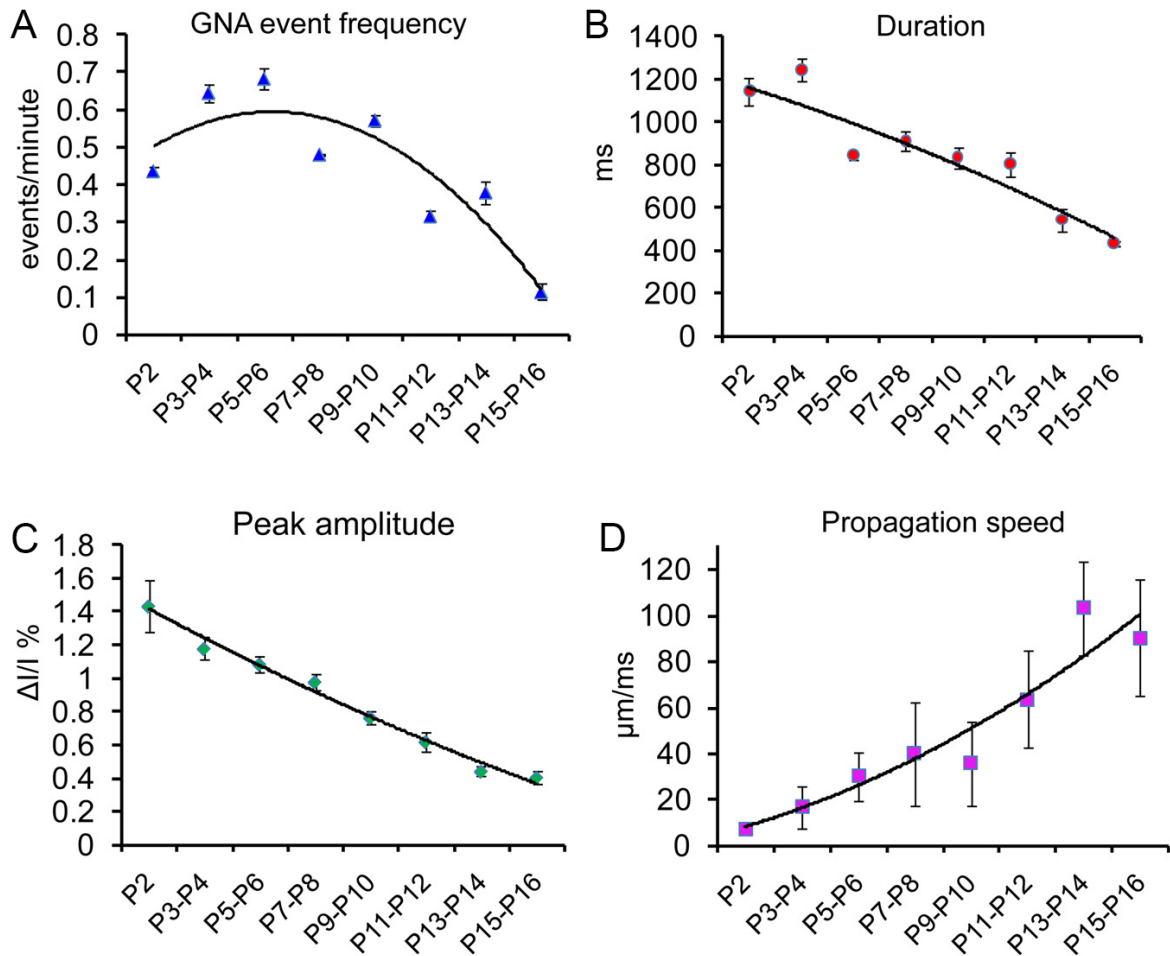
Figure. 1.2. Developmental changes of GNA. **A**, **B**, **C** and **D**. Average GNA event frequency, duration, peak amplitude and propagation speed during P2-P16, respectively. The curves are polynomial-fits through data points (each measured from several sampled events from 4-5 slices). The values represent mean ± SE.

The LSPS method has been previously used in the neocortex and hippocampus

(Brivanlou et al., 2004; Dantzker and Callaway, 2000; Shepherd et al., 2005; Weiler et

al., 2008; Xu and Callaway, 2009). Under our experimental conditions, only neurons

`

located within ~100 μm of the site of photostimulation fired action potentials. Therefore,

laser photostimulation allowed high spatial-resolution activation of action potentials

restricted to excitatory or inhibitory neurons close to the location of each

photostimulation site. It also could be inferred that under our LSPS mapping conditions

and within our analysis window (see below), evoked synaptic currents reflect direct

connections onto the recorded cell from the cells at or near the photostimulation sites in

different hippocampal subfields. During mapping experiments, photostimulation was

usually applied to 16×16 patterned sites (with an inter-site space of 60-80 μm^2) covering

the whole hippocampus in a nonraster, nonrandom sequence to avoid revisiting the

vicinity of recently stimulated sites; whole-cell voltage-clamp recordings were made

from the recorded neurons to measure photostimulation-evoked excitatory postsynaptic

current (EPSC) responses at the holding potential between -60 and -65 mV, which was

based upon the empirically determined GABAergic reversal potentials at the

developmental ages tested. After EPSC measurements, whenever it was possible, the

recorded cells were also voltage-clamped at -10 - -20 mV to detect photostimulation-

evoked inhibitory postsynaptic current (IPSC) responses. In separate experiments, the

recorded neurons were held at +5 mV in voltage clamp mode with cesium-containing

internal solution to map IPSCs.

 Photostimulation can induce two major forms of excitatory responses (Shi et al.,

2010; Xu and Callaway, 2009): (1) direct glutamate uncaging responses (direct

activation of the recorded neuron's glutamate receptors); and (2) synaptically mediated

responses (EPSCs) resulting from the suprathreshold activation of presynaptic

excitatory neurons. Responses within the 7 ms window from laser onset are considered

`

direct. Synaptic currents with such short latencies are not possible because they occur

before the generation of action potentials in photostimulated neurons. To exclude direct

responses, candidate EPSCs with their arrival times occurring within the direct response

window (within 7 ms of the laser onset) are dismissed. Similarly, for inhibitory

postsynaptic responses, we only included actual presynaptic inhibitory input (resulting

from somatic firing of inhibitory neurons at stimulated locations) to construct inhibitory

input maps. A new technique that combines the design of a bank of approximate

matched filters with the detection and estimation theory was implemented for automated

detection and extraction of photostimulation-evoked EPSCs or IPSCs (Shi *et al.*, 2010).

As for individual map construction, input measurements from different stimulation sites

were assigned to their corresponding anatomical locations in the hippocampus; and

color-coded maps of average input amplitude, the number of events, and response

latency per site were plotted to illustrate the overall input pattern to the recorded cell.

The input amplitude/strength of each stimulation site was measured by the sum of

individual EPSCs or IPSCs from each photostimulation site with the baseline

spontaneous response subtracted, and then normalized by the analysis window of 150

ms after photostimulation. This average integrated value was expressed in pico

amperes (pA) for the analysis window. To quantitatively compare input strength and

connections across cell groups, we measured the total sum of the ESPC or IPSC input

strength across the map sites for individual cells, and assessed the extent of synaptic

connections by measuring the number of stimulation locations providing synaptic input

in the mapping region. We also compared EPSC or IPSC latencies of data maps

across the cell groups.

`

After all physiological assays were completed, the brain slices were fixed in 4% paraformaldehyde in phosphate buffered saline (PBS) overnight and then transferred to 30% sucrose solution in PBS. All the slices were stained for 4'-6-Diamidino-2-phenylindole (DAPI) (Sigma-Aldrich, St. Louis, MO) to identify hippocampal subfields. Those slices with whole cell recording experiments were stained against biocytin with 1:1000 Cy3-conjugated streptavidin (Jackson ImmunoResearch, West Grove, PA), and cell morphology was examined with confocal or epi-fluorescent microscopy. Excitatory pyramidal neurons in CA3, hilar mossy cells and DG granule cells were targeted for recordings based upon their distinguishable morphology in living slices under DIC microscopy and confirmed by post-hoc analysis of their intrinsic spiking patterns and morphological features revealed by the biocytin staining.

Results

Spontaneous global network activation (GNA) in the developing mouse hippocampus

We examined mouse hippocampal circuit activity in slice preparations at different ages (postnatal days 1-18 (P1-P18)) with VSD imaging, which monitors neuronal activity spanning DG and hippocampus simultaneously (Xu *et al.*, 2010). We found that spontaneous GNA exhibits a specific anatomical origin at distal CA3, and it starts with sparse activation at the initiation site and gradually evolves into large-scale, bi-directional propagating network activity (Fig.1.1). GNA exhibits rather uniform patterns across different occurrences in the same slices. Simultaneous voltage clamp recordings verified that individual cells receive excitatory synaptic input that correlates with optical measurement (Fig.1.1A-B). GNA initiation is empirically determined by

17

patches of coherent activation across 5 consecutive VSD image frames with its signal

amplitude at least one standard deviation above the preceding 50 ms baseline activity.

As per the color scale, warmer colors indicate greater excitation. The initiation (first 20-

30 ms) appears to arise from activation of a small number of neurons within the area of

80 μm x 80 μm (Fig. 1.1C, E). GNA propagation starts after 40-50 ms, and produces

strong excitatory activity within 300-500 ms throughout the hippocampal circuitry,

propagating to proximal CA3, then to the hilus and the fascia dentate of the dentate

gyrus (DG), as well as to CA1 (Fig. 1.1C, D). The propagation pattern of GNA could

also be well illustrated in space-time analysis of the network activity (Fig. 1.1F-G); there

is a U-shape like activity spread from the point of origin at distal CA3, indicating bi-

directional propagation.

Mouse GNA appears robustly at P2 and event frequency peaks at P5-P6 (Fig.

1.2A). GNA event frequency of the first postnatal week is 0.66 ± 0.075 events per

minute (N= 12 slices of P2-P7), which is considerably lower than an average of 5-6

events/minute for rat GDPs identified by intracellular recordings (Ben-Ari *et al.*, 1989;

Bolea *et al.*, 1999), suggesting a potential species difference and a possibility that single

cell events may not correspond to global scale events. GNA events occur significantly

less often at older postnatal days (Fig. 1.2A) with the average rate of 0.36 ± 0.072

events per minute between P8-P16 (N= 19 slices), which differs significantly from P2-P7

(p <0.01). GNA is only detected in 40%, and 20% of the more developmentally mature

slices tested at P10-P12, and P13-P16, respectively, compared to 80% of the slices for

P2-P9. No GNA events are detected beyond P18. Overall, there is no discernible trend

for clustered occurrences by trial, as we examined a scatter plot of GNA occurrences

`

versus trial numbers from selected sessions in P3-P8 slices (N = 88 sessions from 8

slices). The average numbers of events per session for a given slice was 0.92 ± 0.10,

with its inter-session standard deviation of GNA occurrence ranging from 0.7-1.2.

Figure 1.3
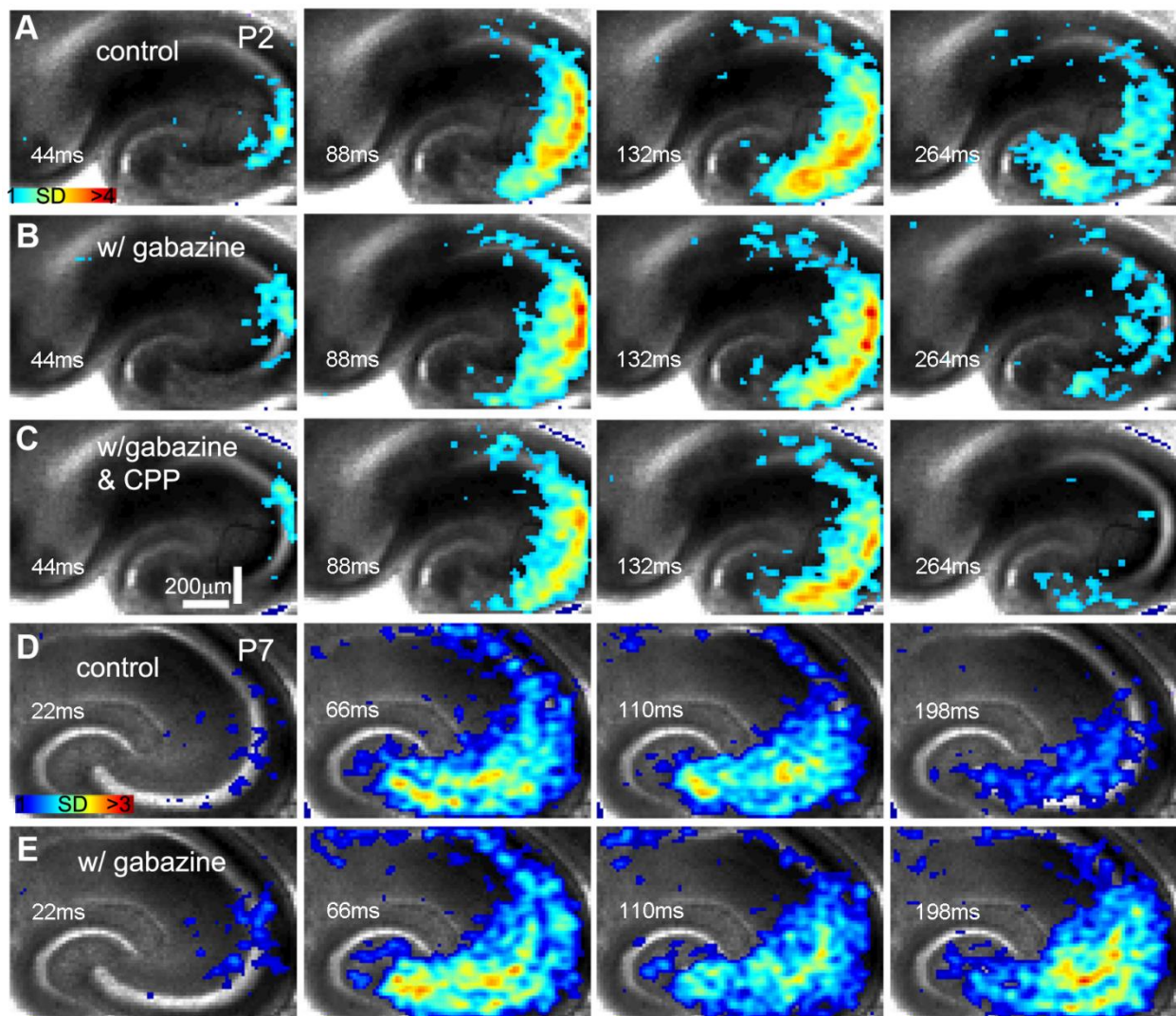
Figure. 1.3. The initiation and propagation of spontaneous GNA does not require GABA$_A$ receptor- or NMDA receptor-mediated signal transmission. A-C and **D-E**, time series data from the P2 and P7 slices, respectively. **A**, **B** and **C**. Spontaneous GNA in normal recording solution, in the presence of the GABA$_A$ receptor antagonist, gabazine (20µM) and in the presence of gabazine and the NMDA receptor antagonist, CPP (10µM), respectively. The color scale corresponds to VSD signal amplitude expressed as SD multiples above the mean baseline. **D-E**. Spontaneous GNA in normal recording solution and in the presence of gabazine (20µM), respectively.

`

In addition, GNA event duration decreases with the increasing age from P2 onward (Fig. 1.2B), with the average duration of P2-P7 and P9-P16 being 1083.7 ± 76.9 ms and 719.8 ± 49.1 ms (p<0.005), respectively. Each GNA occurrence appears to last longer than intracellularly recorded rat GDPs (400-800ms) (Ben-Ari *et al.*, 1989; Bolea *et al.*, 1999) and extracellularly detected spontaneous field potential fluctuations, SPWs (50-100ms) (Buhl and Buzsaki, 2005; Maier et al., 2003). Moreover, the GNA amplitude decreases with increasing postnatal age (Fig. 1.2C); the average peak amplitudes across slices were 1.17% ± 0.19%, measured with the percent change in pixel light intensity ($\Delta I/I$ %) and 0.56 ± 0.17% for P2-P7 and P9-P16 slices (p< 0.001), respectively (Fig. 1.2C). However, the velocity of activity propagation as measured by the travelling peak of VSD signal (Fig. 1.1E) increases with age, going from 8.8 ± 3.2 µm/ms during P2-P4, to 28.6 ± 10.6 µm/ms during P5-P7 and to 90.1 ± 25.6 (p< 0.01) µm/ms during P9-P16 (Fig. 1.2D). Overall, mouse GNA exhibits developmental changes, which is likely related to circuit maturation. As the adult-like pattern of unidirectional circuit propagation from DG to CA3 to CA1 appears around 2 weeks of age (see below), the later time points for GNA duration, peak amplitude and propagation speed may reflect fundamentally different underlying processes at earlier (P2) versus later (P15-16) time points.

Interestingly, mouse GNA in the first postnatal week is different from GDPs reported in the rat based on differences between their pharmacological properties. GNA is not suppressed by blocking GABAergic transmission via GABA$_A$ receptor antagonists (gabazine, SR95531 or bicuculline). While GNA frequency, amplitude or

propagation speed at P2-P5 does not change significantly in the presence of gabazine

(Fig. 1.3A-B), GNA at P7-P10 is enhanced by gabazine (Fig. 1.3D-E) (N = 5-6 slices

each). The changes of GNA properties in the presence of gabazine at P2-P5 versus

P7-P10 were quantified and summarized in Fig. 1.4. In contrast, mouse GNA is

completely abolished by the AMPA receptor antagonist (CNQX, 6-Cyano-7-

nitroquinoxaline-2, 3-dione) (N=10 slices). Furthermore, the NMDA receptor antagonist,

3-(2-carboxypiperazin-4-yl) propyl-1-phosphonic acid (CPP), with or without gabazine,

does not block the onset or propagation of this network activity (Fig. 1.3C). Thus, the

initiation and propagation of spontaneous GNA identified in the mouse hippocampus is

controlled by glutamatergic transmission mediated by AMPA receptors, rather than

$GABA_A$ or NMDA receptors.

Correlation between single cell events, field potential recordings and GNA

To address the cellular basis of mouse GNA, we first examined spontaneous

activity of excitatory pyramidal neurons in CA3 of P5-P6 mouse hippocampus. As

shown in Fig. 1.5A-B, our data indicate that spontaneously recurring, long-duration

membrane potential depolarization of single neuron may underlie GNA macroscopically

detected by VSD imaging. Most neurons recorded are spontaneously active, displaying

large and persistent depolarization of 20-50 mV superimposed with bursts of spikes that

are electrophysiologically similar to rat GDPs. The average frequency of these

persistent depolarization sampled from 6 excitatory neurons (P5-P6) was 1.48 ± 0.30

events/minutes, and their average duration was 1.29 ± 0.09 seconds. Gabazine does

not abolish persistent depolarization, but reduces their over-riding spiking activity, which

makes large membrane depolarization more prominent. All spontaneous spiking activity

`

and depolarization are blocked by CNQX. Overall, these properties of long-duration

cellular depolarization (electrophysiological equivalent of GDPs in mouse hippocampus,

mouse GDPs) are consistent with GNA properties.

Figure 1.4
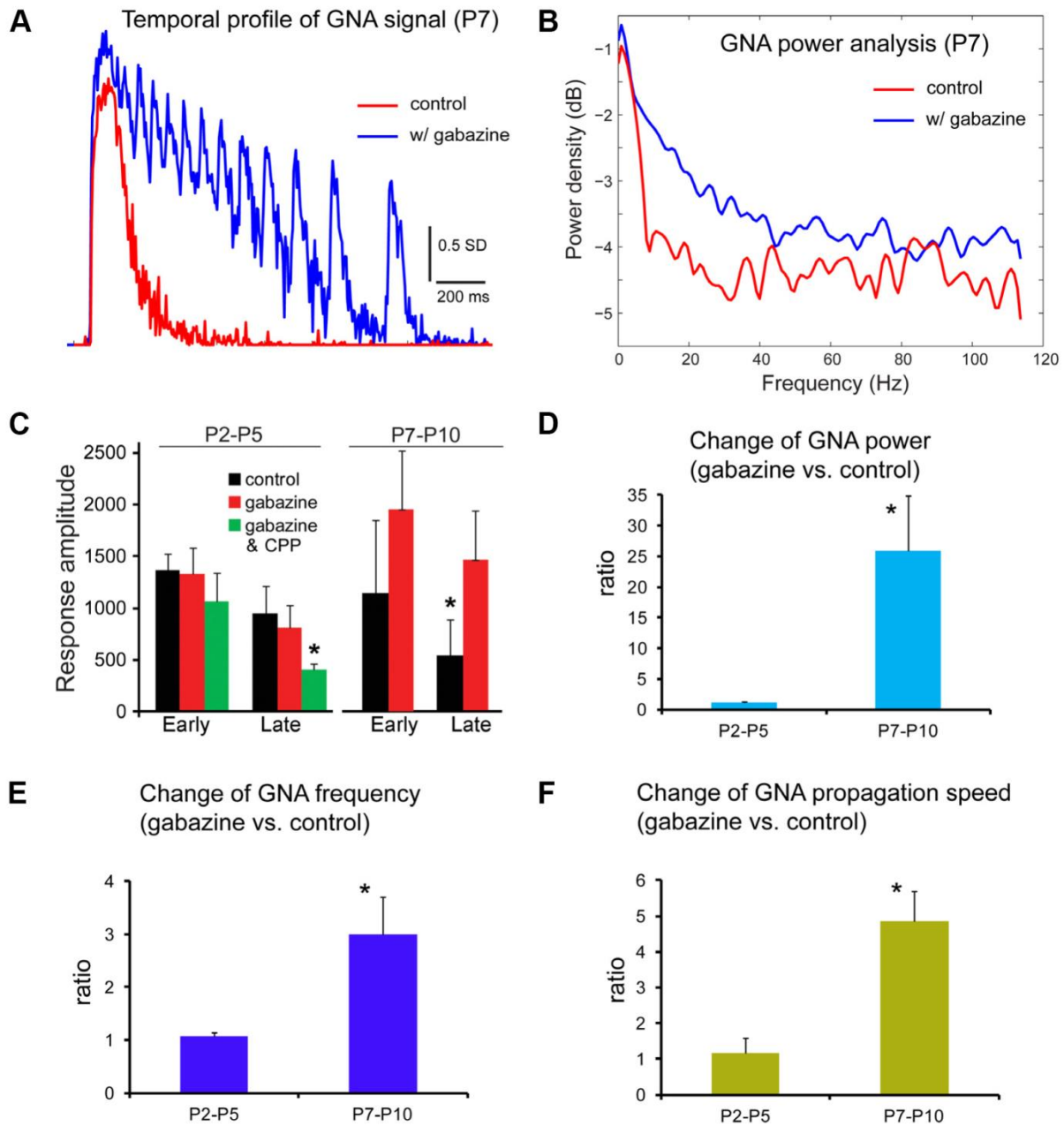
Figure.1.4. Characterization of changes of GNA properties in the presence of gabazine in comparison to the control condition.

`

A. Temporal profiles of GNA from the CA3 region of the P7 slice illustrated in Figure 3d and e for control and gabazine conditions, respectively. **B**. The power density function analysis of GNA for control and gabazine conditions of the P7 slice, which clearly shows increased power at higher oscillation frequencies. **C**. Average response amplitude (early and late response phases) of GNA across the entire hippocampus at P2-P5 and P7-P10 (N = 5-6 slices each) with different experimental conditions. The early and late response phases are defined as the time durations of 66-132 ms and 198-264 ms post-photostimulation, respectively. The response amplitude is in the unit of SD. * indicates a statistically significant difference ($p<0.05$) compared to control. The bar graphs represent mean ± SE. **D-F**. Changes of GNA power, frequency and propagation speed in the presence of gabazine. For the GNA power analysis, the VSD signal was acquired from averaging the pixels across the CA3 region from each image frame; the averaged values constituted the data points of the VSD signal trace in a temporal order. The signal trace was de-trended by linear regression to remove the baseline drift and then subtracted by its mean. The "pwelch" function in MATLAB was used to calculate the power values at different frequencies, which were summed to get the GNA power for the signal trace. In **D**, the power ratios of P2-P5 and P7-P10 GNA events (N= 9-12 each) are 1.17 ± 0.19 and 25.9 ±9.0, respectively. In **E**, the frequency ratios of P2-P5 and P7-P10 slices are 1.06 ± 0.07 and 3.0 ± 0.7, respectively. In **F**, the speed ratios of P2-P5 and P7-P10 events are 1.16 ± 0.42 and 4.86 ± 0.83, respectively. The y axis indicates the average ratio of the parameter measured in the presence of gabazine compared to the control condition. * indicates a statistically significant difference ($p<0.05$) compared to control.

As a developmental shift of GABA effects from mixed inhibition and excitation to exclusive inhibition between P6 and P10, we further tested the effects of blocking GABAA-receptor mediated activity at P10, the older age. To examine the effects of gabazine on single cell events at an older age, we recorded from CA3 pyramidal cells (N = 5 cells) in P10 mouse hippocampus. In control ACSF, the average frequency of mouse equivalent GDPs sampled from the P10 excitatory neurons was 0.33 ± 0.13 events/minutes, and their average duration was 0.67 ± 0.11 seconds. We found that gabazine led to enhanced circuit excitation with more frequent and large subthreshold EPSPs (Fig. 1.5C), which is consistent with GABA action at this older age. While typical mouse GDPs (indicated by single arrows in Fig. 1.5C) seen in control ACSF solution

`

continued to occur in the presence of gabazine, at P10 gabazine promoted excitation
resembling epileptiform activity (indicated by the double arrows in Fig. 5C).

Figure 1.5
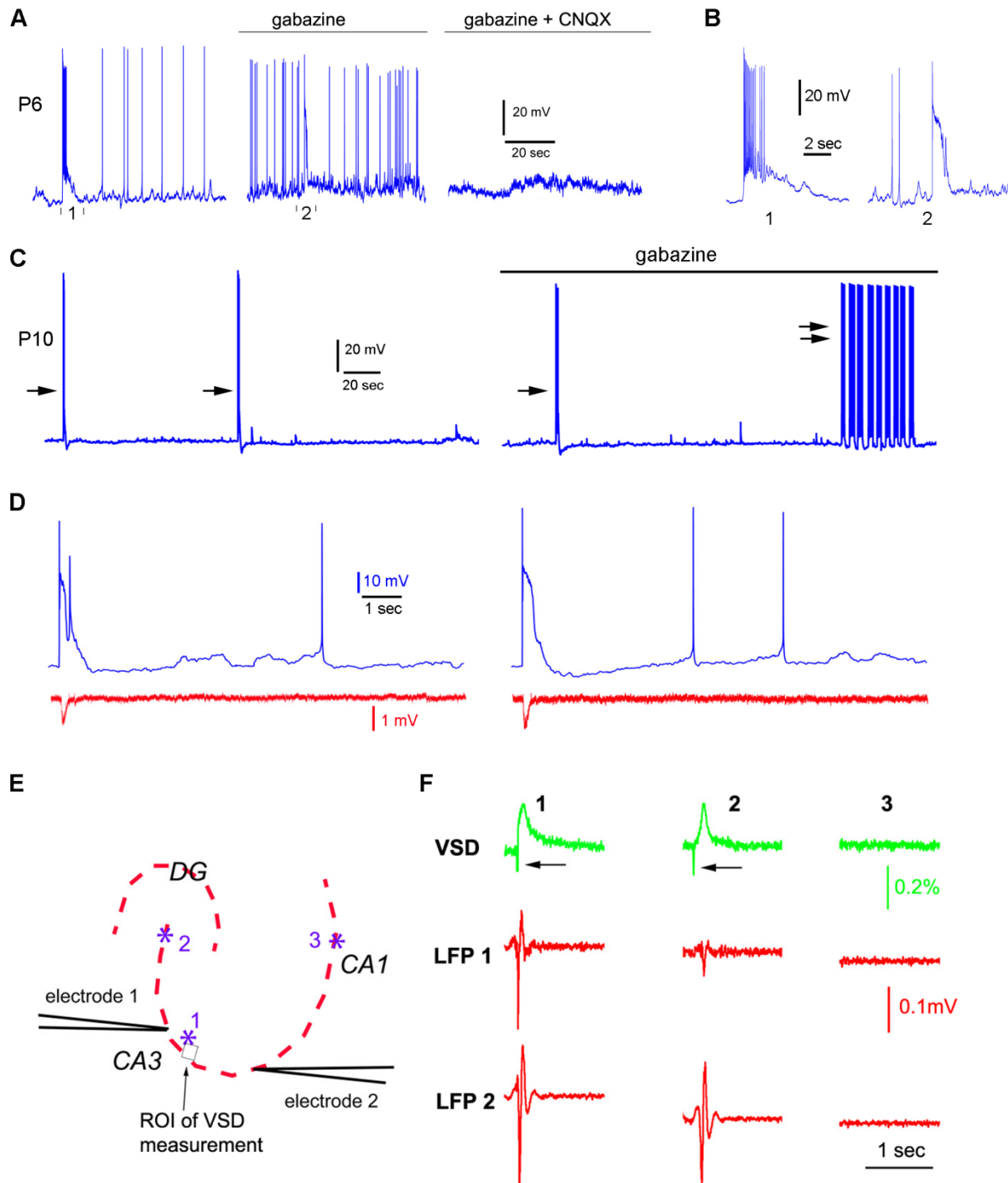
Figure.1.5. Correlation between single cell events, field potential recordings and GNA
A. Spontaneous activity of an example CA3 excitatory neuron (P6) in normal recording solution, in the presence of gabazine, and both gabazine and CNQX (left, middle, and right), respectively. **B**. The long-duration depolarization indicated by "1" and "2" in **A**, expanded and shown separately. C. Spontaneous activity of a CA3 excitatory neuron (P10) in normal recording solution and in the presence of gabazine (left and right), respectively. Single arrows point to typical long-duration depolarization, and the double arrows point to "epileptiform" activity. **D**. Examples of the occurrence of long-duration cellular depolarization (but not the spontaneous-recurring narrow spikes) coinciding with the occurrence of local field potential (LFP) events in P5-P6 slices. The membrane potential trace and the LFP signal trace are shown in blue and red, respectively. **E-F**. GNA occurrences detected by two-site field recordings in CA3 in P5-P6 slices. E shows the LFP electrode placement and photostimulation sites (1, 2, and 3) in the imaged slice. **F** shows simultaneous VSD and LFP detection in response to the sites (1-3) in **E**. The VSD signal was measured from the small region of interest (ROI) close to the site 1. The occurrences and propagation of GNA in response to photostimulation at the sites of 1 and 2 are reflected by the detection of LFP events from the two electrodes, while the local response in CA1 (site 3) did not induce GNA or lead to the LFP detection in CA3. The LFP signal traces were band-pass filtered at 5-300 Hz.

We also examined the relationship between mouse GDPs and local network events as detected by field recording with the electrode placed in the pyramidal cell layer at 100-200 μm away from the single cells examined (N=8 P5-P6 cells) (Fig. 1.5D). During the experiments, photostimulation using caged glutamate (see below) was delivered at a few sites around the recorded cells to induce the occurrence of mouse GDPs. We found that a great majority (86.6%) of the occurrences of long-duration cellular depolarization coincide with tight onset with the detection of local field potential (LFP) events (82 single cell events/71 field recording events), with the LFP duration being 51.8 % of that of long-duration cellular depolarization as would be expected due to extracellular averaging of intracellular events. This indicates that most mouse GDPs closely relate to LFP events reflecting neuronal ensemble behavior in local circuits.

In addition, we examined the correlation between GNA and LFP events by
comparing photostimulation evoked GNA and locally detected field events (Fig. 1.5E-F).
Every GNA occurrence is detected by two-site LFP recording separated at 200-300 μm
apart in CA3 (N = 61 events from 7 P5-P6 slices) and the stronger VSD signal
correlates to the stronger field potential response. The LFP response was faster than
VSD signal, as its peak of downward response (excitatory field response in the
pyramidal cell layer (Lamsa *et al.*, 2000)) occurs 25.7 ± 2.6 ms ahead of VSD signal
peak, due to different kinetics of the electrical versus the dye signal. Thus, at least in
these particular experiments, local field events are tightly correlated to GNA, which
indicate that LFP and GNA may measure the same underlying phenomena at different
scales.

Figure 1.6
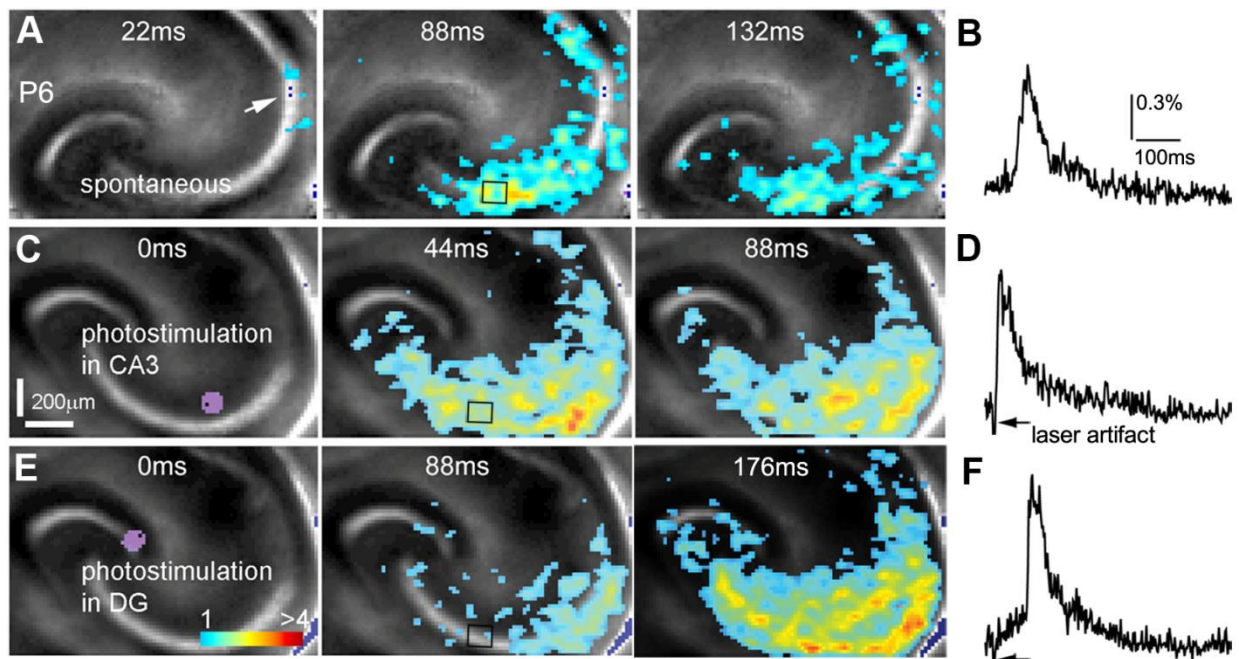
**Figure.1.6. Photostimulation-evoked GNA mimics spontaneous GNA in
spatiotemporal patterns. A.** Time series data of imaging spontaneous GNA at P6.
The arrowhead points to the initiation site in distal CA3. **B**. The time course of VSD

`

signal (in the percent change of pixel intensity [ΔI/I %]) from the region of interest indicated by the small rectangle in the second image frame in **A**. **C**. Time series data of imaging evoked GNA after spatially restricted laser photostimulation (via glutamate uncaging) in distal CA3. The site of photostimulation can be identified by the laser excitation artifact (purple) in the first frame. **D**. The time course of VSD signal from the region of interest indicated by the small rectangle in the second image frame in **C**. **E**. Time series data of imaging evoked network activity after spatially restricted laser photostimulation in DG. **F**. The time course of VSD signal from the region of interest indicated by the small rectangle in the second image frame in **E**. Note that **A**, **C** and **E** are images from the same slice, but **C** and **E** were acquired by the camera with an angle of rotation.

Photostimulation-evoked population activity in the developing mouse

hippocampal circuitry

To further examine the developing hippocampal circuit activity in the first

postnatal week, we used laser photostimulation via glutamate or GABA uncaging to

evoke population neuronal activity in defined sites of spontaneous GNA origin. Caged

compounds that are rendered biologically inert by the chemical addition of a light-

sensitive "caging" group were infused into the slices. Upon illumination of UV laser,

biologically active glutamate or GABA is liberated from the cage group and binds to its

cellular receptors. The laser beam forms uncaging spots, each approximating a

Gaussian profile with a width of ~100 μm laterally at the 4x objective focal plane (Fig.

1.6, also see (Xu *et al.*, 2010)).

Spatially restricted glutamate uncaging in mouse distal CA3 was found to evoke

population neuronal activity with similar features to spontaneous GNA (Fig. 1.6A-B),

with excitatory activity beginning at the site of photostimulation and propagating bi-

directionally, toward proximal CA3 and DG as well as toward CA1. The evoked activity

has an average latency of 15.5 ± 3.9 ms and an average duration of 746.3 ± 60.9 ms,

with an average peak amplitude of $1.68 \pm 0.22\%$ (N=13 slices). Similar to spontaneous

`

GNA, the propagation speed of evoked activity increases later in development, increasing significantly (p<0.005) from 6.5 ± 0.7 μm/ms in P2-P4 to 22 ± 5.5 μm/ms in P5-P7. Additionally, during P2-P5, gabazine does not appear to significantly affect evoked network activity (Fig. 1.7 A, B), but enhances excitatory activity evoked by glutamate uncaging in the second postnatal week (N=7 slices), matching the behavior of spontaneous GNA. In addition to distal CA3, we photostimulated other parts of the hippocampal circuitry. In the first postnatal week, evoked activity in DG propagates to CA3 and then spreads from CA3 to CA1 along the trisynaptic circuitry in the early phase, but there is clear back-propagation from CA3 to DG in the late response phase (Fig.1.6C), which mimics the activity induced by distal CA3 photostimulation and spontaneous GNA. However, photostimulation in CA1 does not lead to backward propagation to CA3. Therefore, backward or reverse propagation in the developing circuitry indicates a strong excitatory pathway from CA3 to the hilus and the fascia dentate of DG, which does not appear in mature circuitry (Scharfman, 1994; 2007).

We also examined the circuit response to GABA uncaging (N=14 slices). Localized excitatory responses are observed at the uncaging sites in mouse slices from P1-P5, whereas excitatory activity is no longer clear at P6-P7. In the younger slices, sometimes GABA uncaging in CA3 induces propagating network activity (N=5 slices) similar to glutamate uncaging (Fig. 1.7C), although GABA uncaging has a longer response latency (85 ± 13 ms). Importantly, GABA-evoked propagating activity is blocked by the AMPA receptor antagonist, CNQX, leaving only a localized response at the GABA uncaging site (Fig. 1.7D). This indicates that GABA can excite neonatal neurons and contribute to the initiation of spontaneous activity, but the propagation of

28

`

excitatory activity in the developing mouse hippocampal circuitry is determined by

AMPA receptor-mediated transmission.

Figure 1.7
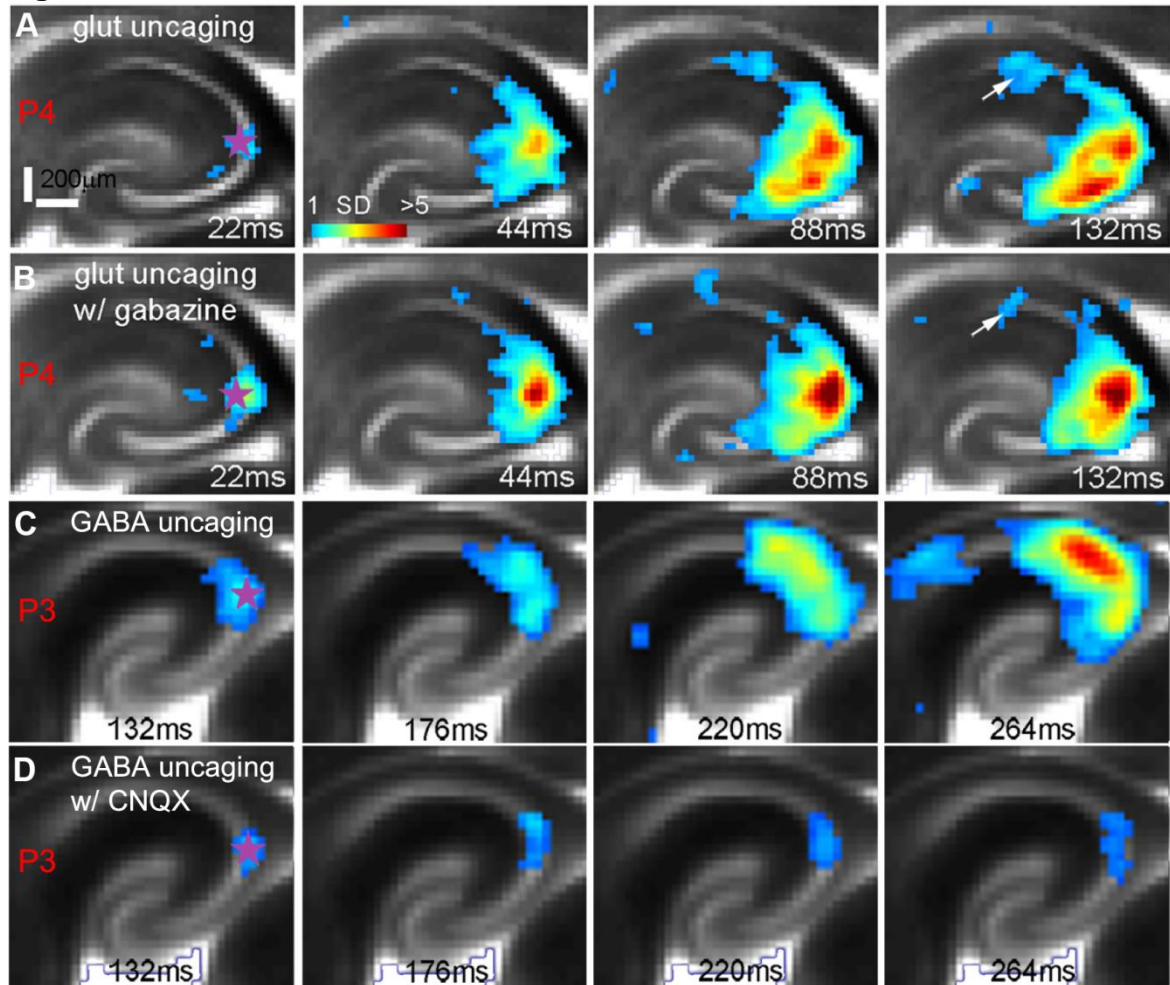
Figure. 1.7. Mouse GNA is dominated by AMPA receptor-mediated glutamatergic transmission. A and **B**. Photostimulation-evoked network activity by glutamate uncaging in a P4 slice was largely unaffected by the GABA$_A$ receptor antagonist, gabazine (20 μM). The uncaging site is denoted by a purple star. The arrows indicate some reduced propagation to CA1 in the presence of gabazine. **C** and **D**. The propagation of photostimulation-evoked network activity by GABA uncaging in a P3 slice was abolished by the AMPA receptor antagonist, CNQX (10 μM). The excitatory response at the uncaging site in **D** was blocked by the further application of gabazine with CNQX. Note that photostimulation and imaging of both slices were performed through a 2x objective.

Global network activity and circuit connections

`

To establish the temporal relationship between GNA and the maturation of functional circuit connections, we mapped the development of hippocampal neural circuitry over the time course during which GNA is active. First, synaptic connections to excitatory pyramidal neurons were mapped by combining whole cell recordings with laser scanning photostimulation (LSPS) (Ikrar et al., 2011; Shi et al., 2010). As illustrated in Fig. 1.8A-C, the LSPS approach involves first recording from a single neuron, then stimulating at other sites in order to generate action potentials from neurons in those sites; recording from the potential postsynaptic neuron allows one to determine if there is actual synaptic input from one particular site. By sequentially stimulating many different sites across the hippocampus, it is possible to generate a map of locations of neurons providing input to that one cell. Through the LSPS mapping experiments, we found that there is clearly observable strengthening of excitatory and inhibitory connections to CA3 pyramidal neurons over the developmental time course (Fig. 1.8D-F, Fig.1.9. A-D). Younger neurons (e.g., P2-P4) have weaker synaptic connections with more localized input from around the perisomatic region, while older neurons (e.g., P9-P12) have stronger and more extensive synaptic connections from a wider area (Fig. 1.8D-F). DG connections to CA3 neurons are increasingly strengthened at older ages as illustrated in the example maps. The average, summed excitatory synaptic input strength measured from excitatory pyramidal cells are 80.8 ± 10 pA (N=10 cells), 650.4 ± 99.9 pA (12 cells) and 1362.7 ± 292.9 pA (8 cells) for the three age groups (P2-P4, P5-P7, P9-P12), respectively (Fig. 1.9A). The extent of local excitatory connections also increases significantly from P2-P4 to P5-P12 by measuring the numbers of input-mapped locations (Fig. 1.9B). Along

with the enhanced input strength, synaptic responses at P5-P7 and P9-P12 have overall

shorter latencies than P2-P4 (median latencies: 67.6 ± 7.6 ms, 40.6 ± 2.9 ms, and 42.7

± 3.5 ms for P2-P4, P5-P7 and P9-P12, respectively) (Fig. 1.9C). In addition, inhibitory

synaptic connections to pyramidal cells start to be detected by measuring inhibitory

postsynaptic currents (IPSCs) to the recorded neurons at the end of the first postnatal

week, and are clearly enhanced during the second week. The average, summed

inhibitory synaptic input strength measured from excitatory pyramidal cells are 104 ±

41.5 pA (N=6 cells), 904.1 ± 215 pA (11 cells) for the age groups of P6-P7 and P12-P16,

respectively.

We also correlated functional circuit connectivity with cell morphological

development by examining the overall dendritic morphology of CA3 excitatory pyramidal

cells that are revealed by intracellular biocytin labeling in early developing hippocampus.

There is a rapid dendritic expansion of CA3 pyramidal cells during the first two postnatal

week (Fig. 1.10).   Consistent with their wider input connections revealed by

photostimulation mapping, compared to P1-P4 (Fig. 1.10A, B), CA3 excitatory pyramidal

cells have much wider dendritic fields and more extensive branches at or beyond P7

(Fig. 1.10 C, D). The average apical dendritic lengths for selected P1-P4 cells and P7-

P8 cells were 79.1 ±12.2 µm, and 521 ± 15 µm, respectively (p < 0.01; N = 5 cells each).

To examine the underlying pathways accounting for GNA back-propagation from

CA3 to DG, we further examined the circuit connections to excitatory mossy cells in the

hilus and DG granule cells.   In the mouse developing hippocampal slices (P4-P6), we

found that mossy cells receive strong excitatory input from proximal CA3 (average

strength: 228.9 ± 58.9 pA measured from N = 8 cells) (Fig. 1.11A). Although DG

`

granule cells have much weaker local input compared to hilar mossy cells, they receive

excitatory input from the hilus and proximal CA3 (average strength: 14.6 ± 3.8 pA and

12.1 ± 3.5 pA, respectively, measured from N = 7 cells) (Fig. 1.11B). Therefore, GNA

back-propagation from CA3 to DG is likely mediated through the di-synaptic circuit of

proximal CA3 pyramidal cells ->hilar mossy cells-> DG granule cells or the mono-

synaptic circuit of proximal CA3 pyramidal cells -> DG granule cells.

Figure 1.8
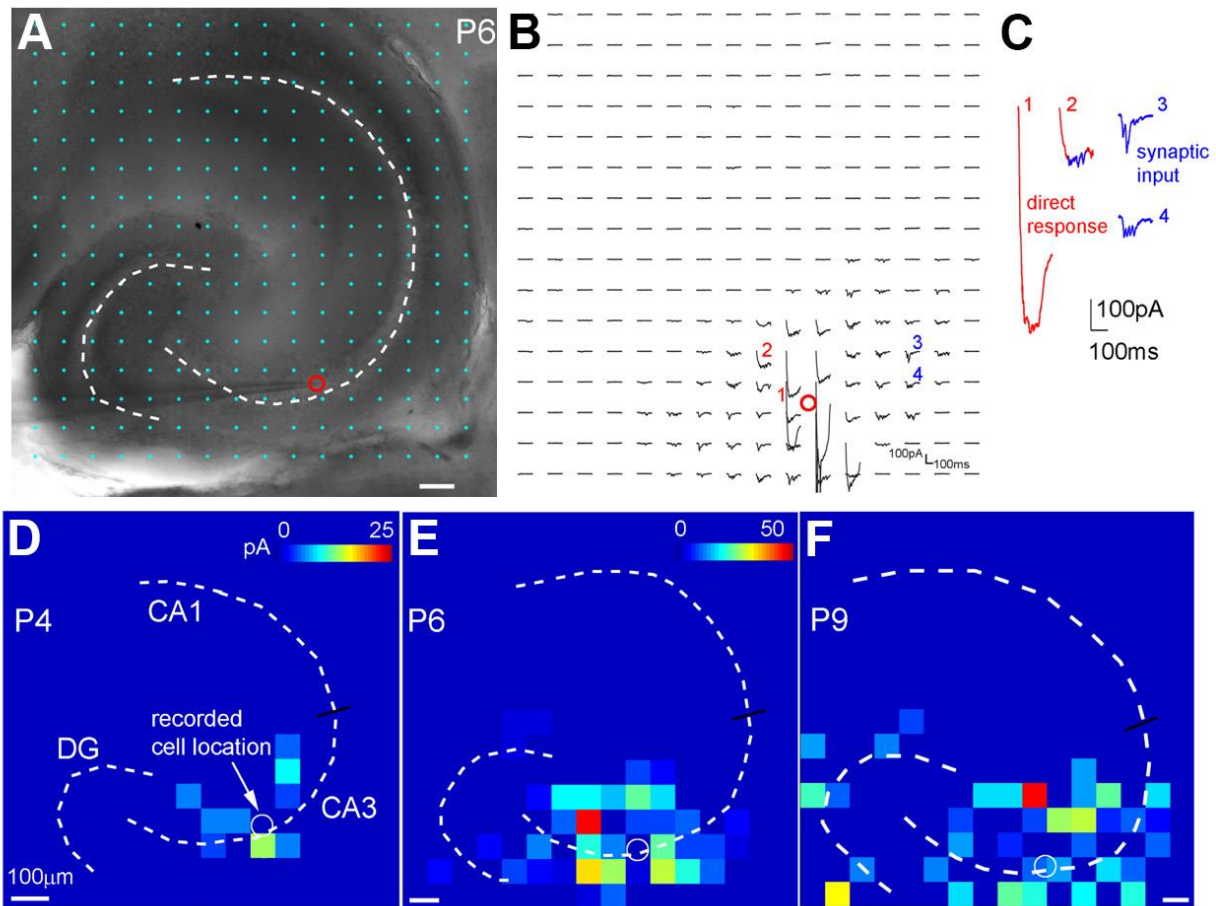
**Figure. 1.8. Developmental strengthening of local synaptic connections to CA3
excitatory pyramidal neurons. A-C**. Laser scanning photostimulation combined with
whole cell recordings to map local synaptic connections to single neurons. **A**. Mouse
hippocampal P6 slice image with the superimposed photostimulation sites (16 x 16 cyan
*, spaced at 80 µm x 80 µm). **B**. Photostimulation-evoked response traces from the
corresponding sites in **A**, with the recorded cell held in voltage clamp mode to detect
inward excitatory postsynaptic currents (EPSCs). The red circle indicates the recorded

`

cell body location. Different forms of photostimulation responses are illustrated by the traces which are expanded and separately shown in **C**. Trace 1 is an example of a large direct response (excluded for further analysis) to glutamate uncaging on the cell body. Trace 2 shows an example of relatively small direct response, with over-riding synaptic responses (blue). Traces 3 and 4 are typical examples of synaptic input responses. **D-F**. Color-coded synaptic input maps showing local excitatory connections to representative CA3 cells at P4, P6 and P9. The input maps are constructed based upon quantification of photostimulation-evoked excitatory synaptic input at stimulation sites across the hippocampus (see the Methods). The color scale codes average input strength at each stimulation site. The amplitude scale in **E** applies to **E** and **F**.

In conjunction with the circuit mapping of single cells, photostimulation and VSD imaging was used to measure evoked circuit excitability and the directionality of excitatory signal propagation over P2-P15. By examining photostimulation-evoked VSD response at two different uncaging initiation sites (DG versus distal CA3) across developmental times, it is obvious that younger slices are more excitable than older slices at both sites with more extensive and stronger response propagation (Fig. 1.12 A-D). The VSD response strength at glutamate uncaging sites is 1.46% ± 0.09% (P2-P7, N = 10 slices) and 0.48% ± 0.04% (P9-P15, N = 12 slices) for younger and older slices, respectively. Backward propagation from distal CA3 to DG in the first postnatal week is robust (Fig. 1.12B). However, while DG signaling to CA3 is maintained, the back-propagation to DG from distal CA3 is significantly decreased toward the end of the second postnatal week (Fig. 1.12D). This is supported by the finding that DG activation at P11-P14 was much less than P7-P10 in response to distal CA3 photostimulation. Therefore, the emergence of the canonical unidirectional trisynaptic circuit organization in the developing hippocampus concurs with the disappearance of spontaneous GNA at around P14-P16.

Figure 1.9
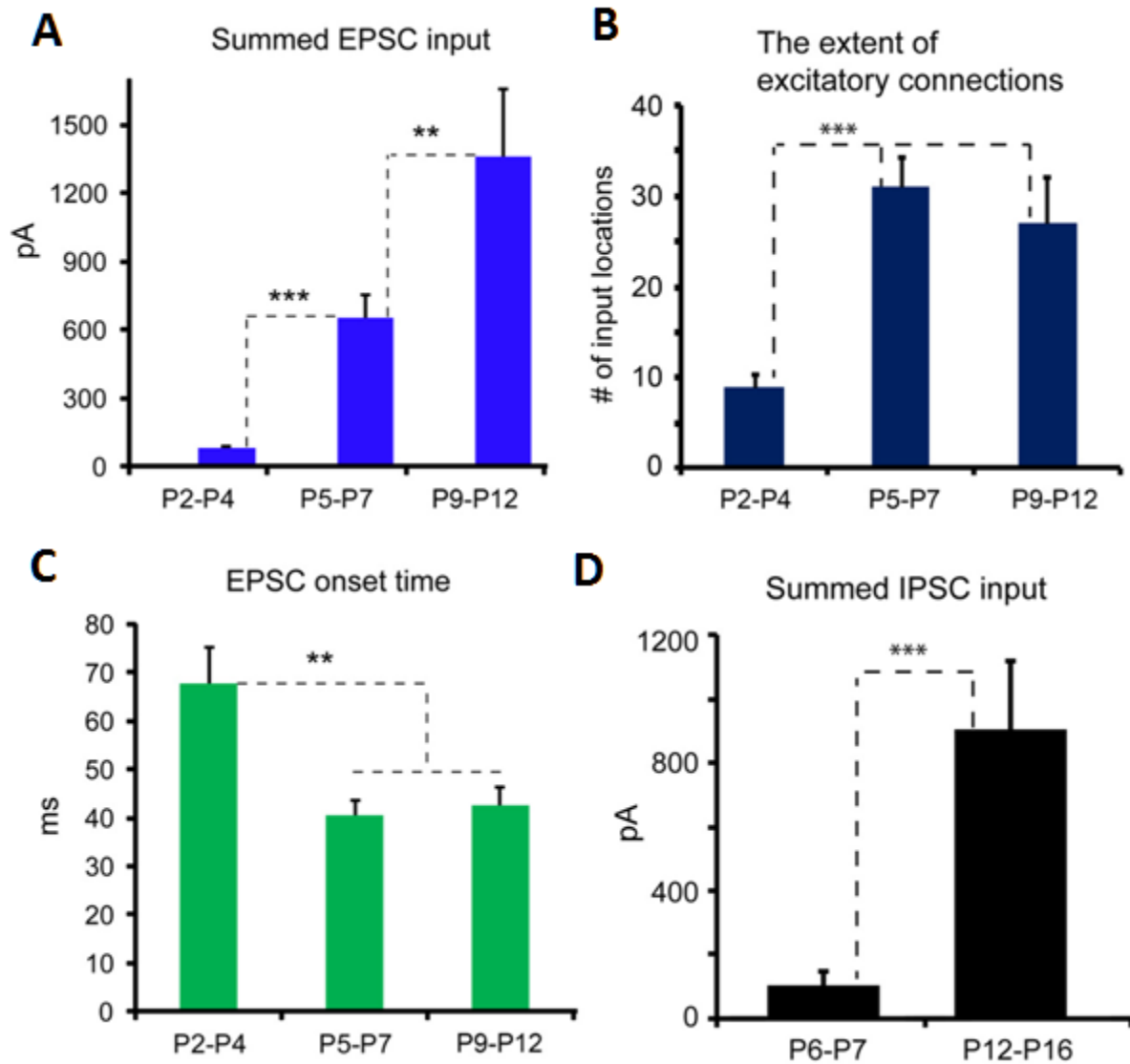
Figure 1.9. Quantitative comparison of synaptic input strength, the extent of excitatory connections and the response latencies of CA3 excitatory neurons of P2-P4 (N=10 cells), P5-P7 (N=12 cells), and P9-P12 (N=8 cells). Specifically, **A**, **B** and **C** show the measurements of the average summed EPSC input strength to single CA3 cells, the average number of input locations and the average onset times of the first detected EPSC per site, respectively. **D**. Quantitative comparison of inhibitory synaptic input strength to CA3 excitatory neurons for the age groups of P6-P7 and P12-P16 (N = 6 and 11 cells, respectively). ** and *** indicates statistical significance of $p<0.01$ and <0.001 between the groups.

Discussion

`

Spontaneous network activity early in development is considered an important factor for sculpting and refining developing circuit architecture. Our approach to studying the developmental contributions of spontaneous and correlated neuronal activity in hippocampus is to determine which events are closely linked to establishing adult functional circuit organization. In this work, we identified and characterized a global pattern of activity we term spontaneous GNA, and a major transition of functional circuit organization in the developing mouse hippocampus from large scale bi-directional signal propagation to the adult-like form of the canonical unidirectional trisynaptic circuit.

Terminology and technical considerations

We coined spontaneous GNA as a new term to describe spontaneous network events in developing mouse hippocampus, based on large-scale VSD imaging of global circuit events. In the same way SPWs and GDPs were coined to specifically refer to the events at single cell and localized circuit levels, we use GNAs to describe large-scale spontaneous network events in developing mouse hippocampus measured by macroscopic VSD imaging. While there are some similarities of spontaneous GNA with the previously examined localized activity patterns, there are differences that indicate that spontaneous GNA does not correspond directly to such local events as GDPs or SPWs recorded with other techniques in the rat (Ben-Ari et al., 1989; Ben-Ari et al., 2007; Buhl and Buzsaki, 2005; Buzsaki, 1986; Leinekugel et al., 2002). While rat GDPs depend on GABAergic transmission (Ben-Ari et al., 2007), mouse GNA is not abolished by GABAa receptor antagonists,. We also observe an obligatory contribution of glutamatergic signaling through AMPA receptors required for mouse GNA. Single cell

35

`

GDP-like events are likely components of the summed macroscopic circuit events we measure as mouse GNA, but they can be distinguished by differing pharmacological sensitivities between the species. In addition, aside from scale, GNA captures emergent properties not described for GDPs, notably the bi-directionality of signal propagation from distal CA3 origin to both CA1 and dentate gyrus. In the previous study using fast VSD imaging, Bolea et al. (2006) referred to GDP-related network events as neuronal coactivation in the developing rat hippocampus, in which a propagating excitation wave could initiate from a small site and propagate to larger hippocampal circuitry. In contrast to what we observed form mouse GNA, they reported that GDP-related waves can originate both in the hilus and in CA3 and that the initiation site is not fixed and varies from event to event.

While the question whether GNA, GDPs and SPWs are different facets of the spontaneous activity patterns in hippocampus remains to be further addressed, we have significantly built on earlier findings on spontaneous network activity in the developing hippocampus by using a suite of new technologies. Fast VSD imaging allows for a macroscopic network-level view of the spatial and temporal dynamics of neural activity across the entire hippocampal circuitry. VSD signal is closely correlated with subthreshold membrane potential depolarization (rather than action potentials), so that VSD imaging is better suited to examine long-duration membrane potential depolarization and can better reveal early neuronal activity ($\leq$ P4) without fully-developed action potentials compared to Ca^{2+} imaging. We corroborated our findings on spontaneous GNA in a parallel set of studies using evoked population activity by laser scanning photostimulation (LSPS) via glutamate or GABA uncaging in the

`

developing circuitry. The LSPS approach with whole cell recordings has further

provided definitive data to reveal changes in local circuit connections over the GNA

active time course.

Figure 1.10
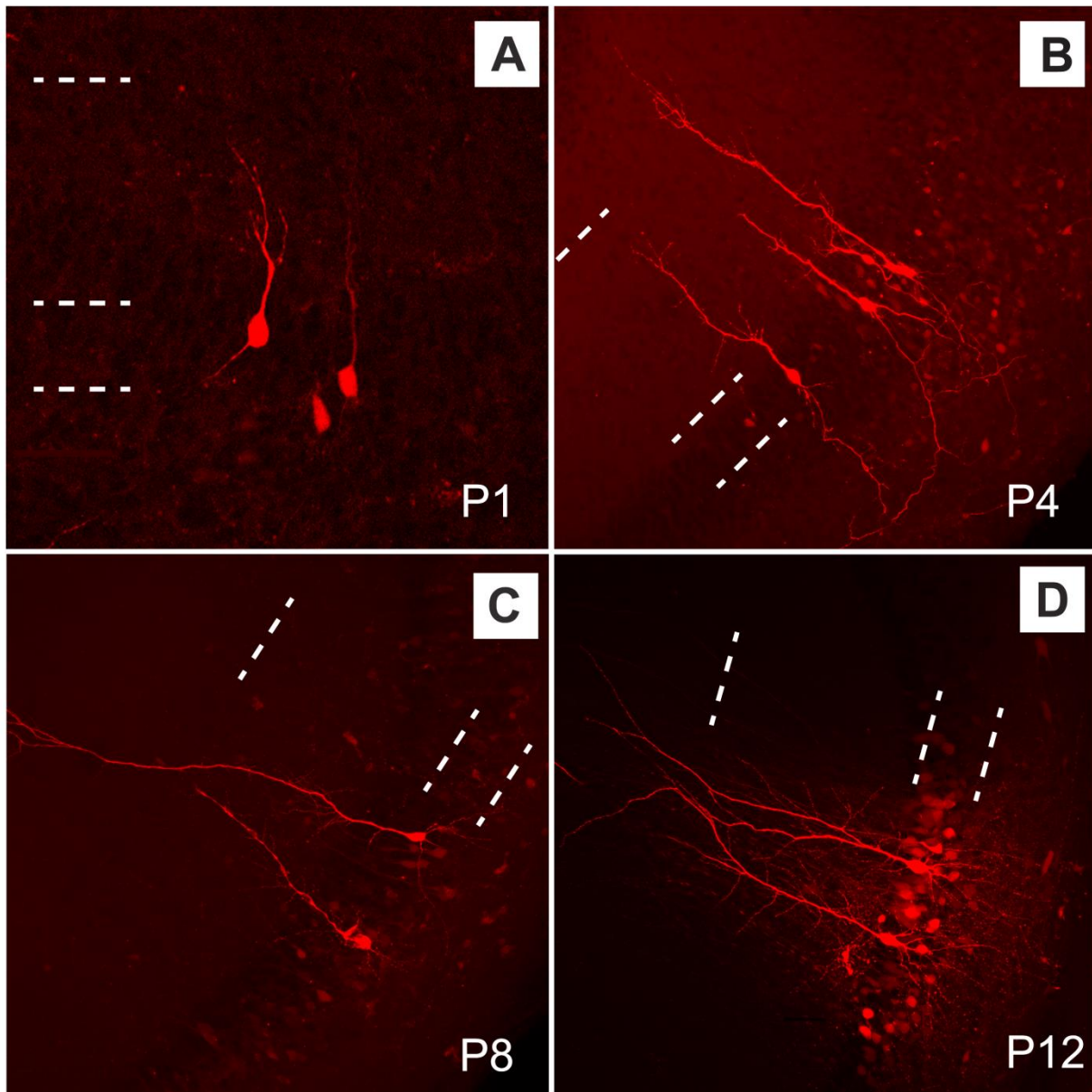
Figure. 1.10. Morphology of CA3 excitatory pyramidal cells in the developing mouse hippocampus. A-D. Gross morphology of example pyramidal cells of P1, P4, P8 and P12, revealed by intracellular biocytin labeling. Compared to older ages, P1-P4 cells have much shorter apical dendrites. The scales in A and B are 50 µm. The scale

`

in B applies to both C and D. SP: stratum pyramidale; SR: stratum lucidum and radiatum; SLM: stratum lacunosum moleculare.

Spontaneous hippocampal network activity

Compared to unidirectional nature of signal propagation exhibited by adult hippocampus, the immature hippocampal circuitry shows substantial bi-directional signal propagation, which we term GNA. Mouse GNA shares some features with GDP related activity propagation and SPWs with multisite extracellular recordings (Csicsvari et al., 2000; Leinekugel et al., 1998; Maier et al., 2003). The distal CA3 origin of GNA and SPWs may be significant, as this region is adjacent to CA2 and receives strong input from the supramammillary nucleus that has been implicated in controlling the frequency of the theta rhythm and the spread of epileptic activity in the hippocampus (Chevaleyre and Siegelbaum, 2010; Lein et al., 2005; Ochiishi et al., 1999). Given the intrinsically bursting properties and high excitability of CA3 excitatory neurons (as we have observed), it is likely that the initiation of mouse GNA is through the intrinsic pacemaker properties of CA3 excitatory neurons and the interactions between excitatory neurons, as proposed for the hippocampus and neocortex (Sanchez-Vives et al., 2000; Sipila et al., 2005).

We have used single cell and field potential recordings to address the relationship between single cell behavior, local circuit events and GNA. Although there is a strong correlation between the electrophysiological equivalent of GDPs in the mouse hippocampus and local field events, our results indicate that spontaneous occurrences of single cell events like GDPs do not have a one-to-one correspondence to large-scale propagating events. This finding is consistent with the previous

observation that rat GDPs can occur in the absence of local network events detected by field recordings (Sipila et al., 2005).

Figure 1.11
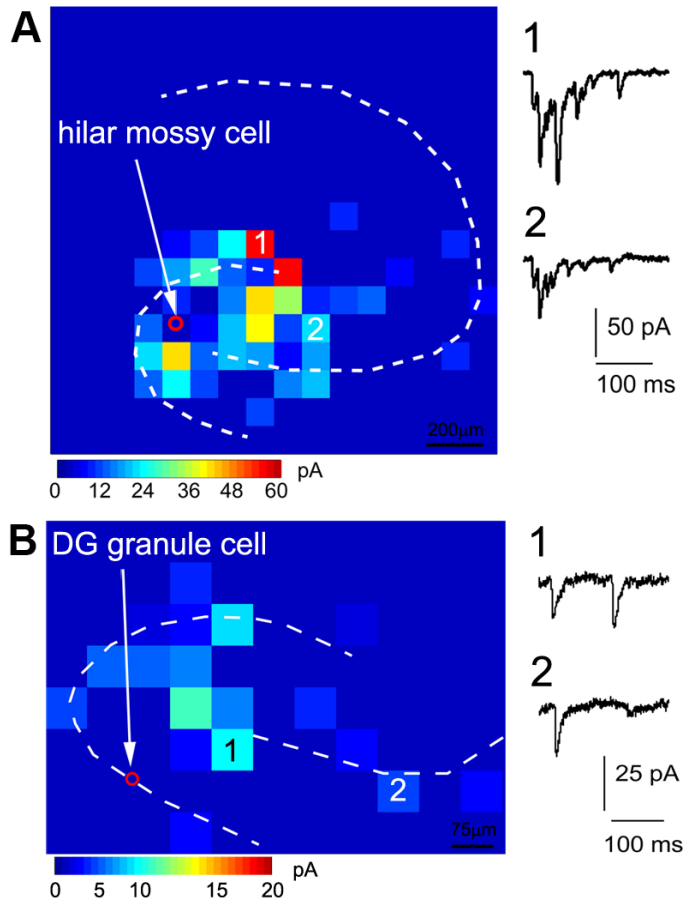
Figure. 1.11. Local excitatory synaptic connections to hilar mossy cells and DG granule cells reflect the underlying pathways of the GNA back-propagation from CA3 to DG.
A-B. Example excitatory input maps to one hilar mossy cell and a DG granule cell (P4-P6), respectively. As shown in **A**, mossy cells, the only excitatory cells in the dentate hilus, receive robust excitatory input from proximal CA3 area in addition to DG and the hilus. As illustrated in **B**, the granule cells receive relatively strong excitatory input from the hilus and weaker input from DG and proximal CA3.

Mouse GNA and rat GDPs have a similar developmental time course; the disappearance of GNA immediately transitions to the emergence of the adult-like unidirectional circuit organization at around two weeks of age in the mouse. In contrast

to the typical notion of GABA-mediated rat GDPs, mouse GNA and the electrophysiological equivalent of GDPs in mouse hippocampus are largely GABA independent and mediated instead by glutamatergic transmission via AMPA receptors postnatally. There is an interesting suggestion that glutamatergic signaling developmentally interacts with GABAergic signaling in rat GDPs (Ben-Ari *et al.*, 1997; Lamsa *et al.*, 2000). In fact, it has been reported that in neonatal rat hippocampal slices, glutamate controls the induction of GABA-mediated GDPs through AMPA receptors, and superfusion of CNQX completely blocks GDPs (Bolea *et al.*, 1999). Furthermore, evoked GDPs in immature rat slices (P2-12) are blocked in the presence of bicuculline, but GDPs evoked by suprathreshold stimuli are mostly resistant to bicuculline and inhibited with CNQX (Xie et al., 1994). Therefore, there are glutamatergic contributions to both mouse GNA and rat GDPs, which show differential features that may be related to species differences.

GNA and circuit maturation

In terms of functional significance, GNA may play an important role in patterning and strengthening intra-hippocampal synaptic connections during early development, resembling other forms of spontaneous neural activity. While adult form of SPWs induced in slice preparations are reported to modulate synaptic connectivity and strength between neurons and regions (Behrens *et al.*, 2005), correlated bursts of activity in the neonatal hippocampus *in vivo* (i.e., early form of SPWs) can provide correlated activity for immature neurons and may underlie activity-dependent maturation of the hippocampal network (Leinekugel *et al.*, 2002). The best demonstration of the causal relationship between spontaneous network activity and synaptic input strength of

specific neurons was shown experimentally by reducing spontaneous network activity *in ovo* in the intact chick embryo (Gonzalez-Islas and Wenner, 2006). The forward and backward propagation of GNA could contribute to the establishment of neuronal population connections between hippocampal subfields, e.g., between CA3 and DG as well as between CA3 and CA1, through recurring local synchronous activity. We show the time course of developmentally enhanced synaptic connections between DG and CA3 neurons by photostimulation mapping of circuit connections to single CA3 neurons.

Figure 1.12
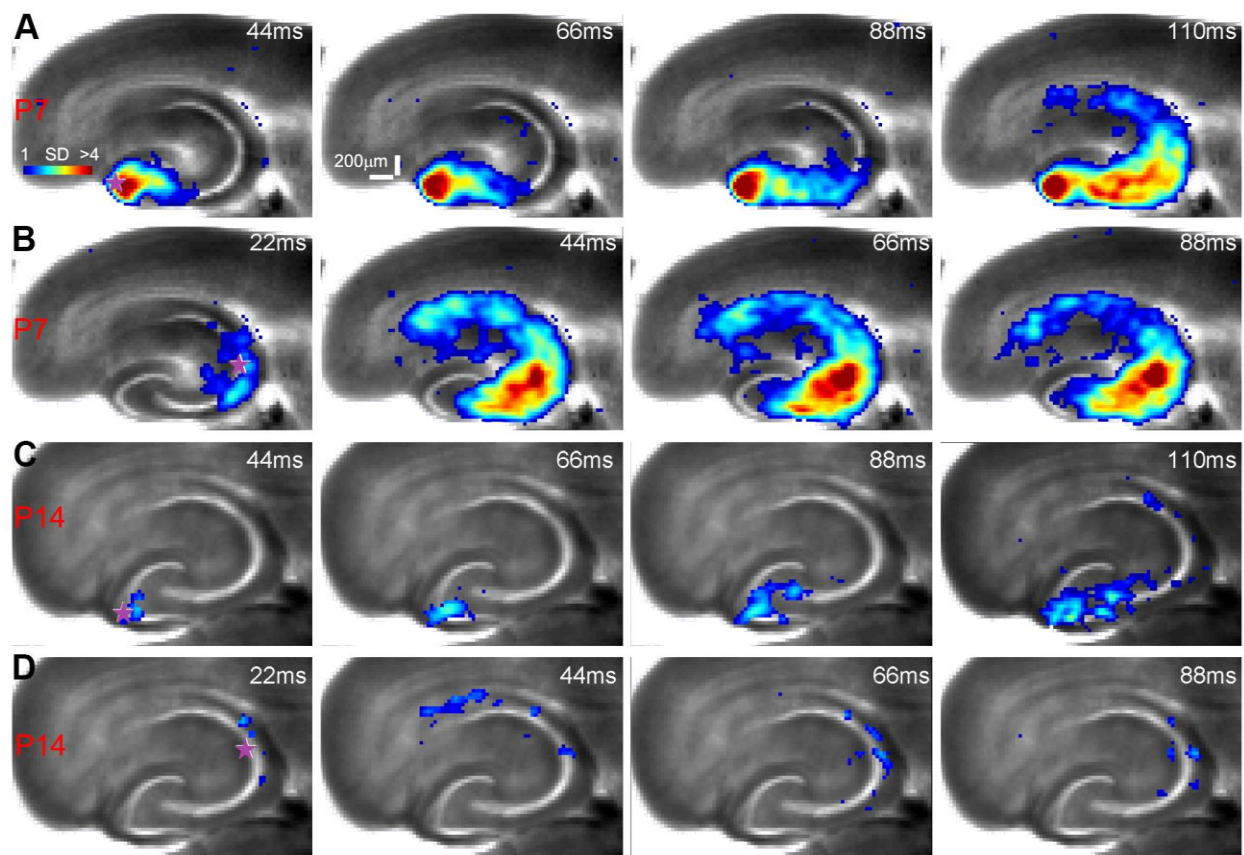
Figure. 1.12. The emergence of the unidirectional circuit organization in the developing hippocampus occurs around the end of the postnatal two weeks. A-B. Time series data of imaging photostimulation-evoked network activity by glutamate uncaging in DG and distal CA3 in a P7 slice, respectively. The uncaging site is denoted by a purple star. **C-D**. Time series data of imaging photostimulation-evoked network activity by glutamate uncaging in DG and distal CA3 in a P14 slice, respectively. Note

`

that photostimulation and imaging of both slices were performed through a 2x objective, and that 3 trials of imaging data were averaged for the presentation. Given the lower sensitivity of the 2x objective, the weaker activated granule cell layer of DG does not show as well as hilar activation in the presented frames, but it is detected with our signal analysis.

Our data show that the weakening and disappearance of bi-directional GNA concurs with the maturity of the trisynaptic circuitry in which the CA3 back- propagation is reduced through decreased circuit excitability and enhanced inhibitory neuronal control that ensures unidirectional information flow. The most important contributing factors include the maturing of the $GABA_A$ receptors and changing of circuit connectivity. We speculate that failure of controlling the back- propagation of distal CA3 beyond early developmental stages may contribute to pathological conditions related to learning and memory deficits and temporal lobe epileptogenesis (Myers and Scharfman, 2011; Scharfman, 2007).

In conclusion, spontaneous GNA immediately precedes the more restricted unidirectional propagation of excitation through the hippocampus that persists into adulthood. Further studies that manipulate the spatial and temporal properties of GNA should reveal its functional importance for setting up the adult circuit architecture.

Chapter 2:
Local circuit connections to hilar mossy cells in the mouse hippocampus

Hilar mossy cells are the only excitatory cells in the dentate hilus, and they have been studied extensively due to its potential critical roles in cognitive functions such as pattern separation and in temporal lobe epileptogenesis. Little is known, however, about the development of local circuit connections of mossy cells. To better understand functional circuit operations of this unique cell type, here we combine whole cell recordings and laser scanning photostimulation (LSPS) to examine both local excitatory and inhibitory synaptic inputs to mossy cells in living slice preparations of mouse hippocampus at different postnatal ages (P7, P14 and P24). The LSPS method allows for much wider input sources to be mapped to intracelluarly recorded neurons than paired or multiple intracellular recordings of synaptically connected neurons, and provides a quantitative assessment of spatial distribution and input strength of excitatory and inhibitory connectivity to the recoded neurons.   Hilar mossy cells are targeted by visualizing non-red fluorescent expression in the dentate hilus of the double transgenic Gad2-Cre:tdTomate mouse, and confirmed by post hoc morphological characterization. We identified developmental changes of local circuit connections to mossy cells in living slice preparations of mouse hippocampus at different ages (P6-7, P13-14 and P21-28).

Our results indicated that at P6-7, mossy cells received extensive excitatory inputs from proximal CA3 pyramidal cells, with total summed excitatory inputs greater than those from dentate granule cells and from within the hilus. In comparison, at P14 and P24, the largest excitatory inputs to mossy cells were from dentate granule cells while the inputs of proximal CA3 and the hilar region were greatly reduced or

`

diminished. In addition, the inhibitory connections to mossy cells appeared to be

balanced with the excitatory connections at different ages, with inhibitory input sources

generally matching excitatory input sources. Overall, local inhibition to mossy cell

increased with the developmental ages. Together, these data provide important new

information on local synaptic circuits of mossy cells, and supports the proposed

pathway of excitatory back projection from CA3 to dentate granule cells via hilar mossy

cells, particularly in the developing hippocampal circuitry.

`

Introduction

Hilar mossy cells are the major glutamatergic neurons in dentate hilus (Soriano and Frotscher, 1994; Scharfman, 1995). Past anatomical study reveals that mossy cell has relatively large soma with thick proximal dendrites, covered by numerous large spines called thorny excrescences (Amaral, 1978) . The whole neuron seems like covered with moss; hence it comes the name. These thorny excrescences are considered the location of mossy fiber synapses (Laatsch and Cowan, 1966).

Mossy cells are mostly involved in two circuits in hippocampus. Mossy cells receive strong and convergent excitatory afferent connections from dentate granule cells, which are their major excitation sources (Buckmaster et al., 1992). Anatomically, a single mossy cell projects to inner molecular layer and contacts many postsynaptic granule cells at ipsi-lateral hippocampus, forming 'recurrent connections'. However, Mossy cells also contact the interneurons in same lamellar which in turn inhibit the excitation of granule cells (Scharfman, 1993). Mossy cells also send axons collaterals along septotemperal axis and contact the granule cells in different lamella (West et al., 1979; Buckmaster et al., 1996). Mossy cell axons also form commissural path way which project to the granule cells at contralateral side(Ribak et al., 1985). There has been debates about the net effect of mossy cells on granule cells. Previous studies (Ratzliff et al., 2004; Jinde et al., 2012) showed increased excitability of granule cells after targeted ablation of mossy cells, indicating a general inhibitory effect of mossy cells to granule cells. The second circuit include the back-projection from CA3 pyramidal neurons (Scharfman, 1993). Such backprojection is confirmed first by histological study (Li et al., 1994) and later with simultaneously recording the excitation of hilus mossy cell and CA3 pyramidal cells after fimbria stimulation or spontaneous CA3 burst

`

(Scharfman, 1993; Scharfman, 1994). CA3 pyramidal neurons excite both mossy cells and hilar interneurons with similar latency. The back-projection is mediated by AMPA receptor. Granule cells also receive an IPSP with longer latency. However, under GABA antagonist, stimulation of fimbria will elicit EPSPs of granule cells, indicating a possible excitatory pathway from CA3- mossy cell- granule cells which is generally masked by GABAergic inhibitory neurons.

There has been many speculations about the functions of mossy cells. The two circuitries described above are important for memory formation and retrieval. Thus mossy cells is considered playing an essential role in pattern separation and cognitive functions. A computational model (Scharfman et al., 2009) also supported this opinion by comparing circuit functions with or without mossy cells. Thus it is a common opinion that the function of mossy cell is to promote the dissimilar activation of granule cells at different lamellas. However, target ablation of mossy cells in vivo (Jinde et al., 2012) only caused short term impaired cognitive functions, thus the exact role of mossy cell in hippocampal circuitry still needs more investigation.

In the present study, we use our photostimulation based functional mapping approach to map extensive synaptic connections of mossy cells through three developmental ages: P6-7, P13-14, and P21-28. Our experiments can obtain a comprehensive information on the afferent connections to mossy cells, which can help understanding the functional role of mossy cells and why mossy cells is related to epilepsy.

Methods and Materials

Hippocampal Slice Preparations

`

Sixty double transgenic Ai9-tdTomato X Gad-Cre mice were used for the experiments. We obtained one to three high quality hippocampal horizontal slices with clear Dentate Gyrus, Dentate Hilus and CA3 structure from each mouse. All animals were handled and experiments were conducted in accordance with procedures approved by the Institutional Animal Care and Use Committee at the University of California, Irvine. To prepare living brain slices, animals (postnatal days 6–7, 13-14 and 21-28) were deeply anesthetized with Nembutal (>100 mg/kg, i.p.), rapidly decapitated, and their brains removed. The occipital lobe was dissected, and 400 μm thick horizontal hippocampal sections were obtained with a vibratome (VT1200S; Leica Systems, Germany) in sucrose-containing artificial cerebrospinal fluid (ACSF) (in mM: 85 NaCl, 75 sucrose, 2.5 KCl, 25 glucose, 1.25 NaH_2PO_4, 4 $MgCl_2$, 0.5 $CaCl_2$, and 24 $NaHCO_3$). In sucrose containing ACSF (in mM: 85 NaCl, 75 sucrose, 2.5 KCl, 25 glucose, 1.25 NaH_2, PO_4, 4 $MgCl_2$, 0.5 $CaCl_2$, and 24 $NaHCO_3$). Slices were incubated for at least 30 minutes in sucrose containing ACSF at 32 °C before transferred into slice recording chambers with normal ACSF (in mM: 126 NaCl, 2.5 KCl, 26 $NaHCO_3$, 2 $CaCl_2$, 2 $MgCl_2$, 1.25 NaH_2PO_4, and 10 glucose). Throughout the cutting, incubation, and recording, the solutions were continuously supplied with 95% O_2–5% CO_2.

Electrophysiology and Laser Scanning Photostimulation

Our overall system of electrophysiological recordings, imaging, and photostimulation was previously as described in detail (Xu et al., 2010). Whole cell recordings were performed in oxygenated ACSF at room temperature under a DIC/fluorescent Olympus microscope (BX51WI). The solution was fed into the slice

recording chamber through a custom-designed flow system driven by pressurized 95% O_2–5% CO_2 (3 PSI) with a perfusion flow rate of about 2 ml/minute. Slices were first placed and carefully examined under a 4x objective for proper targeting of dentate hilus using the landmarks defined in reference (Amaral, 1978). To perform whole cell recordings, neurons were visualized at high magnification (60X objective, 0.9 NA; LUMPlanFl/IR, Olympus). Cell bodies of recorded neurons were at least 50 μm below the slice cutting surface and were initially targeted based upon the multipolar-appearance (Amaral, 1978) of the cell soma and thick apical dendrite, and later with fluorescent imaging confirming negative in Gad expression. Patch pipettes (4 – 6 MΩ resistance) made of borosilicate glass were filled with an internal solution containing (in mM) 126 K-gluconate, 4 KCl,10 HEPES, 4 ATP-Mg, 0.3 GTP-Na, and 10 phosphocreatine (pH 7.2, 300 mOsm) when measuring excitatory postsynaptic currents (EPSCs) and action potentials (APs). In separate experiments, a cesium based internal solution containing (in mM): 130 CsOH, 130 D-gluconic acid, 0.2 EGTA, 2 $MgCl_2$, 6 CsCl, 10 HEPES, 2.5 ATP-Na, 0.5 GTP-Na, 10 phosphocreatine (pH 7.2, 300 mOsm) was used to voltage clamp pyramidal neurons at the excitatory reversal potential (0 mV to 5mV) and measure inhibitory postsynaptic currents (IPSCs). Electrodes also contained 0.1% biocytin for post-hoc cell labeling and further morphological identification. Once stable whole-cell recordings were achieved with good access resistance (usually < 20 MΩ), basic electrophysiological properties were examined through hyperpolarizing and depolarizing current injections. Electrophysiological data were acquired with a Multiclamp 700B amplifier (Molecular Devices), data acquisition boards (models PCI MIO 16E-4 and 6713, National Instruments), and custom modified

`

version of Ephus software 5 (Ephus, available at https://openwiki.janelia.org/). Data were digitized at 10 kHz and stored on a computer.

During photostimulation experiments, the microscope objective was switched from 60× to 4× for laser scanning photostimulation. The same low-power objective lens was used for delivering the UV flash stimuli. Stock solution of MNI-caged-l-glutamate (Tocris Bioscience) was added to 20 ml of circulating ACSF for a concentration of 0.2 mM caged glutamate. The hippocampal slice image was acquired at the 4x objective by a high-resolution digital CCD camera, which in turn was used for guiding and registering photostimulation sites. A laser unit (DPSS Lasers) was used to generate 355 nm UV laser pulses for glutamate uncaging. Short pulses of laser flashes (1 ms, 20 mW) were controlled by using an electro-optical modulator and a mechanical shutter. The laser beam formed uncaging spots, each approximating a Gaussian profile with a width of 100 μm laterally at the focal plane. Photostimulation using caged glutamate allows for high spatial-resolution activation of action potentials restricted to a small number of neurons close to the stimulation location. Under our experimental conditions, LSPS evoked action potentials were measured from stimulation locations within 104 μm of targeted soma and occurred within 150 ms post photostimulation (Fig 2.4).

The LSPS procedures were similar to those described in references (Shepherd, 2012). The approach involves first recording from a single neuron, then stimulating at other sites, generating action potentials from neurons in those sites via LSPS guided glutamate uncaging. Voltage clamping the postsynaptic neuron allows one to determine which stimulated locations contribute synaptic input to the recorded cell.   By systematically surveying synaptic inputs from hundreds of different sites across a large

49

`

cortical region, aggregate synaptic input maps were generated for individual neurons

(Fig. 2.2). For our mapping experiments, a standard stimulus grid (16×16 stimulation

sites, 60-80 µm2 spacing, depending on the size of the slice) was used to cover the

hippocampal slices, including, DG, Hilus, CA3 and CA1. The LSPS site spacing was

empirically determined to capture the smallest predicted distance in which

photostimulation differentially activates adjacent neurons and glutamate uncaging was

delivered sequentially in a nonraster, nonrandom sequence, following a "shifting-X"

pattern designed to avoid revisiting the vicinity of recently stimulated sites (Shepherd et

al., 2003).

Figure 2.1

`
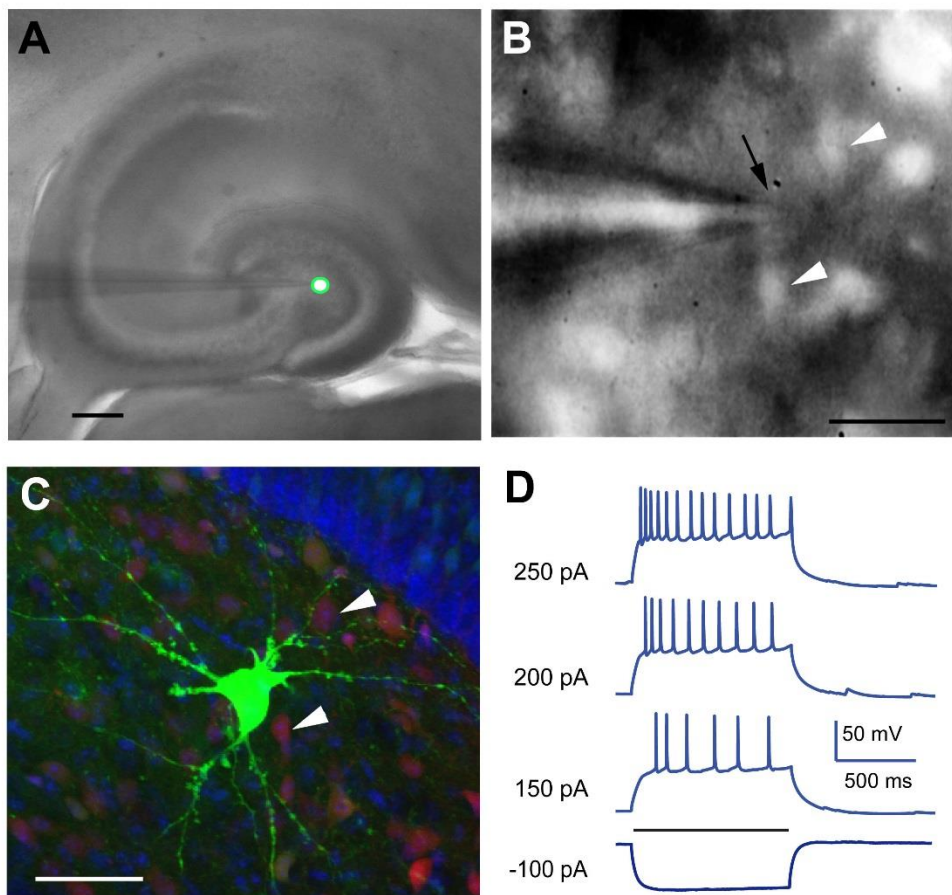
Figure 2.1. Targeted Recordings of Mossy Cells. A. A horizontal hippocampal slice acutely prepared from a GAD-Cre: Ai9 tdTomato double transgenic mouse under 4x objective with a neuron patched (in green circle). **B.** The same slice under 60x objective. The fluorescent neurons are gabaergic neurons. The neuron in the shadow is patched by glass pipette. **C.** Post reconstruction of the morphology of the patched neuron. It has multipolar shape and thick dendrites with thorny excrescences. **D.** The neuron presents regular adapting spiking when injecting current through patching pipette.

Regional Circuit Input Analysis

Photostimulation can induce two major forms of synaptic responses: (1) direct glutamate uncaging responses (direct activation of the recorded neuron's glutamate receptors); and (2) synaptically mediated responses (either EPSCs or IPSCs) resulting from the suprathreshold activation of presynaptic neurons. Excitatory and inhibitory responses within the 10 ms window from laser onset were considered direct, exhibited a distinct shape (longer rise time) and occurred immediately after glutamate uncaging (shorter latency) as demonstrated in Fig. 2.3. Synaptic currents with such short latencies are not possible because they would have to occur before the generation of action potentials in photostimulated neurons. Therefore, direct responses need to be excluded from local synaptic input analysis. However, at some locations, synaptic responses were over-riding on the relatively small direct responses and were identified and included in synaptic input analysis.

For data map analysis, we implemented a new approach for detection and extraction of photostimulation-evoked postsynaptic current responses (Shi et al., 2010), which allows detailed quantitative analyses of both EPSCs and IPSCs (amplitudes and the numbers of events across LSPS stimulation sites). Laminar and regional distributions, average input strength, and numbers of EPSCs measured in pyramidal

cells in the binocular region in V1 slices were quantified. Because of slice excitability and laser strength, measured LSPS evoked synaptic events were estimated to derive from monosynaptic sources. LSPS evoked EPSCs and IPSCs were first quantified across the 16x16 mapping grid for each map and 2 to 4 individual maps were averaged per recorded cell, reducing the likelihood of incorporating artificial synaptic events in the analysis window (150 ms). Averaged maps were then analyzed using the 4X DIC image to bin responses according to laminar cytoarchitectonic landmarks. Data was plotted as either average integrated EPSC or IPSC amplitudes and evoked EPSC and IPSC number per location (Fig. 2.5 and 2.6).

Morphological examination and Cell-type Identification

After physiological assays, brain slices were fixed in 4% paraformaldehyde overnight, then transferred to 30% sucrose solution in PBS. Slices were stained against biocytin with 1:500 Alexa Fluor 488 -conjugated streptavidin (Jackson ImmunoResearch) to visualize the morphology of the recorded cells. Slices were also stained for 4′-6-diamidino-2-phenylindole (DAPI) (Sigma-Aldrich) to identify laminar boundaries. The cell morphology was visualized using Olympus BX 61 epifluorescent microscopy and MetaMorph imaging suite (Molecular Devices).

Statistical Analysis

Data are presented as mean ± SEM. Paired t-tests were used to compare LSPS evoked synaptic events among each age group. Wilcoxon rank sum tests were used for statistical comparisons. In either test, significance was defined as $p < 0.1$.

Result

Identification of Mossy Cells

It is hard to distinguish the mossy cell and other hilar neurons through DIC image. And currently there are no transgenic mice that have mossy cells marked fluorescently. So we used a technique that could identify mossy cells in slice preparation using a combination of multiple characters. Hilar mossy cells are targeted by visualizing non-red fluorescent expression in the dentate hilus of the double transgenic Gad2-Cre:tdTomate mouse. Under 60x objective, the fluorescent neurons are gabaergic neurons and the patched neuron is in shadow, indicating potentially glutamatergic neuron (Fig 2.1B). Since there are other types of non-Gabaergic neuron in hilus, the recorded neurons are further confirmed by current injection through the recording electrode. Glutamatergic neuron should present regular adapting spiking patterns (Fig 2.1D).

After the recording, the morphology of the recorded neuron is recovered by immunocytochemical experiments using antibody against biocytin. High resolution images are obtained through confocal imaging to identify its post hoc morphological characterization. Most of recorded neurons exhibit previously reported mossy cell features, i.e. multi-polar soma, thick dendrites covered with thorny excrescences and confined in hilus (Fig 2.1C).

Intrinsic Physiology of Mossy Cells

Intrinsic physiology property was recorded immediately after successful break-in using the recording electrode. We observed obvious difference intrinsic physiology among the three age groups. First, we noticed reduced membrane resistance (Rm) with increased age (Table 1). The Rm of P6-7 mossy cell is significantly smaller from that of P13-14 and P21-28 neurons (p=0.0229 and p=0.0083). The averaged Rm of P6-7

`

mossy cell (N=11) is 669.4±176.17 comparing to 234.0±37.44 of P13-14 mossy cells

(N=12) and 192.8±36.32 of P21-28 mossy cells (N=11). The decreased Rm suggests

the formation of more effective or increased amount of ion channels. On the other hand,

the membrane capacitance increases. Given the thickness of the membrane and

membrane potential consistent across different ages, such membrane capacitance

difference represent enlarged membrane surface.

   After collecting intrinsic physiology data, we inject current to examine the

excitability for P7, P14 and P26 mossy cells. The current injection strength is 0pA, -

50pA, 50pA, 100pA and 200pA. We notice the decrease of input resistance with

increased ages with hyperpolarizing current injections (Fig 2.2A, Table 1). Such change

might indicate more excitability in the later age of mossy cells.

Table 2.1. Intrinsic Physiology of mossy cells at different ages.

Mouse age	RMP	Rs	Rm	Cm	Rinput	Evoked spike rate at 50 pA current injection
P6-7 (N = 11)	-60.3±1.68	32.6±2.38	669.4±176.17	70.4±10.30	637.7±73.99	5.6±1.10
P13-14 (N = 12)	-61.5±1.13	27.2±2.95	234.0±37.44	111.80±10.74	439.8±37.72	1.5±0.58
P21-28(N = 11)	-62.4±1.06	33.8±3.46	192.8±36.32	102.3±14.86	341.71±63.50	3.1±0.92
Significance level	n.s.	n.s.	* P6-7 vs. P13-14 0.0229 * P6-7 vs. P21-28 0.0083	* P6-7 vs. P13-14 0.0161 * P6-7 vs. P21-28 0.0845	* P6-7 vs. P13-14 0.0229 * P6-7 vs. P21-28 0.0083	* P6-7 vs. P13-14 0.0055

RMP: resting membrane potential. Rs: Access Resistance. Rm: Membrane Resistance. Cm: Membrane Capacity. Rinput: Input Resistant

Recording of Mossy Cell and data analysis

To assess the afferent input to the recorded mossy cell effectively on a large area, the

brain slice is placed under microscope for LSPS. The laser stimulation points are

superimposed on the slice image (Fig.2.3A). The LSPS system is set up as in the

methodology paper Xu et al, 2010. The LSPS method allows for much wider input

sources to be mapped to intracellular recorded neurons than paired or multiple

intracellular recordings of synaptically connected neurons, and provides a quantitative

assessment of spatial distribution and input strength of excitatory and inhibitory

connectivity to the recorded neurons. So far this technology has made considerable

contribution in understanding local circuit organization.

Figure 2.2
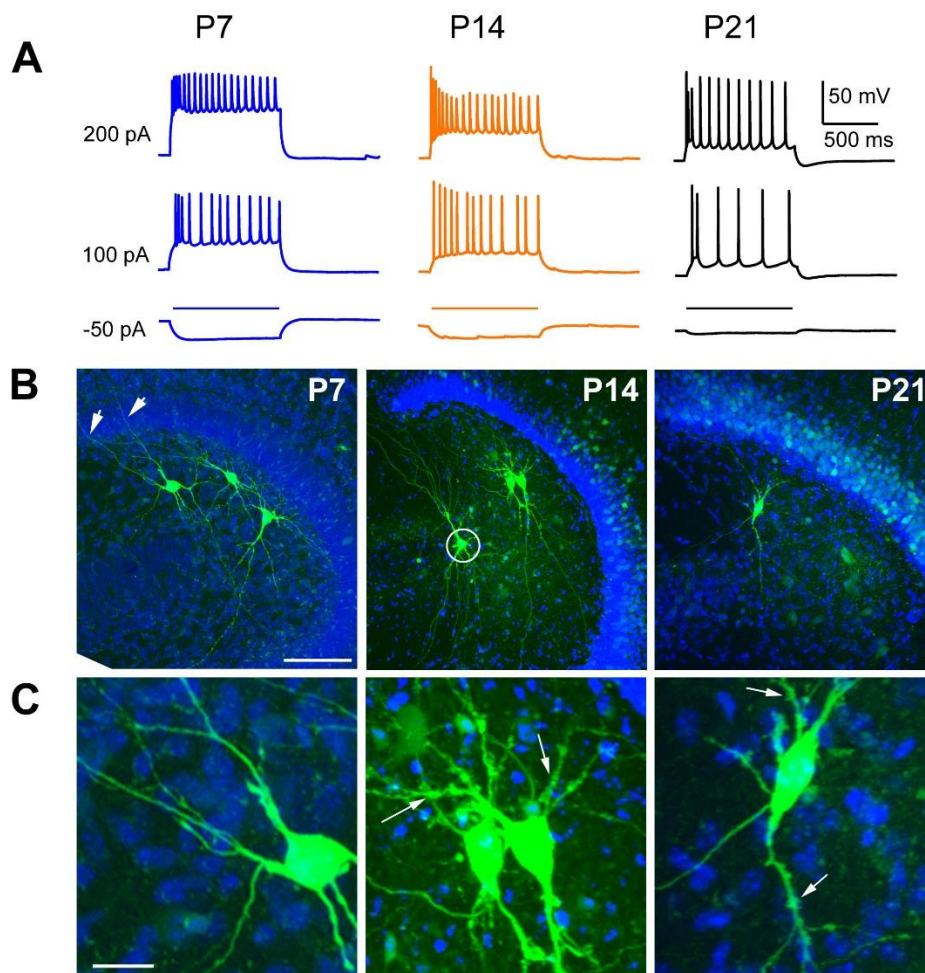
Figure 2.2. Developmental changes of intrinsic physiology. A. The example current injection responses for P7, P14 and P26 mossy cells. **B.** Biocytin-labeled recorded neurons from recorded neurons at P6-7 (left), P13-14(Middle) and P21-28(Right). The labeled neurons at P6-7 has relatively smooth proximal dendrites while neurons of P13-P14 and P21-28 have obvious thorny excrescence (pointed by arrows) on their proximal dendrites. However, all of the recovered neurons have large and multipolar soma and thick proximal dendrites.

After each LSPS trial, we can obtain a map of the raw signal traces (Fig 2.3B). Raw signal traces are characterized by the contained responses. Direct uncaging responses (Fig.2.3C upper trace) has large amplitudes with short response latencies (<10ms). And synaptic responses have smaller amplitudes and longer latencies (>10ms; Fig. 2.3C lower trace). A short detection window (10-160ms after stimulation) helps reduce the probability of detecting polysynaptic and spontaneous events. More often, the synaptic responses are superimposed with the direct response. Our novel software(Shi et al,2011) could isolate the synaptic responses from direct responses and calculate the average amplitude, integrated input, event number, first event delay, rise time and decay constant of each synaptic response. These quantitative data will be turned into color-coded map for further region specific analysis (Fig. 2.3 D, E, F).

To reduce the contamination of spontaneous event, we performed three photostimulation trials at the same laser stimulation duration. The three maps obtained from the three trials are averaged and only the sites with EPSCs or IPSCs at all three maps can be consider having presynaptic neurons.

Excitation profile of Mossy Cell

To confirm laser photostimulation resolution, we hold the neuron with I-clamp and record the action potentials elicited by laser stimulating the presynaptic cells of the recorded neurons (Fig.2.4). This experiment is normally done before obtaining

`

excitatory maps. Because Cs+ blocks K+ channel, it is not possible to obtain the

excitation profile when using internal solution when mapping inhibitory connections. To

map the distribution of photo-excitability sites, the slice was placed under 4x objective.

Then the laser scans an area that contain the whole dendritic arbors. The stimulation

pattern is normally 8X8 and centered on the recorded neurons, with the spacing ranging

from 75mm to 100mm, depending on the age of the slice. Only neurons located close

to photostimulation sites fired action potentials. To map the average distances of

photostimulation-evoked spikes from the recorded cell bodies were 115.7 ± 12.7 (N=7)

µm, 133.3 ± 26.7(N=3) µm, and 127.5 ± 8.9 (N=12) µm, respectively, for DG granule,

mossy and CA3c pyramid cells. This proves the EPSCs shown in Fig.2.4 are direct

input from stimulated pre-synaptic neurons.

Morphology development of mossy cells

After LSPS experiment, the recorded cells are immunostained with biocytin and

the morphology is recovered through confocal imaging (Fig.2.2B). From the image, we

can clearly see young neurons have relatively smooth proximal dendrites while the older

neurons show lots of thorny excrescence. This is consistent with previous histology

study using Golgi staining(Ribak et al., 1985). And another interesting fact is the

dendrites of young mossy cell penetrate fascia dentata and in older mossy cell, the

dendrites are confined in Hilus.

Excitatory Afferent input to Mossy Cell

28 mossy cells are recorded from P6-7, P13-14, P21-28 mice (N=12, 9 and 7).

After the recording, we performed region specific analysis to characterize the excitatory

input from different regions of hippocampus to mossy cell. The excitatory afferent input

57

are weak from DG at P7, and significantly increases at P14 and P21-28. Such

difference could be explained the increased amount of thorny excrescences from P7 to

P14 and P21-28, as the thorny excrescences are considered the location of mossy fiber

synapsis. Although the excitation from the entire DG decreases at P21-28, such

difference is not statistically significant. We found that Mossy cell at P7 receives

majority of its excitatory input from CA3 (Fig 2.5A), indicating strong CA3 back

projection. As the mouse gets older, the CA3 and Hilus input diminishes and mossy cell

receives more input from dentate gyrus.

Figure 2.3

A

B 1000 pA
200 ms
2
1

C UV laser
Analysis window (150 ms)
1. Direct response
200 pA
100 ms
2. Synaptic input response

E Average input strength
0   60 pA

F Number of evoked events
0   12

G Number of spontaneous events
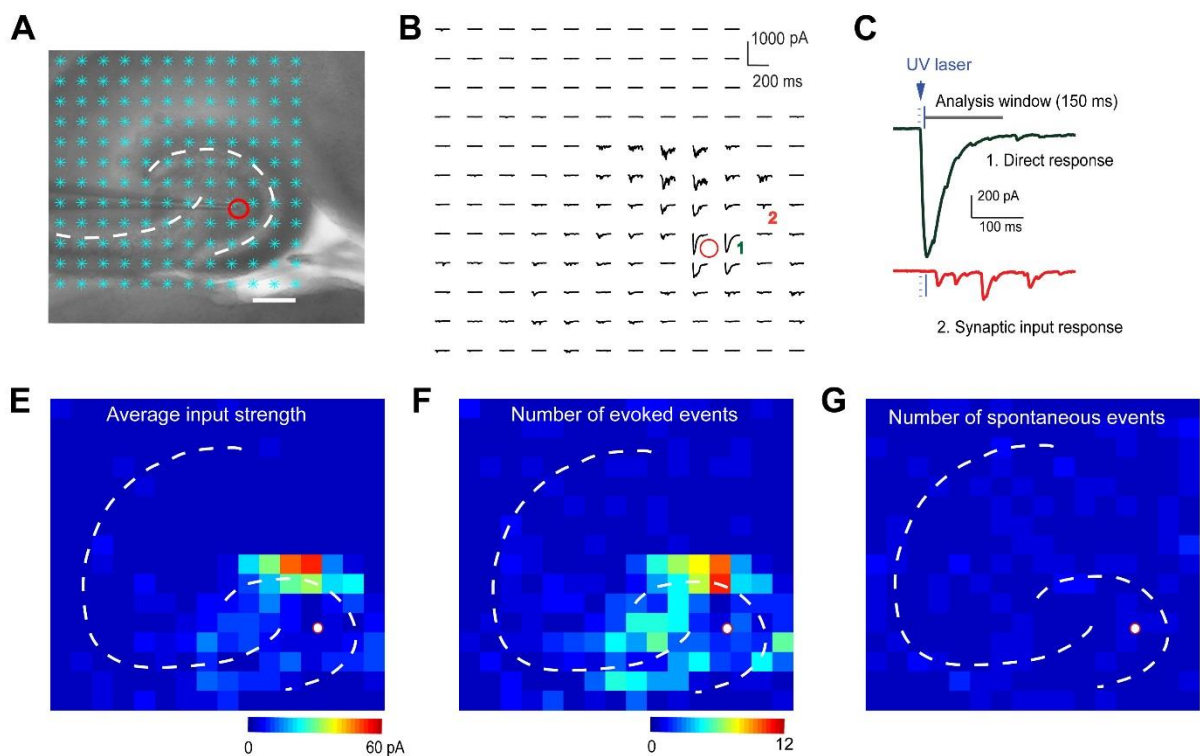
Figure 2.3. LSPS Mapping and Data Analysis. A. A horizontal hippocampal slice
under 4x objective with a neuron patched (in red circle) and Laser stimulating sites
overlapped (cyan dots). **B.** Raw signal traces of recorded from the patched neuron while
the laser is stimulating the slices. **C.** Close look of two signal traces. The green trace
contains direct response which has large amplitudes with short response latencies. The
red traces contains only synaptic responses which have smaller amplitudes and longer

58

`

latencies. **D.E.F.** The synaptic responses are detected and extracted by automatic software processing (Shi et al, 2010). Quantitative data such as Input Amplitude, Number of Events and Number of spontaneous events are calculated and turned into color-coded maps.

The recorded cells receive 44.8±8.38pA integrated excitatory input from DG at P7, 189.9±58.96 at P13-14 and 120.2±11.54 at P21-28. DG input constitutes 29.1±6.07% of the total received excitation at P7, 62.7±6.19% at P14 and 74.9±4.40% at P21-28. The per stimulation site input also increases drastically from 3.6±0.5pA at P7 to 9.6±1.51 pA and 9.6±1.88 pA at P14 and P21-28, respectively.

Comparing to the input from DG, CA3 provides more input at P7 and much less input at P14 and P21-28. The integrated input is 73.1±19.9pA at P7, 43.7±14.6pA at P14 and 13.7±4.3pA at P21-28. The average percent of evoked excitatory inputs from CA3 to mossy cells was 32.0±5.39%, 43.7±14.6% and 13.7±4.3%. The per stimulation site input also decrease from 3.7±0.5pA and 3.9±0.7 pA at P7 and P14 to 1.8±0.3 pA at P21-28.

The input from Hilus followed similar trend of CA3 input. The integrated input is 18.8±4.6pA at P7, 10.9±6.6pA at P14 and 2.6±1.0pA at P21-28. The average percent of evoked excitatory inputs from hilus to mossy cells was 18.2±6.3%, 4.8±1.73% and 2.8±1.29%. The per stimulation site input decreases from 4.1±1.0pA at P7 to 3.1±1.3 pA and 1.4±0.5 pA at P14 and P21-28, respectively.

The number of LSPS evoked EPSCs were also measured independently from EPSC strength (Fig.2.5B). The number of evoked EPSCs per stimulation site were 3.2±0.48, 3.9±0.45 and 3.5±0.13 from P7, P14, and P21-P28 from DG. The number of evoked EPSCs per stimulation site were 3.3±0.64, 1.7±0.49 and 0±00 from P7, P14, and P21-

P21-28 from Hilus. And the number of evoked EPSCs per stimulation site were

3.4±0.37, 2.4±0.27 and 1.7±0.15 from P7, P14, and P21-P28 from CA3.

We examined how fast the mossy cells receive excitatory events after stimulation. This

is important to determine the major role of mossy cell in trisynaptic circuit of

hippocampus and CA3 backprojection since mossy cell closely relate to the excitability

of DG granule cells (Scharfman, 1995). The onset of excitatory input has no significant

difference among the three age groups. And in fact, they are even similar among

different regions, i.e., DG, Hilus and CA3c (Table 2.2c).

Inhibitory Afferent input to Mossy Cell

27 mossy cells are recorded from P6-7, P13-14, P21-28 mice (N=10, 7 and 10).

After the recording, we performed region specific analysis to characterize the inhibitory

input from different regions of hippocampus to mossy cell. We found that Mossy cell at

P7 receives inhibitory input evenly from DG, Hilus and CA3 (Fig 2.6A). As the mouse

gets older, the inhibition from DG reached peak at P13-P14 and slightly reduce at later

age. However, CA3 and Hilus inhibition has no significant change during aging.

The recorded cells receive 68.5±24.0pA integrated inhibitory input from DG at P7,

490.7±100.6 at P13-14 and 280.2±36.5 at P21-28. DG input constitutes 31.2±6.07% of

the total received excitation at P7, 62.7±6.19% at P14 and 74.9±4.40% at P21-28. The

inhibition per stimulation site are 3.9±0.9pA, 12.8±1.4 pA and 8.2±0.8 pA at P6-7, P13-

14 and P21-28, respectively.

Comparing to the input from DG, CA3 provides most inhibition at P13-14 and

much less input at P14 and P21-28. The integrated input is 77.1±20.5pA at P7,

150.6±30.4pA at P14 and 82.2±14.7pA at P21-28. The average percent of evoked

`

inhibitory inputs from CA3 to mossy cells was 40.5±6.24%, 18.5±2.53% and

18.4±1.27%. The inhibition per stimulation site was 4.3±0.8pA, 10.8±2.1 pA and 6.4±0.7

pA at P6-7, P13-14 and P21-28.

Figure 2.4
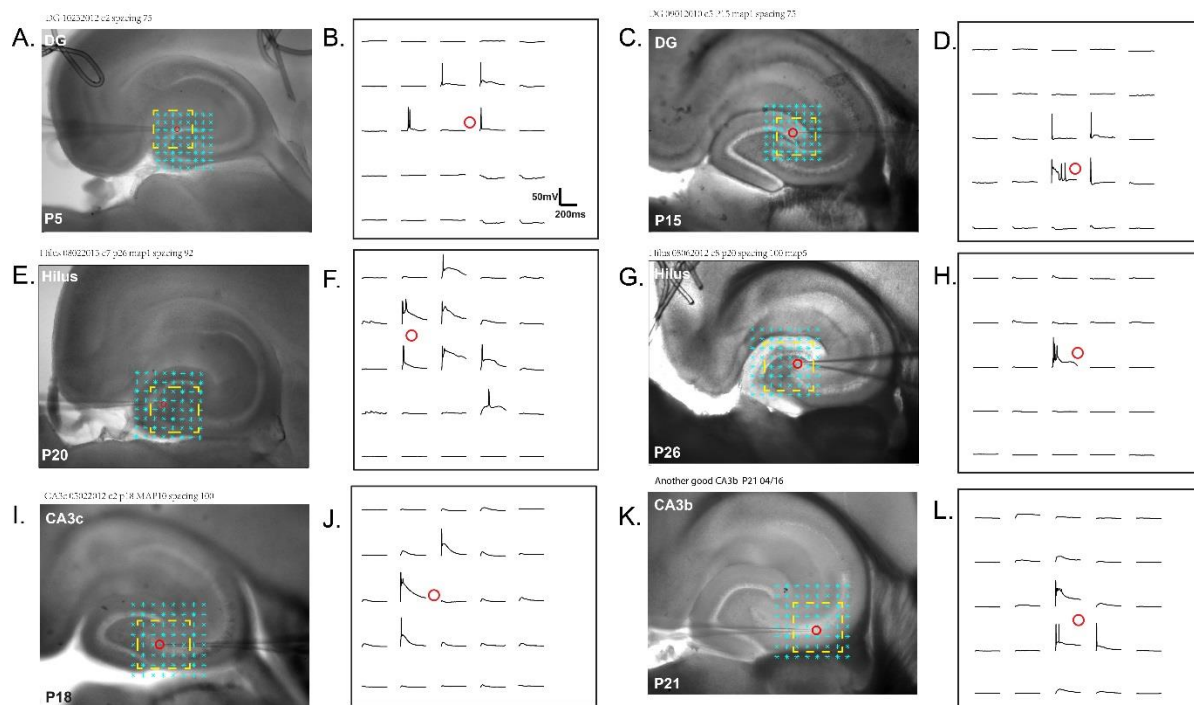
Figure 2.4. Spatial resolution of LSPS by examining the excitation profile of recorded neurons in DG, Hilus and CA3c. A-B: The excitation profile of a recorded DG granule cell from P5 mouse hippocampal slice. The excitation profile is the spatial distribution of uncaging sites that produce action potentials. The cell is held in current clamp mode. The cyan dots in **A** are the stimulation sites and spaced by 75um. The evoked action potentials are restricted in a small region (Yellow Square). The raw signal traces in the yellow square are shown in **B. C-D:** The excitation profile of a recorded DG granule cell from P15 mouse hippocampal slice. **E-H:** The excitation profile of a recorded hilar mossy cell from P26 and P20 mouse hippocampal slice. The space between stimulation points are 92um (**E-F**) and 100um (**G-H**). **I-L:** The excitation profile of recorded CA3c (**I-J**) and CA3b (**K-L**) pyramid cells from P18 and P21 mouse hippocampal slice. The space between stimulation points are 100um. The excitation profiles show no spike-evoking sites far from the perisomatic area of the recorded neuron, proving the LSPS maps represent monosynaptic inputs.

Figure 2.5
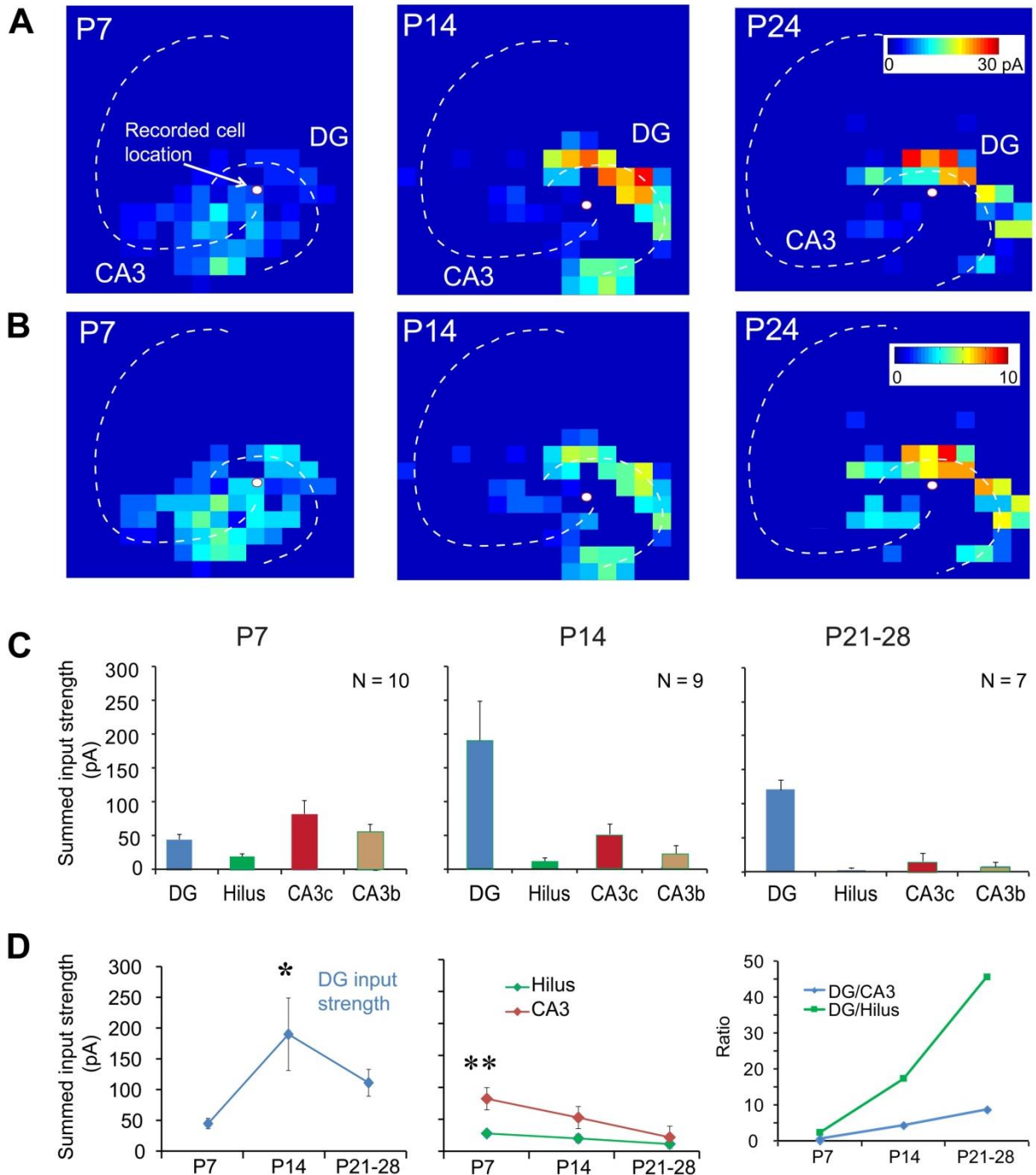
Figure 2.5 Excitatory input connections to mossy cells at different ages. A. The map of excitatory input amplitude at P7, P14 and P24. The outline of hippocampus is overlaid onto the color map. The little red circle indicates the cell soma. The warmer color indicates stronger response. **B.** the frequency of EPSC events. **C.** Averaged

`

excitatory regional input amplitude. These bar graphs plot averaged regional input amplitudes to single mossy cells. We mapped 10, 9 and 7 cells from P7 P14 and P21-p28 mice, respectively. The y-axis is the input strength. **D.** The input from CA3 and Hilus decreases as the animal ages.

The input from Hilus followed similar trend of CA3 input. The integrated input is 28.1±8.8pA at P7, 132.2±35.2pA at P14 and 38.6±5.7pA at P21-28. The average percent of evoked inhibitory inputs from hilus to mossy cells was 18.2±3.93%, 14.9±2.95% and 10.5±2.28%. The per stimulation site input was 4.7±1.3pA, 10.7±2.1 pA and 5.0±0.6 pA at P6-7, P13-14 and P21-28, respectively.

The number of LSPS evoked IPSCs were also measured independently from IPSC strength (Fig.2.6B). The number of evoked IPSCs per stimulation site were 2.0±0.40, 3.7±0.41 and 3.3±0.36 at P7, P14, and P21-P28 from DG. The number of evoked IPSCs per stimulation site were 2.6±0.59, 3.9±0.58 and 2.8±0.29 from P7, P14, and P21-28 from Hilus. And the number of evoked IPSCs per stimulation site were 2.2±0.36, 3.0±0.48 and 2.7±0.22 from P7, P14, and P21-P28 from CA3. Similar to excitatory input, we examined the onset of inhibitory input to the recorded mossy cells. The onset of IPSC decreased significantly from P6-7 to P13-14. And slightly went up at P21-28(Table 3c). This change is significant at DG and CA3.

Discussion:

The current study of mossy cell connectivity is largely influenced by anatomical observation (Ribak et al., 1985) and paired recordings (Ratzliff et al., 2004). In this study, Laser-Scanning Photostimulation combined with whole cell patch clamping and advanced software processing tool allowed us to efficiently assess both excitatory and inhibitory afferent connectivity to mossy cells at three important developmental stage of

`

mice. Our data is the first to provide a comprehensive evaluation of the circuits connection distribution and input strength of mossy cells.

Comparison of excitatory and inhibitory connections of mossy cell

Although the experimental results recapitulated that mossy cells receive strong excitatory innervations from DG granule cells in later development and adult, it is new that the DG excitation is small at p6-p7. This is consistent with the finding that thorny excrescence only appears at rather late stage(around p9) and become common at p14 in rodent (Ribak et al., 1985). Young mossy cell receive dominant excitation from CA3 back-projection, which decreased significantly in later age. The weak excitatory input from hilus might be a result of recurrent connections from other mossy cells. Such excitation disappeared in later age.

The inhibition of mossy cells comes mostly from DG and CA3. Such inhibition is weak and comes evenly from DG, Hilus and CA3. As the animal aging, the DG inhibition increased significantly and CA3 and hilus inhibition is reduced.
Both excitation and inhibition from DG peaked at P14 and slightly went down at P21-P28. Although further studies are necessary to reveal the mechanism of such reduction, it is possible due to the decreased cell density in dentate gyrus in later development (Seress, 1977; Sadgrove et al., 2006).
Mossy cells development and formation of canonical unidirectional trisynaptical circuits

It has been well know that the fundamental neuronal organization of hippocampus is DG-CA3-CA1 trisynaptic circuits. Cortical information enters Dentate Gyrus through entorhinal cortex. DG granules project to mossy cells and CA3 pyramidal

`

neurons through mossy fibers. Besides forming autoassociation network, CA3

pyramidal neurons contact CA1 pyramidal neurons through Shaffer collaterals. CA1

then send efferent connection back to entorhinal cortex. Such information flow is

considered mostly unidirectional in mature hippocampus. However, it is not always the

case, especially in immature hippocampus. In our previous study (Shi et al, 2013), we

found the bi-directional propagation of global network activity that originate in distal CA3

and propagate towards DG and CA1 at the same time in young hippocampus (P1-P14).

Such bi-directional propagation is mediated by AMPA receptor and gradually

disappeared by p14 and followed by unidirectional propagation. However, it is not clear

how such information flow is formed. In past studies, biocytin staining and paired

recording have shown axon collaterals of CA3 pyramidal neurons directly innervate the

activation of mossy cells and GABAergic neurons (Scharfman, 1993; Scharfman, 1994)

in dentate and hilus. These neurons sends axons to molecular layer and targets

Granule Cells. However, the net effect of back-projection is generally inhibitory on

granule cells. In the present study, we discovered that mossy cell receives relatively

strong back-projection from CA3 at P6-7 and such excitation diminishes at later ages. At

meantime, although the inhibition from CA3 decreases as well, the onset of inhibition

became faster than excitation at later age. Such change could block the excitation to

mossy cell and prevent them from activating granule cells, hence the formation of

unidirectional information flow.

Mossy Cell and epilepsy

Mossy cell loss has been observed both in human with temporal lobe epilepsy

and animal models. There have been a few hypothesis in attempt to connecting mossy

`

cell with epileptogenesis. However in recent study(Jinde et al., 2012) , although targeted ablation of mossy cell in vivo caused short-term hyperexcitability of granule cells, increased anxiety and impaired contextual discrimination, no spontaneous seizure is observed and most of the acute effects are back to normal in chronic phase. It is also observed that there sprouting of interneuron axons into inner molecular layer. This experiment indicates deleting mossy cells alone could not cause seizures in hippocampus since the interneuron sprouting might supplement the lost inhibition(Jinde et al., 2013).

In our previous study using voltage sensitive dye imaging, the bidirectional propagation from CA3 is mediated by AMPA receptor. Whole-cell voltage-clamp of Granule cell at p5 received strong and weak excitation when stimulating hilus and CA3, reflecting the underlying excitatory pathway from CA3 to hilus and hilus to DG. This is consistent with previous findings (Scharfman 1993). The bi-directional propagation disappears at P14, similar time of GABA transition from excitatory to inhibitory, indicating the maturation of GABA inhibitory system is possibly important for. By removing the inhibition with GABA antagonist bicuculline, the back propagation could still be observed (Nick's previous data) and stimulation of fimbria could elicit EPSP of the dentate granule cells. Granule cells also receive stronger excitation from more locations in DG, CA3 and Hilus of epileptic pilocarpine-treated rats, while such excitation is rare in control rats (Zhang, 2012). Further, the loss of SOM inhibitory neurons in Hilus after epilepsy (Peng, 2013) completely removed inhibition from Hilus to granule cells, and possible to mossy cells as well, which could be the key factor for the

`

formation of uncontrolled recurrent network between granule cells and CA3 pyramidal

cells.

Figure 2.6

`
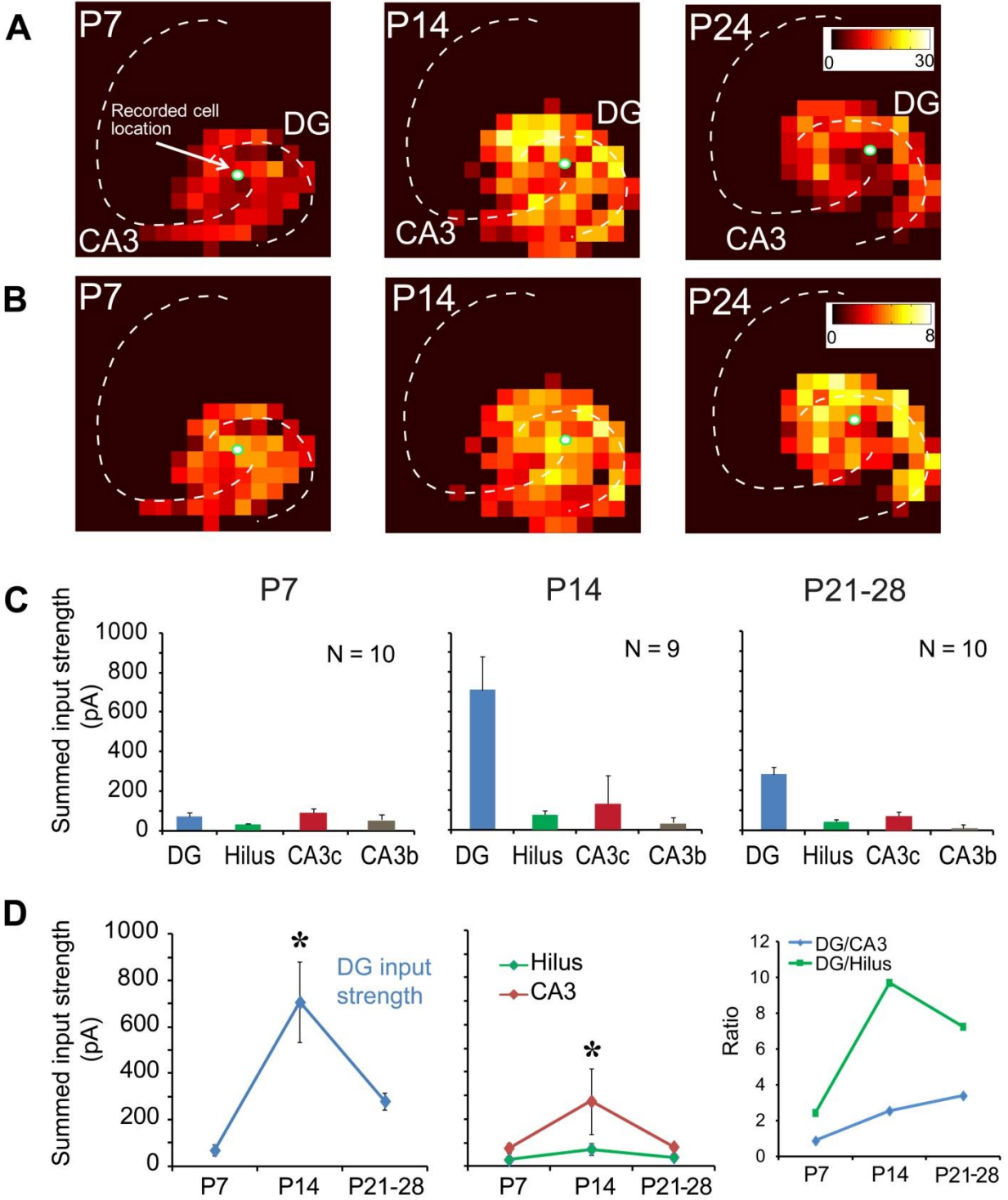
Figure 2.6. Inhibitory input connections to mossy cells at different ages. A. The map of inhibitory input amplitude at P7, P14 and P24. The outline of hippocampus is overlaid onto the color map. The little green circle indicates the cell soma. The brighter color indicates stronger response. **B.** The frequency of IPSC events**. C.** Averaged inhibitory regional input amplitude. We mapped 10, 9 and 10 cells from P7 P14 and P21-p28 mice. **D.** The input strength increased significantly at P14 and goes down at P21-28. DG provides dominant inhibition comparing to other areas.

Interestingly, although GABA is an inhibitory transmitter in adult cerebra, it might switch back from inhibitory to excitatory when large amount of GABA is released under pathologic conditions. Further, GABAergic neuron axon sprouting is observed after mossy cell deletion (Jinde, 2012). The pilocarpine-treated rats also show massive reorganization of the axons of SOM interneurons onto granule cells in hippocampus, despite large amount of neuronal loss (Peng, 2013). In this case, the gabaergic neurons might actually facilitate the formation of such recurrent excitatory network under pathologic conditions.

Conclusion

In summary, we reported both excitatory and inhibitory connectivity changes to mossy cells during the hippocampal development. And such findings could contribute in understanding formation of canonical hippocampal circuits organization and potentially the mechanism of epilepsy.

Table 2.2 Statistics of EPSC events of mossy cells at different ages
a. Averaged Integrated Input Strength of EPSC events of mossy cells at different ages.

EPSC Integrated Input					
		P6-7	P13-14	P21-28	Significance level
DG	EI	44.8±8.38	189.9±58.96	120.2±11.54	* P6-7 vs. P13-14 0.0507 * P6-7 vs. P21-28 0.00048
	EI Per Site	3.6±0.5	9.6±1.51	9.6±1.88	n.s.
	% EI	29.1±6.07	62.7±6.19	74.9±4.40	n.s.
hilus	EI	18.8±4.6	10.9±6.6	2.6±1.0	* P6-7 vs. P21-28 0.0218
	EI Per Site	4.1±1.0	3.1±1.3	1.4±0.5	n.s.
	% EI	18.2±6.3	4.8±1.73	2.8±1.29	n.s.
CA3	EI	73.1±19.9	43.7±14.6	13.7±4.3	* P6-7 vs. P21-28 0.0556 * P13-14 vs. P21-28 0.0907
	EI Per Site	3.7±0.5	3.9±0.7	1.8±0.3	n.s.
	% EI	32.0±5.39	22.4±4.59	13.8±3.88	n.s.

EI: Evoked Input.

b. Number of EPSC events of mossy cells at different ages.

EPSC Freq					
		P6-7	P13-14	P21-28	Significance level
DG	EI	38.9±7.02	70.7±21.16	51.4±10.07	n.s.
	EI Per Site	3.2±0.48	3.9±0.45	3.5±0.13	n.s
	% EI	31.2±5.04	56.6±6.37	68.3±4.21	n.s.
hilus	EI	15.1±3.38	4.9±2.48	2.6±1.10	* P6-7 vs. P13-14 0.0503 * P6-7 vs. P21-28 0.0117
	EI Per Site	3.3±0.64	1.7±0.49	0	n.s.
	% EI	13.3±4.33	5.4±2.08	3.2±1.22	n.s.
CA3	EI	60.4±13.94	25.5±8.36	12.7±3.24	* P6-7 vs. P21-28 0.0193
	EI Per Site	3.4±0.37	2.4±0.27	1.7±0.15	n.s.
	% EI	33.4±5.76	26.2±4.69	14.3±3.50	n.s.

c. Rise time, Time Constant and Onset of EPSC

		P6-7	P13-14	P21-28	Significance level
DG	Rise time(ms)	2.4±0.12	2.6±1.31	2.49±0.14	n.s.

`

	Time Constant(ms)	4.2±0.23	4.16±0.29	5.0±0.60	n.s.
	Onset(ms)	50.5±5.60	46.2±6.73	42.1±4.78	n.s.
hilus	Rise time(ms)	2.3±0.17	2.9±0.57	2.2±0.23	n.s.
	Time Constant(ms)	6.7±0.99	5.7±0.46	6.2±1.48	n.s.
	Onset(ms)	46.9±4.88	59.1±7.33	39.2±9.05	n.s.
CA3	Rise time(ms)	2.45±0.12	3.14±0.13	2.73±0.25	* P6-7 vs. P13-14 0.0038 * P13-14 vs. P21-28 0.0401
	Time Constant(ms)	7.2±0.29	4.4±0.28	3.4±0.91	n.s.
	Onset(ms)	44.1±2.99	51.0±7.41	47.2±10.25	n.s.

Table 2.3 Statistics of IPSC events of mossy cells at different ages
a. Integrated Input of IPSC events of mossy cells at different ages.

		IPSC Integrated Input			
		P6-7	**P13-14**	**P21-28**	**Significance level**
DG	EI	68.5±24.0	490.7±100.6	280.2±36.5	* P6-7 vs. P13-14 0.00041 * P6-7 vs. P21-28 0.00079
	EI Per Site	3.9±0.9	12.8±1.4	8.2±0.8	n.s.
	% EI	31.2±5.54	62.3±5.00	64.1±2.93	n.s.
hilus	EI	28.1±8.8	132.2±35.2	38.6±5.7	n.s.
	EI Per Site	4.7±1.3	10.7±2.1	5.0±0.6	n.s.
	% EI	18.2±3.93	14.9±2.95	10.5±2.28	n.s.
CA3	EI	77.1±20.5	150.6±30.4	82.2±14.7	n.s.
	EI Per Site	4.3±0.8	10.8±2.1	6.4±0.7	n.s.
	% EI	40.5±6.24	18.5±2.53	18.4±1.27	n.s.

b. Number of IPSC events of mossy cells at different ages.

		IPSC Freq			
		P6-7	**P13-14**	**P21-28**	**Significance level**
DG	EI	32.6±11.70	105.3±21.12	111.6±14.46	* P6-7 vs. P13-14 0.0136 * P6-7 vs. P21-28 0.0028
	EI Per Site	2.0±0.40	3.7±0.41	3.3±0.36	n.s.
	% EI	31.1±5.57	56.3±4.82	60.8±1.92	n.s.
hilus	EI	15.15±4.18	35.38±9.79	21.3±2.80	n.s.
	EI Per Site	2.6±0.59	3.9±0577	2.8±0.29	n.s.
	% EI	19.3±3.89	17.1±2.60	13.1±2.16	n.s.
CA3	EI	36.2±9.14	44.3±13.16	33.8±4.40	n.s.
	EI Per Site	2.2±0.36	3±0.48	2.7±0.22	n.s.
	% EI	39.3±6.43	19.9±2.69	18.6±0.93	n.s.

c. Rise time, Time Constant and Onset of IPSC

		P6-7	**P13-14**	**P21-28**	**Significance level**
DG	Rise time(ms)	4.1±0.25	4.0±0.23	4.4±0.18	n.s.

	Time Constant(ms)	9.3±0.06	7.7±0.78	7.4±0.33	P6-7 vs. P21-28 0.0167
	Onset(ms)	57.1±2.17	34.8±1.55	40.2±2.53	* P6-7 vs. P13-14 0.0003108 * P6-7 vs. P21-28 0.0000938 * P13-14 vs. P21-28 0.0702
hilus	**Rise time(ms)**	4.6±0.27	4.4±0.27	4.8±0.16	n.s.
	Time Constant(ms)	7.3±0.00	7.7±1.04	9.4±0.83	n.s.
	Onset(ms)	39.3±6.46	28.7±4.27	33.0±2.93	n.s.
CA3	**Rise time(ms)**	4.4±0.28	3.5±0.35	4.5±0.22	* P6-7 vs. P13-14 0.051 * P13-14 vs. P21-28 0.025
	Time Constant(ms)	8.8±0.11	7.0±0.78	8.6±0.64	n.s.
	Onset(ms)	61.5±6.25	34.0±4.53	35.8±2.50	* P6-7 vs. P13-14 0.0079 * P6-7 vs. P21-28 0.003

`

Chapter 3
Novel use of matched filtering for synaptic event detection and extraction

Efficient and dependable methods for detection and measurement of synaptic events are important for studies of synaptic physiology and neuronal circuit connectivity. As the published methods with detection algorithms based upon amplitude thresholding and fixed or scaled template comparisons are of limited utility for detection of signals with variable amplitudes and superimposed events that have complex waveforms, previous techniques are not applicable for detection of evoked synaptic events in photostimulation and other similar experimental situations. Here we report on a novel technique that combines the design of a bank of approximate matched filters with the detection and estimation theory to automatically detect and extract photostimluation-evoked excitatory postsynaptic currents (EPSCs) from individually recorded neurons in cortical circuit mapping experiments. The sensitivity and specificity of the method were evaluated on both simulated and experimental data, with its performance comparable to that of visual event detection performed by human operators. This new technique was applied to quantify and compare the EPSCs obtained from excitatory pyramidal cells and fast-spiking interneurons. In addition, our technique has been further applied to the detection and analysis of inhibitory postsynaptic current (IPSC) responses. Given the general purpose of our matched filtering and signal recognition algorithms, we expect that our technique can be appropriately modified and applied to detect and extract other types of electrophysiological and optical imaging signals.

`

Introduction

Neurons in the brain and nervous system in general communicate with one another by forming connections mostly through synapses. Typical neurophysiological studies involve experimental recordings from many neurons, and may require detailed examination and analysis of synaptic events. For example, laser scanning photostimulation experiments are effective for mapping local circuit inputs to individually recorded neurons (Callaway and Katz, 1993; Weiler et al., 2008; Xu and Callaway, 2009), as simultaneous whole-cell recordings from a postsynaptic neuron with photostimulation of clusters of presynaptic neurons (via glutamate uncaging) at many different locations provide quantitative measures of spatial distribution of excitatory and inhibitory inputs impinging onto individually recorded neurons. Similar to most other synaptic physiological analyses, photostimulation data analysis involves identification and detection of hundreds of response traces that are recorded from each individual cell. Although photostimulation maps of synaptic inputs can be constructed by simply averaging postsynaptic current amplitudes within a response window (Shepherd and Svoboda, 2005; Jin et al., 2006; Weiler et al., 2008; Xu and Callaway, 2009), a more comprehensive understanding of synaptic connectivity requires detection of individual synaptic events and measurement of parameters such as event occurrence times, amplitudes and frequencies (Yoshimura and Callaway, 2005; Yoshimura et al., 2005). While the human detection of these events is typically aided by software applications, the process is still laborious and time-consuming, which precludes efficient treatment of large datasets (Dantzker and Callaway, 2000; Yoshimura et al., 2005).

Table 3.1. Quantitative analysis of photostimulation-evoked EPSCs recorded from excitatory pyramidal cells and FS cells.

	EPSC peak amplitude (median, pA)	EPSC rise time (median, ms)	mean EPSC frequency (Hz) across photostimulation sites	The latency of first detected EPSC per site (median, ms)
excitatory pyramidal cells	35.66 ± 2.31 (mean ± SE)	4.7 ± 0.31	4.37 ± 0.59	42.4 ± 5.23
fast-spiking (FS) inhibitory cells	50.77 ± 2.84	2.93 ± 0.73	7.87 ± 1.49	37.9 ± 4.82

*Note that the data summary is based upon automated detection and measurement of 689 and 1076 evoked EPSCs from excitatory pyramidal cells and FS cells (N = 3 each) recorded in the deep layers of the prelimbic area, respectively.

As automated detection of synaptic events is of practical importance to

experimental neuroscience, several different approaches (particularly for detection of

spontaneous synaptic events) have been developed, where detection algorithms are

based upon amplitude thresholding, and fixed or scaled template matching (Liao et al.,

1992; Cochran, 1993; Abdul-Ghani et al., 1996; Clements and Bekkers, 1997; Hwang

and Copenhagen, 1999; Li et al., 2007). An unpublished method (http://huguenard-

lab.stanford.edu/public/) noted in (Jin et al., 2006) could detect photostimulation-evoked

EPSCs based upon the estimated EPSC differentiation window sizes and event

amplitudes, which need to be carefully adjusted and tested on recorded traces of each

map to ensure detection of synaptic events. However, these algorithms are found to be

of limited utility for detection of signals with variable amplitudes and superimposed

events that have complex waveforms (Clements and Bekkers, 1997; Hwang and

`

Copenhagen, 1999); thus they are not optimal for detection of evoked synaptic events in

photostimulation and other similar experimental situations.

Figure 3.1
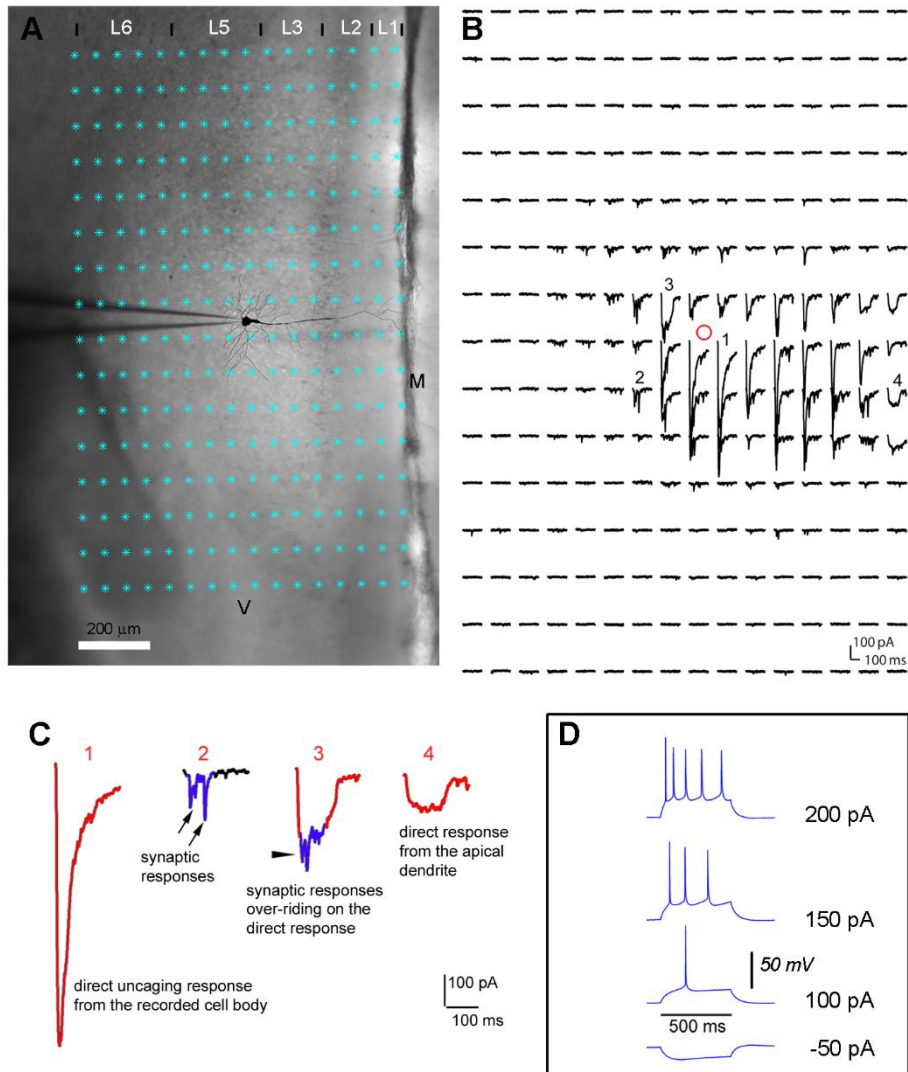
Figure 3.1. Laser scanning photostimulation combined with whole cell recordings to map local circuit input to an excitatory pyramidal neuron. A shows a mouse prefrontal cortical slice image with the superimposed photostimulation sites (16 x 16 cyan stars, spaced at 60 μm x 100 μm) across all the cortical layers 1, 2, 3, 5 and 6 (i.e., L1-L6). Note that the prefrontal cortex lacks granular layer 4 found in primary sensory cortex. The glass electrode was recording from an excitatory pyramidal neuron (shown with a scaled reconstruction with major dendrites) in upper layer 5 of the prelimbic area in prefrontal cortex. M denotes medial, and V denotes ventral. B shows an array of photostimulation-evoked response traces from most locations shown in A, with the cell held at -70 mV in voltage clamp mode to detect inward excitatory synaptic

`

currents (EPSCs). The red circle indicates the cell body location. Only the 200 ms of the recorded traces after the onset of laser photostimulation (1 ms, 25 mW) are shown. Different forms of photostimulation responses are illustrated by the traces of 1, 2, 3 and 4, which are expanded and separately shown in C. Trace 1 is an example of the direct response (shown in red) to glutamate uncaging on the cell body. Trace 2 is a typical example of synaptic input responses (blue). Trace 3 shows synaptic responses (blue) over-riding on the relatively small direct response (red) evoked from the cell's proximal dendrites. Trace 4 is another form of direct response (red) evoked from apical dendrites. D shows the pyramidal cell's intrinsic firing pattern with its voltage response traces to current injections at amplitudes of -50, 100, 150 and 200 pA, respectively.

In the present study we introduce a novel technique for detection and extraction of photostimulation-evoked excitatory postsynaptic currents (EPSCs) from individually recorded neurons in cortical circuit mapping experiments. Our technique is motivated by the observation that a matched filter represents a detector that maximizes the signal-to-noise ratio (SNR) (Kay, 1998). In other words, if a noisy time series is match-filtered, the time samples that contain a signal of interest are amplified while those containing noise are suppressed, which then facilitates the separation of signal and noise in the filtered time series. To synthesize such a filter, the signal to be detected must be perfectly known so that the filter can be matched to the signal, which is not possible in most experimental situations. To circumvent this constraint, our technique starts with a training stage, where several high-SNR EPSCs are identified by a human operator and fitted by polynomial models to build an array (bank) of approximate matched filters (templates). The filter bank provides a rich class of waveforms that potentially match those of EPSCs found in experimental recordings, thereby increasing the likelihood of their detection. In the fully automated detection stage, experimental data traces are filtered in the time domain with the polynomial templates obtained in the training stage. This amounts to convolving the data traces to be analyzed with the templates, with

76

candidate EPSCs having a better match with the templates and thus yielding larger convolution amplitudes. To detect EPSCs, the convolution traces are then compared to an event detection threshold and candidate EPSCs are localized and extracted by using statistical parameters estimated in the training stage.

The paper presents novel EPSC detection and extraction algorithms, as well as technical implementation details. The sensitivity and specificity of the method were first evaluated on simulated data, and subsequently validated on experimental data by comparing its performance to that of visual event detection performed by human operators. We also extended this method to the detection and analysis of inhibitory postsynaptic current (IPSC) responses. Finally, this new technique was applied to quantify and compare photostimulation-evoked EPSCs obtained from excitatory pyramidal cells and fast-spiking interneurons.

Methods and Materials

Experimental recordings

Wild-type C57/B6 mice were used in the experiments. All animals were handled and experiments were conducted in accordance with the protocol (#2008-2796) approved by the Institutional Animal Care and Use Committee at the University of California, Irvine. To prepare living brain slices, animals (postnatal day 17–23) were deeply anesthetized with pentobarbital sodium (>100 mg/kg, i.p.), rapidly decapitated, and their brains were removed. Coronal sections of prefrontal cortex were cut 400 μm thick with a vibratome (VT1200S, Leica Systems) in sucrose-containing artificial cerebrospinal fluid (ACSF) (in mM: 85 NaCl, 75 sucrose, 2.5 KCl, 25 glucose, 1.25 NaH2PO4, 4 MgCl2, 0.5 CaCl2, and 24 NaHCO3). Slices were first incubated in

`

sucrose-containing ACSF for 30 min to 1 h at 32°C, and then transferred to recording

ACSF (in mM: 126 NaCl, 2.5 KCl, 26 NaHCO3, 2 CaCl2, 2 MgCl2, 1.25 NaH2PO4, and

10 glucose) at room temperature. Throughout incubation and recording, the slices were

continuously bubbled with 95% O2-5% CO2.

Cortical slices were visualized with an upright microscope (BW51X, Olympus)

with infrared differential interference contrast optics. Electrophysiological recordings,

photostimulation, and imaging of the slice preparations were done in a slice perfusion

chamber mounted on a motorized stage of the microscope. An aliquot of MNI-caged-L-

glutamate (4-methoxy-7-nitroindolinyl-caged L-glutamate, Tocris Bioscience, and

Ellisville, MO) was added to 20–25 ml of circulating ACSF for a concentration of 0.2 mM

caged glutamate. To perform whole cell recording, cells were visualized at high

magnification (60x objective, 0.9 NA; LUMPlanFl/IR, Olympus). Neurons were patched

with borosilicate electrodes and recorded at room temperature. The patch pipettes (4–6

MΩ resistance) were filled with an internal solution containing (in mM) 126 K-gluconate,

4 KCl, 10 HEPES, 4 ATP-Mg, 0.3 GTP-Na, and 10 phosphocreatine (pH 7.2, 300

mOsm). For some recordings in which IPSCs were measured, potassium in the internal

solution was replaced with cesium. The internal solution also contained 0.1% biocytin

for cell labeling and morphological identification. Once stable whole cell recordings

were achieved with good access resistance (usually <20 MΩ), the microscope objective

was switched from 60x to 4x for laser scanning photostimulation. At low magnification

(4x objective lens, 0.16 NA; UplanApo, Olympus), the slice images were acquired by a

high-resolution digital CCD camera (Retiga 2000, Q-imaging, Austin, TX) and used for

guiding and registering photostimulation sites in cortical slices.

Figure 3.2
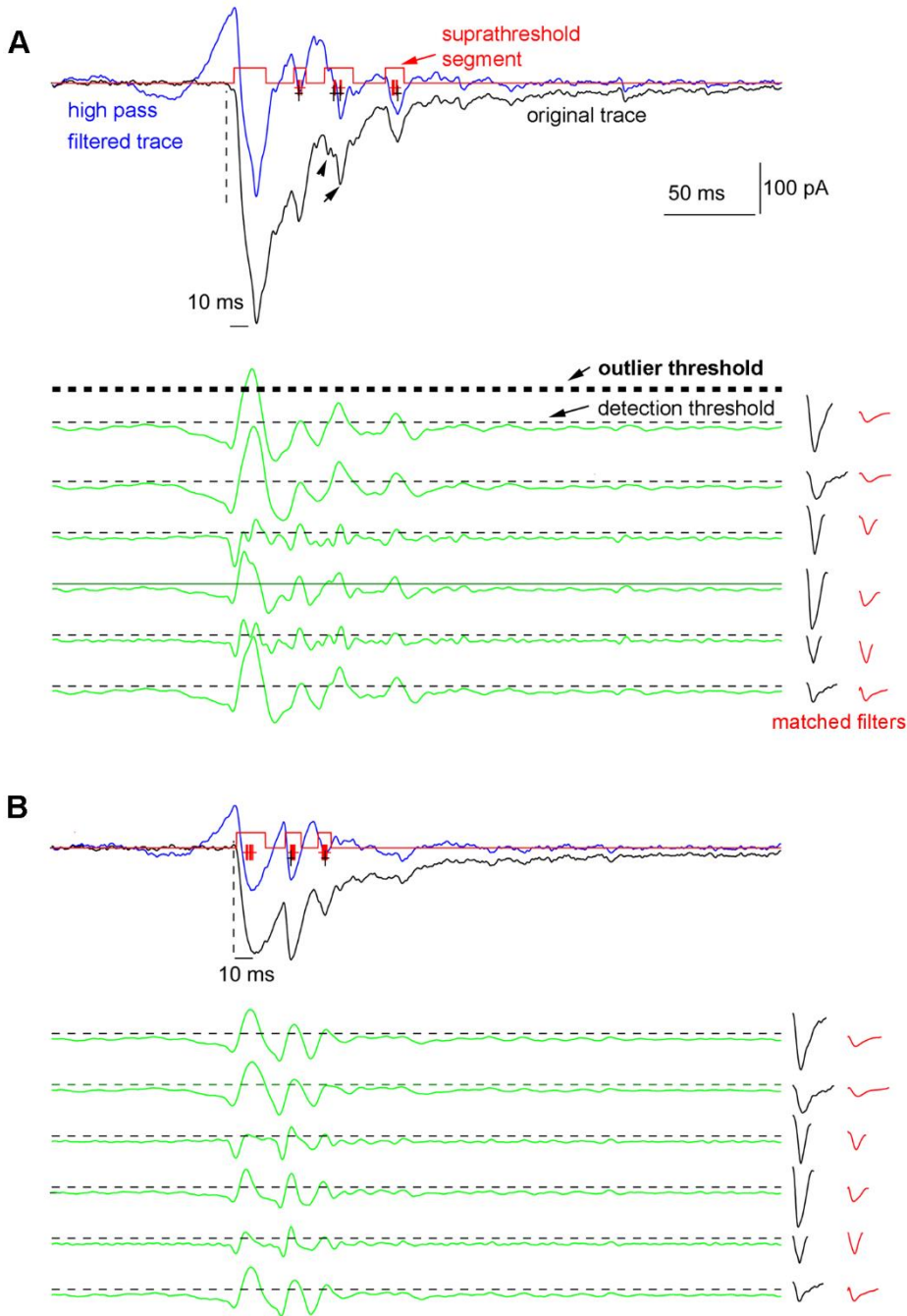
Figure 3.2 Detection of EPSCs with matched filters. A. In the top portion, the original and high-pass filtered traces are aligned. The raw trace, which is high-pass filtered with a Butterworth filter, contains a large direct response and synaptically mediated responses. The vertical dashed line indicates the photostimulation laser onset. The direct response window is defined as 10 ms within the laser onset. The filtered data trace is convolved with all the filters (a total of 18 matched filters in this

79

case) from the bank, and the convolution traces (one for each filter) are compared to a threshold. In the bottom portion of A are shown 6 example convolution traces (green) produced with 6 matched filters (red) and their original EPSC templates (black). The detection threshold (dashed) is chosen as μ- 1.2σ (11 pA), where μ is the mean value (28.4 pA) of c_{max} obtained in the training stage from the bank of 18 filters and σ is its standard deviation (14.5 pA). All the samples of the convolution traces that cross the detection threshold form the suprathreshold segments (red squares); each trace may has its own set of suprathreshold segments. The red crosses illustrate the centers of mass of the suprathreshold segments and represent potential EPSC occurrence times, while the black crosses are determined as identified EPSC peaks. As the arrow heads point out, more than one EPSCs can be identified within one suprathreshold segment. As the convolution values of the direct response are large and exceed the outlier threshold, defined as μ + 4 σ (86 pA) within W ms (i.e., 30 ms) after the laser onset, the direct response is not detected as an EPSC response. B is similarly formatted as A, and shows another example to detect both a direct response and synaptically mediated responses. The direct response in B is relatively small, and its peak values of the convolution traces do not exceed the outlier threshold. But the response is correctly identified as a direct response, because the leading edge of the response is located within the 10 ms direct response window.

The design of our laser scanning photostimulation system has been described previously (Xu et al., 2010). A laser unit (model 3501, DPSS Lasers, Santa Clara, CA) was used to generate a 355 nm UV laser for glutamate uncaging. Various laser stimulation positions were achieved through galvanometer-driven X-Y scanning mirrors (Cambridge Technology, Cambridge, MA), as the mirrors and the back aperture of the objective were in conjugate planes, thereby translating mirror positions into different scanning locations at the objective lens focal plane. During mapping experiments, photostimulation was applied to 16 x 16 patterned sites (centered at the recorded neuron) in a nonraster, nonrandom sequence, while whole-cell voltage-clamp recordings were made from the recorded postsynaptic neurons with EPSCs and IPSCs measured at the holding potential of -70 mV and 0 mV, respectively, across photostimulation sites. Data were acquired with a Multiclamp 700B amplifier (Molecular Devices, Sunnyvale, CA), data acquisition boards (models PCI MIO 16E-4 and 6713,

`

National Instruments, Austin, TX), and custom-modified version of Ephus software

(Ephus, available at https://www.ephus.org/). Data were low-pass filtered at 2 kHz

using a Bessel filter, digitized at 10 kHz, and stored on a computer. For more detailed

electrophysiology and photostimulation procedures, please refer to previously published

studies (Xu and Callaway, 2009; Xu et al., 2010).

Figure 3.3
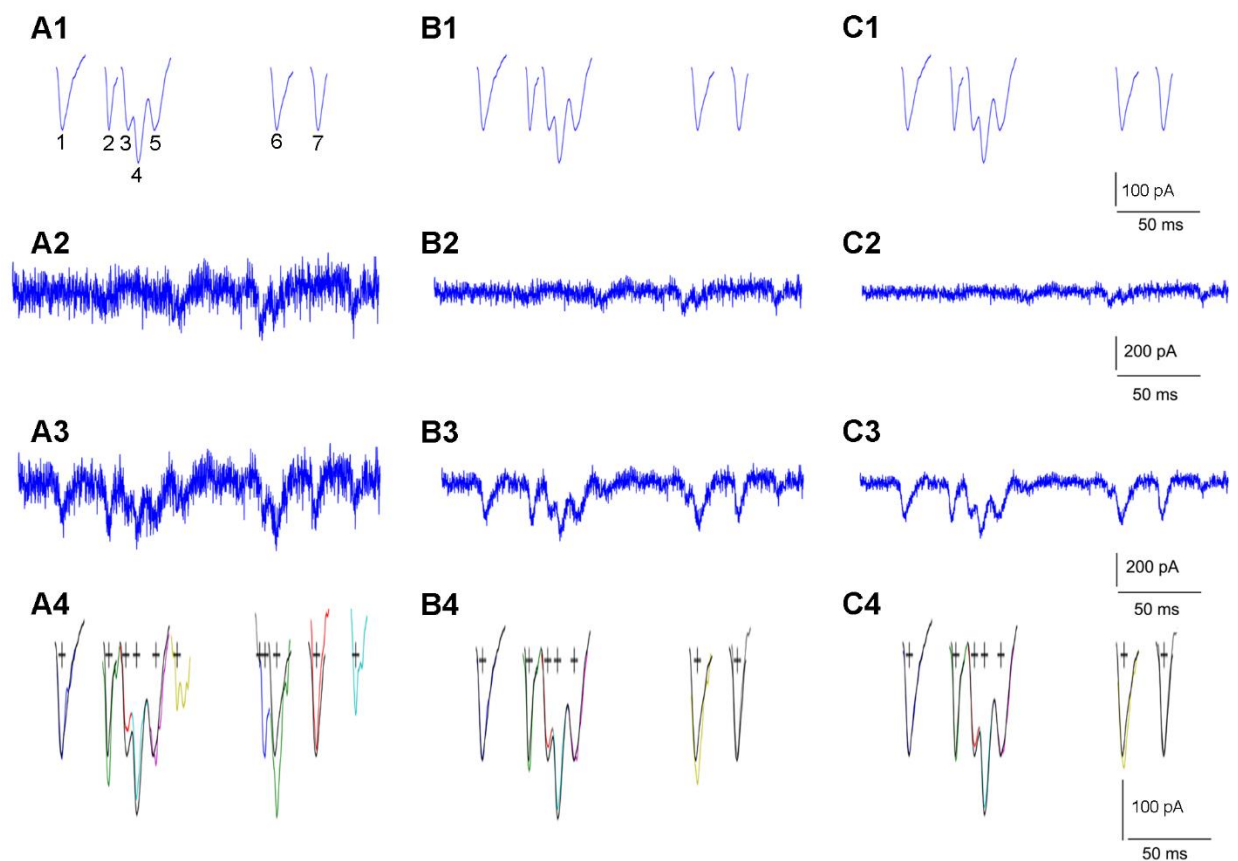
Figure 3.3 Simulated neural data and detection examples. A1, B1 and C1 are the
same set of test templates (EPSC examples) acquired from experimental recordings,
normalized to their peak amplitudes. Within this set of templates, simulated EPSCs of
1, 2, 6 and 7 are distributed as individual, non-overlapping events, while simulated
EPSCs of 3, 4 and 5 overlap and take place as one complex and overlapping response.
A2, B2 and C2 are the baseline spontaneous activity (noise) trace, with noise variances
scaled to the test template amplitude with different SNRs. A3, B3 and C3 are simulated
data traces by superimposing the template events with different degrees of noise. A4,
B4 and C4 show EPSC detection results (color coded, with the estimated arrival time

marked as '+') through convolving the simulated data traces in A3, B3 and C3 with 10 matched filters, respectively. The original EPSC template events (black, as shown in A1, B1, C1), are plotted for evaluating software detection. The detection procedure uses a detection threshold at μ + 3σ (3 standard deviations from the mean of the maximal template convolution values of the filters), and uses an amplitude cutoff of 60 pA, which is about 25% of the peak values of the individual test templates.

Design of matched filters, and EPSC detection and extraction algorithms

Figure 3.4
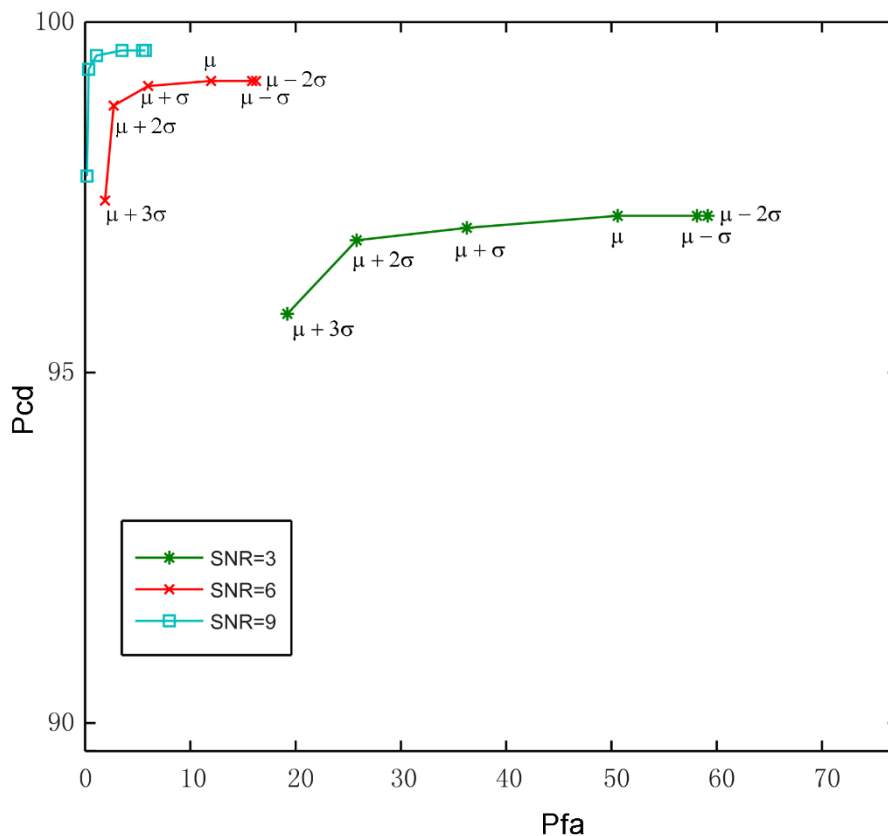
Figure 3.4. Detection performance evaluation on simulated data by using Receiver Operating Characteristic (ROC) curve analysis. The horizontal axis shows the probability of false alarm (Pfa), and the vertical axis shows the probability of correct detection (Pcd). Each ROC curve represents the software PSC detection performance at a fixed SNR (3, 6 or 9) with different detection thresholds. The detection thresholds ranges from – 2σ to 3σ from the mean of the maximal template convolution values. The ROC curve for each combination of the detection threshold and SNR was calculated by averaging the performance over 200 trials.

82

`

Our detection method consists of two stages: (i) the design of matched filters (templates); and (ii) the fully automated event detection with established filters. In the filter design stage, referred to as the training stage, the user presents the algorithm with examples of identified EPSCs, based on which templates and statistical parameters of their waveforms are estimated and stored. In the detection stage, the templates and parameters obtained in the training stage are used to detect EPSCs.

Training Stage: In the training stage, the user identifies raw experimental data traces that contain evoked EPSCs that are sufficiently strong with respect to background noise; and the user is prompted to manually mark evoked EPSCs. This procedure typically involves sequential selection of several synaptic responses with different shapes, durations and amplitudes. The onset of the EPSC should be taken as the point where the signal starts falling sharply from the baseline. Similarly, the offset point should be the point where the signal returns to baseline. The onset and offset points should be at a similar baseline level. If this condition is violated (presumably due to a high noise level or direct response contamination), it is recommended that a new EPSC be used for training. Superimposed EPSCs are not appropriate to be used for training. An 8-th order polynomial model is fitted through the segment of each identified EPSC, normalized by its L_1 norm [The L1 norm of a vector $x = [x_1, x_2, \dots, x_n]$ is defined as: $\|x\|_1 = \sum_{i=1}^{n}|x_i|$.], and saved as a template (approximate matched filter) for the detection stage. The normalization is necessary to minimize the dependence of EPSC detectability on the filter amplitude. While EPSCs from a single synaptic event are typically modeled using exponential functions (Nenadic et al., 2000; Nenadic et al., 2002; Nenadic et al., 2003; Li et al., 2007), most of photostimulation-evoked EPSCs appear to represent

`

compound responses of multiple synapses, and the exponential models proved

inadequate. The 8-th order polynomial model, however, provided an excellent fit, given

the sampling rate of 10 kHz and the mean duration of EPSCs of ~14 ms. While our

method and its software implementation allow the user to change the order of the

model, choosing polynomials of higher order may result in overfitting. Several

parameters are then calculated and stored for further analysis, including the duration of

the EPSCs, defined by manual mouse clicks, and the duration of the leading and trailing

parts of EPSCs, defined as the absolute value of the difference between the time of the

(negative) peak of the selected EPSC and its onset and offset, respectively. In addition,

the amplitude of the selected EPSC, defined as the difference of the amplitude value at

the onset and peak time of the EPSC, is calculated. Finally, the selected raw EPSC is

convolved with the yielded template and the maximum value of the convolution signal,

$c_{\max}$, is logged. The purpose of this step is to obtain the statistics of convolution

amplitudes for the detection stage. Due to the presence of noise and the fact that

EPSCs are asymmetric, there is typically a time shift between the peaks of convolution

and EPSC traces, and the shift value is also recorded and stored. The role of these

parameters will be precisely defined in the detection stage. The whole procedure is

then repeated with a different trace or a different EPSC within the same trace, which

amounts to building a bank of approximate matched filters for the detection stage. A

minimum recommended number of filters in the bank is 10, although 18 filters were

used in the present study. In addition to increasing the likelihood of detecting EPSCs

with various shapes and durations, multiple templates allow the statistics of the above

parameters to be estimated more accurately. Subsequently, based on these

`

parameters, detection thresholds and safeguards against false detection can be set in a

statistically meaningful manner. It should be noted that the user's involvement only

includes selecting EPSCs with mouse clicks, and that all subsequent calculations are

automated. Typical time necessary to obtain the filter bank and the associated

parameter statistics is less than 10 min. It should also be noted that templates and

parameters trained on a data set from one experiment can often be used for detection

of EPSCs in other similar experiments.

Figure 3.5
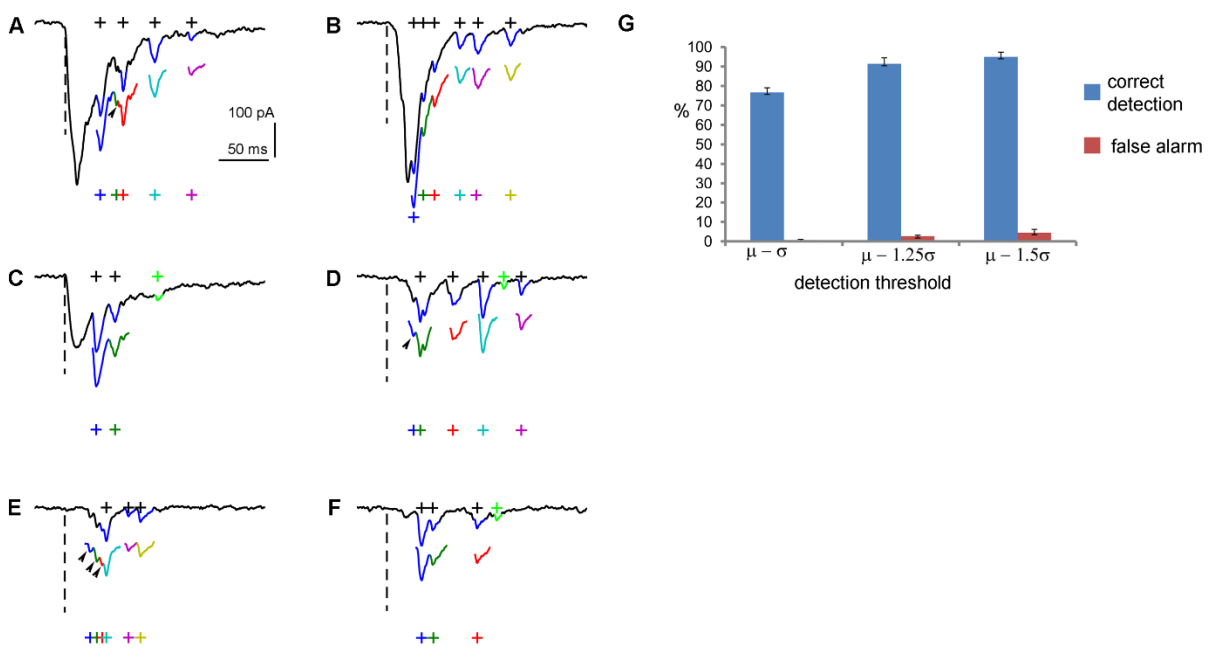
Figure 3.5. Analysis of experimental data through matched filtering. A-F: Typical examples of detection and extraction of photostimulation-evoked EPSCs, in comparison with human visual detection.   The raw data traces were shown in solid back, with the overlaying segments of EPSCs (blue) identified by an experienced human operator. The black crosses indicate the center of the human selected EPSCs. The color-coded segments shown below the raw data traces are detected and individually extracted EPSCs through matched filtering, with the respective crosses indicating the detected EPSC centers. The arrows and arrow heads point to the extra events correctly detected by the software, but missed by the human. The weak EPSCs (with the amplitudes of < 20 pA, about the spontaneous EPSC level) (green) identified by the human are missed by the automated detection, because of the pre-set amplitude cutoff (20 pA). G: the bar

graph summarizing the percentage of correct detection and percentage of false alarm of the automated detection of EPSCs across different data sets (N = 3), using the same filter bank at multiple detection thresholds (μ-1σ, μ-1.25σ and μ-1.5σ). The values are presented as mean ± SE. Each data set contained more than 200 photostimulation-evoked EPSCs, and the detection results were inspected and verified by a human operator.

Detection Stage: In the detection stage, the arrival (occurrence) times of

candidate EPSCs are found and processed, and short segments of data around the

estimated occurrence times are extracted for further analysis. Specifically, the data

trace under investigation is first high-pass filtered (>10 Hz) with a 5th order, infinite

impulse response Butterworth filter. The role of this filter is to minimize the effect of the

direct uncaging response (see Results), whose duration is much longer than that of

synaptically mediated indirect responses (EPSCs). To minimize the phase distortions,

this filter is implemented as a zero-phase forward and reverse digital filter (Oppenheim

and Schafer, 2009). The high-pass filtered signal is then convolved with all the filters

from the bank, and the convolution traces (one for each filter) are time-shifted to

minimize the difference between the time of the convolution peak and a potential EPSC

peak, and thus facilitate a more precise estimation of EPSCs' occurrence times. The

applied time shifts are those recorded in the training stage (see above). Time-shifted

convolution traces are then compared to a detection threshold. For experimental data,

this threshold is typically chosen between $\mu - 1.5\sigma$ and $\mu - \sigma$, where μ is the mean

value of c_{max} obtained in the training stage, and σ is its standard deviation. The

program allows the user to change the detection threshold, should it be necessary. The

points of threshold crossing represent potential arrival times of EPSCs with two

exceptions. First, W_d ms within the onset of the laser stimulus, no synaptic responses

are expected to be found (see below), and our method dismisses any potential events

`

within this window. The default value for W_d is 10 ms. Second, W_o ms (W_o= 30 ms by default) within the laser stimulus, convolution traces may still be affected by the direct response, yielding extremely large values. Therefore, the convolution traces within this window are compared to an additional (outlier) threshold, e.g. chosen as $\mu + 4\sigma$, where μ and σ are defined as above, and potential EPSCs whose convolution traces exceed this threshold are dismissed. For each convolution trace, the samples that exceed the detection threshold form the so-called suprathreshold time segments. Within each eligible suprathreshold segment outside of W_d time window, the center of mass of each convolution trace is found and declared as an occurrence time candidate, t_{cm}, of an EPSC.

To localize EPSCs, the occurrence time candidates are processed from earlier to later along the original data trace in the following manner. First, for each potential EPSC, its negative peak is found in the vicinity of the occurrence time candidate, t_{cm}, defined a $[t_{cm} - L, t_{cm} + T]$,   where L (e.g., 4.4 ms) and T (10.2 ms) are the mean leading and trailing parts of EPSCs estimated from the training stage.   If multiple negative peaks are found around an occurrence time, they are scored according to several criteria, and the peak with the highest score is selected. The location of the peak, t_p, is then taken as the estimated EPSC occurrence time. Its onset and offset times are further identified within the segment$[t_p - L_{on}, t_p + L_{off}]$.   Here $L_{on} = \mu + \sigma$ where μ and σ are the mean and standard deviation of the leading part of EPSC estimated in the training stage, and $L_{off} = \mu + \sigma$ where μ and σ are the mean and standard deviation of the trailing part of EPSC estimated in the training stage. Specifically, the onset point of this potential EPSC is found as the largest positive peak

`

on the segment $[t_p - L_{on}, t_p]$; and the offset point is located as the largest local peak within the trailing part of the EPSC waveform between t_p and $t_p + L_{off}$, or between t_p and the onset of the next potential EPSC within $[t_p, t_p + L_{off}]$. An additional measure is employed to detect potential overlapping EPSC events within $[t_p - L_{on}, t_p + L_{off}]$. The potential EPSCs are required to exceed an amplitude threshold based upon the mean amplitude of spontaneous EPSCs assessed in the training stage. All the above procedures are repeated to process all occurrence time candidates to detect and localize potential EPSCs. Short segments of detected events centered at t_p are then extracted and saved for further analysis. EPSC parameters, such as the peak amplitude (defined as the difference between the amplitudes at t_p and the onset), the summed input ($2 \sum_{onset}^{t_p} f(x)$), and the number of detected events, are subsequently calculated and analyzed.

Modeling Neural Data

Simulated neural data were used to evaluate the performance of our method. To mimic experimental conditions, 10 EPSCs from actual whole-cell recording experiments were detected by a human operator, normalized to the amplitude of the largest EPSC ($||S_i||_\infty = 105.2$ pA; $i = 1,2,\cdots,10$) [The L$_\infty$ norm of a vector of a vector $x = [x_1, x_2, .., x_n]$ is defined as: $||x||_\infty = \max_{1 \le i \le n}|x_i|$.] and stored in a test template library. The rationale for this normalization will be explained below. For each trial, a Poisson process with the mean rate of 20 events per second and a refractory period of 27 ms was used to generate a sequence of EPSC arrival times. To account for overlapping events, in 20% of cases the refractory period was ignored. With a maximum duration of these test templates being ~20 ms, this Poisson event generator produced overlapping events with

reasonable intervals, as seen in real experimental recordings. The duration of each trial

was set to 215 ms, with an average of 4.28 EPSCs to be generated. For each trial, the

test templates were drawn at random from the library (with a uniform distribution) and

centered at the arrival times generated by the Poisson process above to form a train of

test templates.

Figure 3.6

A

EPSC rise time

laser onset

EPSC latency / arrival time

EPSC summed input
= 2 x the shaded integral

EPSC peak amplitude

25 pA

25 ms
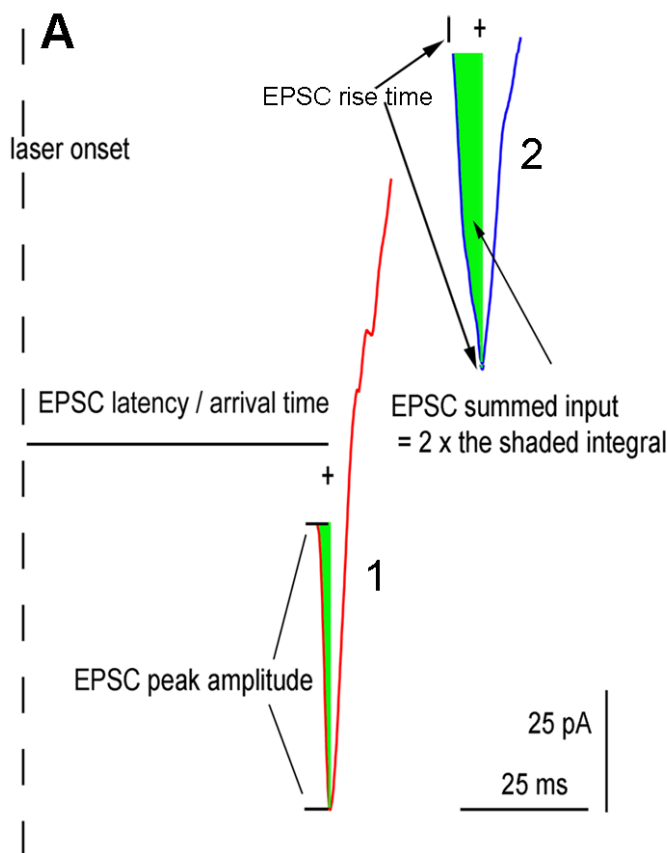
Figure 3.6. EPSC analysis and photostimulation data map construction. A shows
the two extracted EPSCs (1, 2), one showing an example of over-riding EPSCs on the
direct response, and the other showing an EPSC without being affected by the direct
response.   As illustrated in the two examples, individual EPSC peak amplitudes and
summed input amplitudes, the EPSC rise time (from the onset to the peak time), EPSC
latency/arrival time, and the number of EPSCs per site are measured. As the trailing
portion of the over-riding EPSC can be skewed by the direct response, the individual

EPSC summed input is defined as 2x [the integral area between the leading edge and the EPSC center] (the green shaded area)

To model the noise, some 160 whole-cell recordings that did not yield any evoked response (as established by the visual inspection by a human operator) were identified, normalized (mean: 0, standard deviation: 1) and saved in a noise template library. The duration of these traces was 400 ms. Note that these traces contain spontaneous activity, which presents realistic challenges to our detection method by creating potential false alarms. Other advantages of this noise model over traditionally used autoregressive models that rely on spectrum fitting are discussed at length in previous studies (Nenadic and Burdick, 2005, 2006; Benitez and Nenadic, 2008). For each trial with a given SNR, defined here as SNR $= ||S_i||_\infty/\sigma_n$, where σ_n is the desired noise standard deviation, a 215-ms-long noise segment was selected randomly from the noise library, scaled to the desired SNR (i.e. multiplied by $||S_i||_\infty/$SNR) and added to the train of test templates. The normalization of test templates admits description of each trial with a single SNR, for otherwise SNRs need to be averaged over multiple events. Note that the average SNR is not a perfect measure of noisiness of the data as two trials with the same SNR may pose vastly different challenges to the detection algorithm (Nenadic and Burdick, 2005). Note that despite the normalization of the test templates, the detection of EPSCs with variable amplitudes can be effectively simulated by varying SNRs.

For analysis of the model data, 200 Monte Carlo trials were generated for each SNR, the threshold was varied, and the detection technique with established matched filters was applied. The results are shown as receiver operating characteristic (ROC)

curves, illustrating the probability of correct detection (Pcd) and the probability of false

alarm (Pfa). The detection of EPSC test template was declared correct if the absolute

value of the difference between estimated and true arrival times was ≤ 1.5 ms. Note

that this tolerance is significantly smaller than the average duration of test template

EPSCs (~11 ms). If no EPSC was detected within 1.5 ms of the true arrival time, an

omission was declared. Similarly, if no true arrival time is found within 1.5 ms of the

estimated arrival time, a false alarm was declared. To calculate Pcd and Pfa, instances

of correct detections and false alarms are counted on a trial-by-trial basis, and averaged

over trials. Please see (Nenadic and Burdick, 2005) for the details of our averaging

methodology.

Figure 3.7
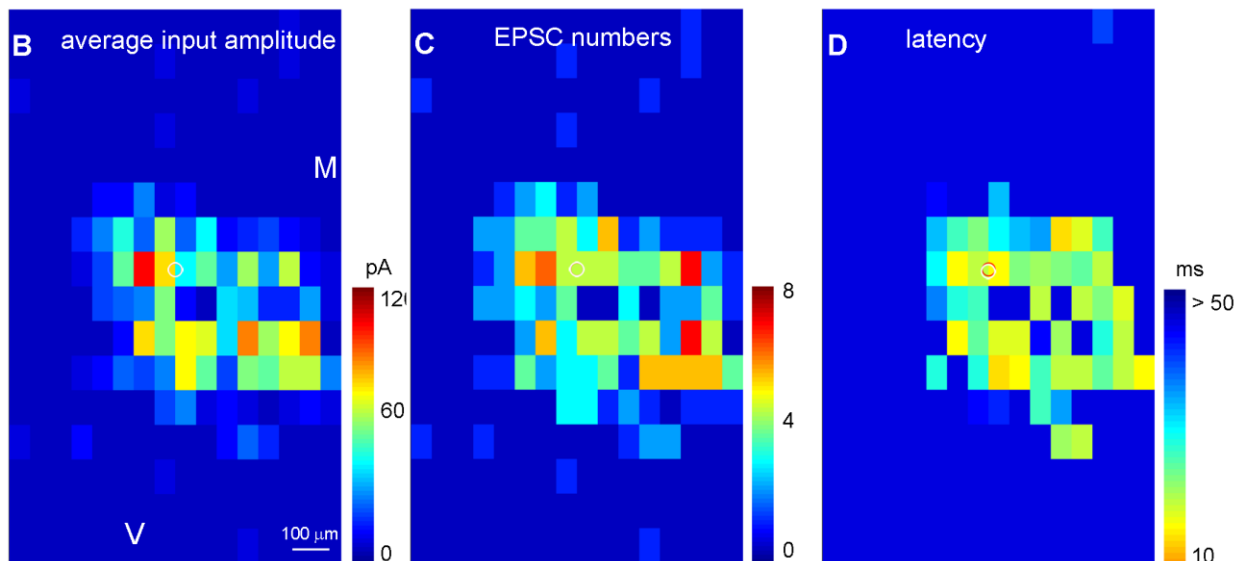
Figure 3.7. The color-coded maps (16 x16 sites) of average input amplitude, the EPSC numbers, and the first detected EPSC latency per site, respectively, for the data set shown in Figure 3.1. The average input amplitude from each stimulation site is the mean amplitude of EPSCs in the response analysis window, with the baseline spontaneous response subtracted from the photostimulation response of the same site. The calculation is based upon the measurement of the total sum of individual EPSCs from each photostimulation site for the specified analysis window, and the value is

`

expressed as pico amperes (pA). The number of EPSCs and the arrival time or latency of the first detected EPSC per site are also measured and plotted. M: medial; V: ventral.

Software programming

All programming and data processing was done in MATLAB 2008 running on a Windows 7 PC laptop computer, with a 2.4 GHz Core 2 Duo processor and 4 GB of RAM. Once the matched filters are established, the automated detection and measurements of EPSCs in one typical data set containing 256 data traces (1 second length, sampled at 10 kHz) only requires a minute or so. A basic tutorial and software implementation of our technique will be publicly available at the authors' webpage.

Results

Detection of photostimulation-evoked synaptic events through matched filtering

Overall, photostimulation-evoked EPSCs represent a range of complex synaptic events that may be encountered in other studies of synaptic connections using focal electrical stimulation and dual or multiple intracellular recordings in highly localized circuits formed by neurons of high connection probabilities (Liao et al., 1992; Gibson et al., 1999; Silberberg and Markram, 2007). As illustrated in Figure 3.1, photostimulation can induce two major forms of excitatory responses: (1) direct glutamate uncaging responses (direct activation of the recorded neuron's glutamate receptors); and (2) synaptically mediated responses (EPSCs) resulting from the suprathreshold activation of presynaptic excitatory neurons. Responses within the 10 ms window from laser onset were considered direct, as they had a distinct shape (longer rise time) and occurred immediately after glutamate uncaging (shorter latency) (Figure 3.1C). Synaptic currents with such short latencies are not possible because they would have to

92

`

occur before the generation of action potentials in photostimulated neurons (Dantzker and Callaway, 2000; Yoshimura et al., 2005; Xu and Callaway, 2009; Xu et al., 2010). Therefore, direct responses need to be excluded from local synaptic input analysis. However, at some locations, synaptic responses were over-riding on the relatively small direct responses and they needed to be identified and included in synaptic input analysis (Figure 3.1C). Detection and extraction of this type of synaptic events actually presents a major challenge for automatic signal detection and extraction using algorithms in previously published techniques. In addition, synaptically-mediated responses have varying amplitudes and frequencies with overlapping EPSC events.

Our new technique of matched filtering can be effectively applied to detection of photostimulation-evoked EPSCs, as exemplified in Figure 3.2. The raw data trace was first high-pass filtered with a Butterworth filter, which reduces the effect of the direct response and low frequency drifts (see the Methods). The filtered data trace is then convolved with all the matched filters from the bank, with potential EPSCs having better fitting of the templates and exhibiting larger convolution amplitudes. The examples of matched filters and their convolution traces are shown in Figure 3.2A and B. Note that the filters have different shapes or waveforms, based upon a range of EPSC templates selected from experimental datasets. For each candidate EPSC, given that multiple samples of a convolution trace from one matched filter are likely to exceed the threshold, and considering that multiple convolution traces can exceed the threshold, the centers of mass of all the suprathreshold segments in all convolution traces are calculated. The arrival time of candidate EPSCs can be found in the vicinity of the center-of- mass points (see the Methods for details).

Figure 3.8
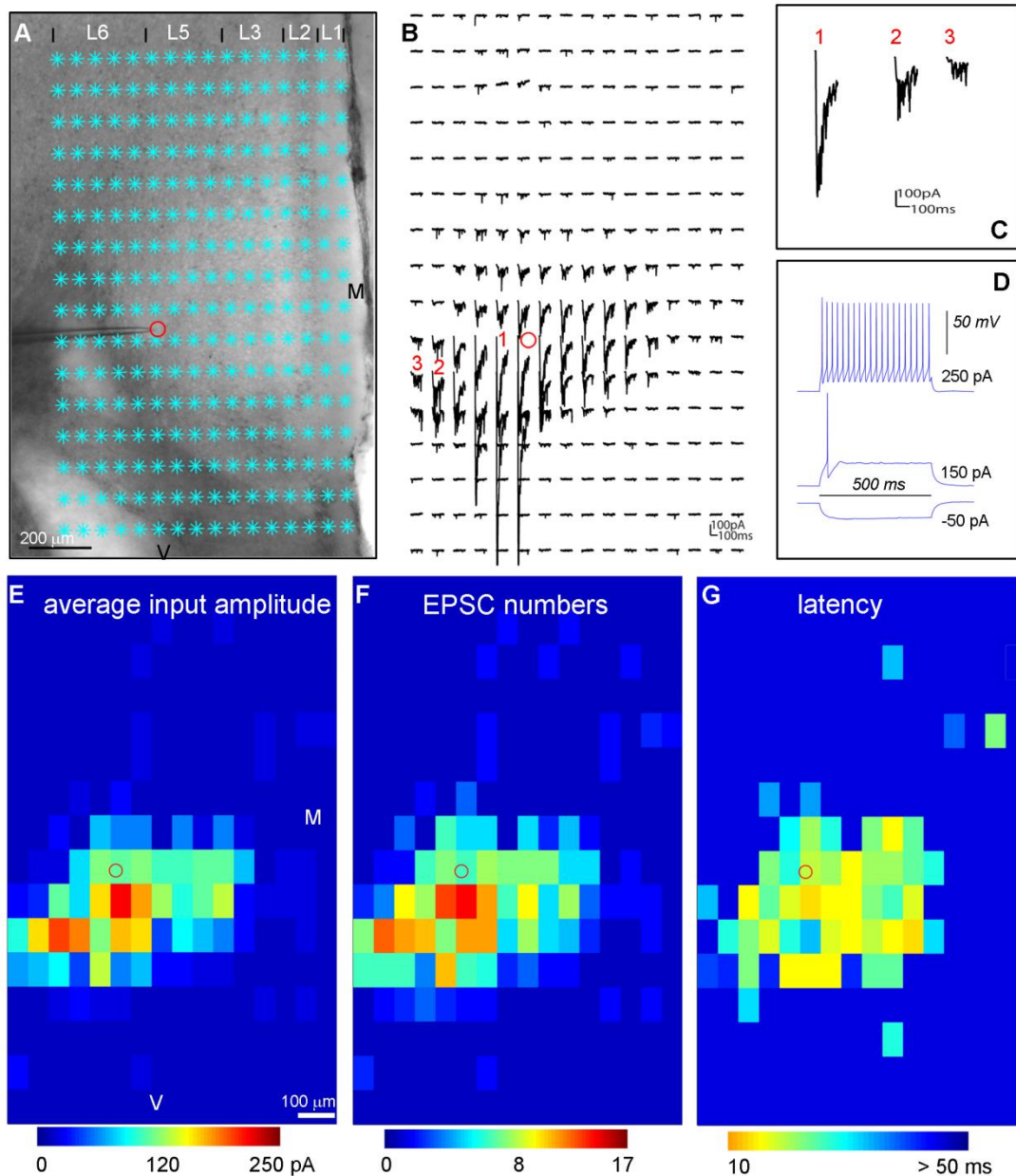
Figure 3.8. Excitatory input of local circuits to a fast-spiking (FS) inhibitory cell.
A-D are similarly formatted as in Figure 3.1. A shows a mouse prefrontal cortical slice image with the superimposed photostimulation sites (cyan stars) across all the cortical layers 1, 2, 3, 5 and 6, with a glass electrode recording from a fast spiking inhibitory interneuron in the border of layers 5 and 6 of the prelimbic area in prefrontal cortex. The red circle indicates the cell body location. M denotes medial, and V denotes ventral. B shows an array of photostimulation-evoked response traces from the locations shown in A, with the cell held at -70 mV in voltage clamp mode to detect inward excitatory synaptic input. Examples of photostimulation-evoked responses are illustrated by the traces of 1, 2 and 3, which are expanded and separately shown in C.

Trace 1 is an example of direct response with over-riding synaptic responses. Traces 2 and 3 are typical examples of synaptic input responses of FS cells. D shows the FS cell's intrinsic firing pattern with its voltage response traces to current injections at different amplitudes of -50, 150 and 250 pA, respectively. E, F and G present the color-coded maps of average input amplitude, the EPSC numbers, and the first detected EPSC latency per site, respectively, for the data set shown in B.

The EPSCs detected above need to be subjected to additional tests. To exclude direct responses, candidate EPSCs with their arrival times occurring within the direct response window (within 10 ms of the laser onset) are dismissed. While high-pass filtering reduces the direct response amplitude and duration, its convolution trace may still exhibit extremely large values (as much as 10 times greater than those of indirect synaptic responses) with long durations. With this consideration, within 30 ms of the laser onset, candidate EPSCs are declared eligible only if the convolution traces remain below the outlier threshold, but exceed the detection threshold. Detected events that fail this test are excluded from the list of candidates (Figure 3.2A). On the other hand, certain direct responses (e.g., those from the proximal or apical dendrites, see Figure 1) are relatively small, and their convolution traces may not exceed the outlier threshold. However, these direct responses can be correctly identified (Figure 3.2B), because their leading edge is traced back to the 10 ms direct response window.

The over-riding synaptic events are typically superimposed on the trailing part of the direct response (defined as the points between the (negative) peak of the direct response and the return to the baseline). While the aforementioned detection algorithm detects small, over-riding synaptic events, it also detects such responses that exhibit inflection points or "EPSC-like" notches that are related to baseline fluctuations. To eliminate these events from candidate EPSCs, an amplitude check is performed by

95

`

comparing amplitudes of candidate EPSCs to a pre-set threshold based upon the mean amplitude of spontaneous EPSCs (assessed in the training stage). Normally, the cut-off threshold is based on statistical parameters estimated during the template training procedure. However, for detection of weak EPSCs, the cutoff threshold can be empirically set based upon the spontaneous EPSC level. Candidate events that do not get excluded by the above additional criteria represent detected EPSCs.

Detection performance evaluation with simulated neural data

Since in actual recording experiments, the number of synaptic events and their exact arrival times ("ground truth") are not perfectly known, the performance of our method was first assessed on simulated data (Figure 3.3). This allowed us to systematically vary the parameters critical for detection, such as SNR and detection thresholds, and evaluate the performance in terms of the probability of correct detection (Pcd) and probability of false alarm (Pfa).

Our technique was tested under different SNR and detection threshold scenarios. To ensure statistically meaningful results, for each SNR value, 200 independent Monte Carlo trials were performed, and the technique was applied by varying the detection threshold values between $\mu - 2\sigma$ and $\mu + 3\sigma$ (in increments of 1σ), where μ and σ are the mean and standard deviation of the maximum convolution value c_{max} obtained in the training stage. Based on the detection results, Pfa and Pcd were calculated by averaging over trials, and plotted as receiver operating characteristic (ROC) curves in Fig. 3.4. In all ROC curves, false alarms and correct detection are traded off at varying threshold values. Depending on the cost associated with omission and false alarm errors, the optimal detection threshold can be set. At low SNRs, the ROC curves are

more spread for the detection thresholds chosen around the mean, μ, indicating higher sensitivity to the choice of threshold. Conversely, at SNR ≥ 9, a situation likely to be found in actual recordings, the choice of threshold is less critical, as performances tend to cluster around the optimal point (Pfa = 0, Pcd = 1).

By analyzing the estimated arrival times of the correctly detected EPSCs, we found that on average the estimated and the true arrival time differed by 0.15 ± 0.49 (mean ± SD), 0.02 ± 0.32, and 0.0 ± 0.24 ms, for SNR=3, 6, and 9, respectively, which is insignificant compared to the typical duration of the template EPSCs. Based on these results, as well as the results from the ROC curves, especially at high SNR values, we conclude that our method is expected to perform well in experimental conditions.

Analysis of experimental data, in comparison with human detection performance

Our new technique was further validated on experimental data, while compared to that of manual (human) detection. Typical examples of software detection and extraction of photostimulation-evoked EPSCs, along with human visual detection of these events, are illustrated in Fig. 3.5 A-F. These data traces include direct responses and synaptically mediated EPSCs, and contain complex overlapping events. In most occasions, EPSCs detected by the software and the human operator matched quite well, with software detection performing better than the human in identification of overlapping synaptic events (see the arrow heads in Figure 3.5). It should be noted that some of the weak EPSCs (with the amplitudes of about the spontaneous EPSC level) identified by the human, however, were missed by the automated detection, because of the pre-set cutoff threshold for evoked EPSC amplitudes. The inclusion of the amplitude cut-off setting is necessary for rejecting noise-related artifacts, due to an

97

`

inherent trade-off between the sensitivity and specificity of our and any other statistical

detection method (Kay, 1998). Those missed weak EPSCs were proportionally

insignificant, as they accounted for less than 4 % of all the candidate events across

individual datasets. In addition, considering that the software detects both the

spontaneous baseline synaptic activity and photostimulation responses, and as the

baseline spontaneous response is subtracted from the photostimulation response, the

missed measurement of weak EPSCs at the spontaneous level does not have a major

impact on our final measurement and analysis of EPSCs across many photostimulation

sites (data not shown). Figure 3.5G summarizes quantitative evaluations of the

automated detection of EPSCs, using the same filter bank at multiple detection

thresholds.   In general, the method performance was excellent and stable across

different data sets. With the detection results inspected and verified by experienced

human operators, the average probability of correct detection (Pcd) is 87.7%, with the

average false alarm (Pfa) rate of 2.6% for the three detection thresholds chosen as $\mu -$

$\sigma, \mu - 1.25\sigma$ and $\mu - 1.5\sigma$. Specifically, the probability of correct detection is 76.7% ±

2.4% (mean ± SE), 91.45% ± 3.1%, and 94.9% ± 2.43% respectively; the corresponding

probability of false alarm is 0.67 % ± 0.37%, 2.72% ± 0.44%, and 4.43% ± 1.75%,

respectively. In practical settings, our software implementation includes quick tests of

selected data traces to determine appropriate detection thresholds.

In addition, the accuracy of this technique did not seem to depend much on the

training stage and the choice of EPSCs for the design of the filter bank. To test the

robustness of the method with the template design variability, a human operator

repeated the filter design process by selecting a different set of EPSCs and

consequently obtaining a different set of templates. When this template set was used for

automated detection of EPSCs across the same data used for Figure 3.5G, the overall

rates of correct detection and false alarm were 91.7% and 7.3%, respectively, similar to

the rates reported with the first template set. Stable results were also obtained from a

template set from a different operator, as the overall rates of correct detection and false

alarm for the same dataset were 88.6% and 5.2%, respectively.

After correct detection and extraction of the events, EPSCs are subsequently

analyzed and the parameters such as EPSC peak amplitudes and summed input

amplitudes, EPSC rise times, EPSC latency/arrival times, and the number of EPSCs

from each photostimulation site are measured (Figure 3.6 A). As the trailing portion of

the over-riding EPSC is often skewed by the direct response, the individual EPSC

summed input is defined as 2 x [the integral over the segment between the leading

edge and the EPSC center]. For the purpose of visual display, a color-coded map is

constructed to illustrate the pattern of excitatory input to the recorded neuron (Figure

3.7B). The number of EPSCs and the arrival time or latency of the first detected EPSC

per site are also measured and plotted (Figure 3.7C and D).

Our automated procedure was much faster and more efficient than human

detection. It is estimated that detection and analysis of photostimulation-evoked EPSCs

with the software implementing our novel detection method are at least an order of

magnitude faster than the human manual detection and analysis. Thus, this new

technical advancement can greatly facilitate data analysis for photostimulation and other

similar experiments.

Characterization of photostimulation-evoked EPSCs

Figure 3.9

A   Original IPSC response traces

B   Inverted IPSC response traces

300pA
100ms

C

matched filters

outlier threshold

D

100 pA
10 ms

detection threshold

E   Average input amplitude

400pA

0

F   IPSC numbers

5

0

G   Latency

>50 ms

200 μm

10 ms

100
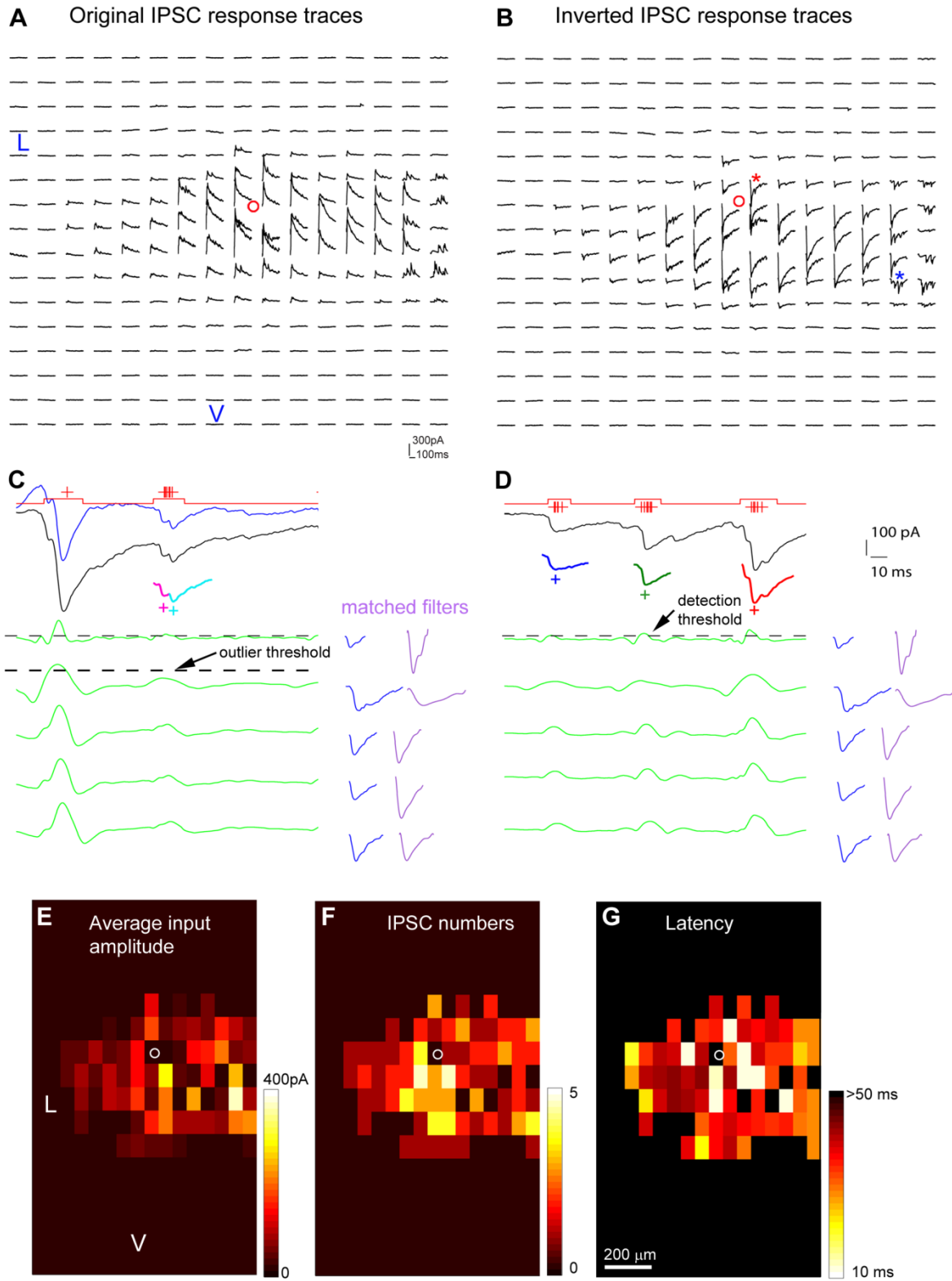
Figure 3.9. Extension of the method to the detection of IPSCs with matched filters. A and B are the original and sign-inverted IPSC response traces, respectively, which were from a layer 5 pyramidal neuron in the prelimbic area of mouse prefrontal cortex. The small red circles in A and B indicate the location of the recorded cell body. C and D are the illustration of matched-filtering detection of inverted IPSCs, reminiscent of EPSC detection (See Figure 2). The data traces for C and D are from the map sites indicated by the red and blue stars in B, respectively. The black traces are raw signals and the blue one shown in C is a high-pass filtered signal trace. In C and D, five exemplary convolution traces (green) produced with five matched filters (purple) are shown. The original EPSC templates (blue) used to synthesize the matched filters are also shown next to the convolution traces. The data trace in C has one large direct response, superimposed with two IPSCs that are color coded and individually extracted (shown below the original trace with the crosses indicating the event peaks), while the data trace in D contains three IPSC events (color coded and individually extracted, shown below the original trace). See Figure 2 for other conventions. E, F and G are the color-coded maps of average input amplitude, the IPSC numbers, and the first detected IPSC latency per site, respectively, for the raw data map shown in A. The small white circles indicate the location of the recorded cell body. L: lateral; V: ventral. The average input amplitude in each stimulation site is the mean amplitude of IPSCs in the response analysis window, with the baseline spontaneous response subtracted from the photostimulation response of the same site. The number of IPSCs and the arrival time or latency of the first detected IPSC per site are also measured and plotted.

Given that EPSCs recorded from different cell types may differ in their strength and kinetics in mouse sensory cortex (Xu and Callaway, 2009), in this study we further quantified and compared the EPSCs obtained from excitatory pyramidal cells and fast-spiking (FS) interneurons in mouse prefrontal cortex with our new technique. As illustrated in Figure 3.8, when compared to excitatory pyramidal cells (see Fig. 3.1), FS cells tend to receive stronger and more frequent evoked EPSCs from local laminar circuits. In addition, FS cells' EPSCs may have faster kinetics, as they exhibit sharper rising phases. This qualitative impression was confirmed by our quantitative analysis of EPSCs recorded from these two cell types (Table 1). The data analysis was based upon automated detection and measurement of 689 photostimulation-evoked EPSCs recorded from excitatory pyramidal cells (N = 3), and 1076 evoked EPSCs recorded

`

from FS cells (N = 3). As seen from Table 1, excitatory pyramidal cells had weaker

EPSCs than FS cells, as established by comparing their median EPSC peak amplitudes

which were 35.66 ± 2.31 pA (mean ± SE) and 50.77 ± 2.84 pA, respectively. Compared

to excitatory pyramidal cells, the EPSCs of FS cells had on average shorter rise times,

as their respective values were 2.93 ± 0.73 ms (FS cells) and 4.7 ± 0.31 ms. Excitatory

and FS cells also differed in their average EPSC frequencies per stimulation site, as

their respective values are 4.37 ± 0.59 Hz and 7.87 ± 1.49 Hz. Finally, the latencies of

the first detected EPSC per site for excitatory pyramidal and FS cells were relatively

similar (42.4 ± 5.23 ms vs 37.9 ± 4.82 ms). Therefore, our novel technique allows

detailed quantitative data analysis and enables efficient treatment of large datasets

through dependable, automated detection and characterization of synaptic events.

Application of the method to IPSC detection

Given the general applicability of our matched filter detection and extraction

algorithms, our method can be appropriately modified and further applied to detection

and extraction of other types of electrophysiological signals. For example, the

technique has been easily modified to accommodate detection and analysis of inhibitory

postsynaptic current (IPSC) responses. As illustrated in Figure 3.9A and B, for the

IPSC detection, we first inverted the sign of IPSC responses, so the outward IPSC

responses turned into EPSC-like inward responses. Note that compared to EPSCs,

inverted IPSCs tend to have different waveforms with longer response durations (see

Fig. 3.1 and 3.9). As done in EPSC detection, the bank of matched filters was then

generated based upon the inverted IPSCs and automated detection was applied for

`

IPSC map data analysis and plotting (Figure 3.9C-G). Similar to EPSC detection, our method achieved excellent performance in IPSC detection across datasets.

Discussion

In this study, we have developed a novel matched filtering technique for automated detection and extraction of synaptic events by combining the design of a bank of matched filters with the detection and estimation theory. The current technique has overcome the limitations of previously described threshold and template comparison techniques in detection of complex evoked synaptic signals with variable amplitudes and superimposed events.

An important novel feature of our technique is utilization of a bank of matched filters for the detection stage, which offers several advantages over previous techniques of template comparison. When human supervision is allowed, the optimal detector is a matched filter (template). Since humans have good understanding of the underlying signals, synaptic events can be reliably selected and their waveform appropriately modeled with high order polynomials (templates). EPSCs that match the templates are detected with high sensitivity by convolving with templates; artifacts and noise transients are rejected (filtered out) because they do not match the template waveform and time course. However, previous techniques using a template with fixed or variable amplitudes resulted in low sensitivity if the actual event waveform deviated from the template waveform; these techniques were not as effective for detecting overlapping events and compounds of events with different kinetics (Clements and Bekkers, 1997; Hwang and Copenhagen, 1999). Compared to fixed or scaled templates, even a few templates clearly increase the sensitivity of EPSC detection (Li et al., 2007). This major

`

issue of single template comparison has been avoided in our new technique, as an array of filters based upon identified EPSCs from experimental data in the training stage provides a range of templates with variable shapes and durations that potentially match a variety of EPSCs found in experimental recordings.

For the design of filters, the training stage requires prior knowledge about evoked EPSCs and requires human supervision in selecting typical events for matched filter synthesis. However, the training stage is rather quick (~10 min), and templates and parameters acquired from a typical data set can be used for detection of EPSCs in other similar experiments. In addition, the bank of multiple templates allow the statistics of the expected event waveform characteristics and time courses to be derived, and detection thresholds and safeguards against false detection to be subsequently set in a statistically meaningful manner. This constitutes one important novel of our method, as in previous studies the criteria used for both detection and extraction were mostly set empirically through error and trial (Cochran, 1993; Abdul-Ghani et al., 1996; Clements and Bekkers, 1997; Hwang and Copenhagen, 1999; Jin et al., 2006; Li et al., 2007).

Although the present study was focused on EPSC detection and extraction, considering the general-purpose nature of our matched filtering and signal recognition algorithms, we expect the technique to be applicable to detection and extraction of other electrophysiological events such as extracellular action potentials, and event-related local field and electroencephalogram potentials as well as optical imaging signals (e.g., calcium indicator signals and voltage sensitive dye signals) in general. This generalizability follows from the theoretical properties of the matched filter which is known to be the SNR-optimal signal detector (Kay, 1998). Clearly, the application of

104

`

our technique to other domains will require modifications, including the design of an appropriate filter bank and adjustment of sensitivity/specificity thresholds. These modifications, however, are rather easy to implement using our user-friendly software. For example, our technique has been further applied to the detection and analysis of IPSC responses. To facilitate IPSC detection, as EPSCs and IPSCs have different signs, our method simply inverted the polarity of the original raw data traces, and the filter design and automated detection steps were applied in the same way as done in the EPSC detection. As for the detection of extracellular action potentials, the use of single or limited waveform templates has been used in prior studies (Bankman et al., 1993), but the efficiency and sensitivity of detection can be greatly improved with the design of a bank of matched filters, as done in the present study. Moreover, similar to EPSCs or IPSCs, optical imaging signals such as calcium transient signals and fast voltage sensitive dye signals are mostly unipolar (Ohki et al., 2005; Xu et al., 2010) and have varying amplitudes and overlapping events. Therefore, as illustrated in the IPSC detection, the adoption of our new method to detection of optical signal events should be relatively simple. Finally, we hypothesize that our technique can be modified to accommodate detection of event-related local field and electroencephalogram potentials. Similar to extracellular action potentials, these usually have biphasic (bipolar) waveforms, and while modification procedures are likely to be different from those used in IPSC detection, the general algorithms can still be applied.

Another innovation of our technique is that convolution traces of the matched filters are compared to an event detection threshold to construct suprathreshold segments of the data trace, and the center of mass of each of the convolution trace is

`

found and declared as an occurrence time candidate of an EPSC. Single or multiple

overlapping EPSCs within each suprathreshold segment can be correctly identified (see

Fig. 3.5). Our algorithm manages to detect multiple or pairs of events that are

separated in time by less than the length of the templates, which previous template

comparison techniques would not be able to (e.g., see Clements and Bekk, 1997).

Moreover, with additional constraints of the direct response and outlier windows, our

technique is able to exclude direct photostimulation responses and detect synaptically

mediated EPSCs over-riding on the direct response. Detection and extraction of this

type of over-riding events illustrates the power and effectiveness of our new technique,

as previously published techniques would fail in such complex situations (Liao et al.,

1992; Abdul-Ghani et al., 1996; Clements and Bekkers, 1997; Hwang and Copenhagen,

1999; Li et al., 2007).

Our results show that the new method can identify events with high sensitivity

and a low false alarm rate, with tests on both simulated data and experimental data. In

most occasions, the automated detection was at least as good as human visual event

detection when applied to photostimulation experimental data. Our algorithm, in

essence, only requires the user to select a set of typical synaptic responses from

experimental data during the filter design/training stage in order to detect events, and

obtain accurate estimates of the amplitude, timing and kinetic information of the

detected events during the automated detection stage. In addition, if the default

template library and threshold settings are used, the method can be implemented in a

fully automated fashion. Should the default parameters prove inadequate, the efficient

`

software implementation and fast execution of our method allow the parameter

adjustment under training-derived statistical guidance.

With the established filter bank, the sensitivity and specificity of our technique is

dependent on two parameters, the event detection threshold, and the event amplitude

cut-off threshold. The statistics of the filter bank (e.g., the mean and standard

deviations of convolution peak values) may help guide the setting of appropriate

detection thresholds. In addition, the software implementation allows practical tests of

selected data traces to determine optimal detection thresholds.   As shown in our ROC

analysis, the lower detection thresholds may present higher sensitivity in detection but

with a higher false alarm rate. Sometimes when it is necessary to set a lower detection

threshold for detecting low-amplitude events, the event amplitude cut-off threshold is

important to reject noise-related artifacts, and ensures a low rate of false alarm.

In summary, our algorithms and software implementation enable dependable

automatic detection of synaptic events with minimal human supervision. The use of a

bank of matched filters and template-derived statistical guidance are important novel

features of our technique. This work represents a substantial contribution to the

recognition and detection of complex signals encountered in the studies of synaptic

physiology.

`

Chapter 4

Large scale neural circuit mapping data analysis accelerated with the graphical processing unit (GPU)

Modern neuroscience research demands computing power. Neural circuit mapping studies such as those using laser scanning photostimulation (LSPS) produce large amounts of data and require intensive computation for post-hoc processing and analysis. Here we report on the design and implementation of a cost-effective desktop computer system for accelerated experimental data processing with recent GPU computing technology. A new version of Matlab software with GPU enabled functions is used to develop programs that run on NVidia GPUs to harness their parallel computing power. We evaluated both the central processing unit (CPU) and GPU-enabled computational performance of our system in benchmark testing and practical applications. The experimental results show that the GPU-CPU co-processing of simulated data and actual LSPS experimental data clearly outperformed the multi-core CPU with up to a 22x speedup, depending on computational tasks. Further, we present a comparison of numerical accuracy between GPU and CPU computation to verify the precision of GPU computation. In addition, we show how GPUs can be effectively adapted to improve the performance of a commercial image processing software such as Adobe Photoshop. Together, GPU enabled computation enhances our ability to process large-scale data sets derived from neural circuit mapping studies, allowing for increased processing speeds while retaining data precision.

`

Introduction

Computer-based resources can greatly facilitate neuroscience research. As neuroscientists demand more computing power for circuit mapping studies, researchers may resort to expensive solutions such as clusters and supercomputers for large-scale computational tasks. Due to recent advances in the graphics processing unit (GPU) computing technology, today's GPU does much more than rendering graphics as originally intended, and GPUs can provide an inexpensive and computationally powerful alternative to CPU based solutions (Nageswaran et al., 2009; Baladron et al., 2012).

Traditionally, a central processing unit (CPU) has been the computation core of computers. The CPU is specialized in optimizing serial operations while containing various sub-circuits for multiple types of tasks, such as coordinating concurrent software processes, predicting branches, handling high priority interrupts and managing cache-memory traffic. However, its serial processing nature limits its ability to perform intensive parallel computation. In comparison, the newest generations of GPUs have stream multiprocessors and act as powerful massively parallel coprocessors. Yet, the price paid for such power at a relatively modest cost is that GPUs are unconventional in their organization, and in particular are highly constrained in their communication bandwidth with the main CPU and in the type of operations that can efficiently be executed in parallel. It is often extremely difficult to map a given application for effective (fast) execution on GPUs. Regardless, because of their promise, scientists and engineers have returned to exploring the power of GPUs for various applications ranging from astrophysics and finance to biomedical research, enabled by the recent advances in hardware and integrated programming interfaces such as Nvidia's

`

Compute Unified Device Architecture (CUDA) platform. In a custom-designed system,

GPU-accelerated applications can split their computationally intense tasks into a

number of threads which could be further processed by thousands of cores of GPUs. In

addition, the recent addition of double-precision floating point units provides GPUs the

capability to produce accurate results that can satisfy the strictest computational

requirements.

Table 4.1. Structural components and general computation capabilities of the

CPU and GPU used in our desk computer system.

Components	Model	Price, each ($)	Note
Hard Drive	Samsung 840 Pro	218	Two units In RAID 0 mode
Motherboard	ASUS Rampage IV extreme	439	
CPU	Intel i7-3930k	499	Running at 4.5 GHz
CPU Cooler	Corsair H100i closed loop liquid cooler	105.99	
System Memory	G.SKILL 32 GB Quad Channel DDR3	300	Running at 2.133 GHz
Graphic Card	Asus GTX 680 A455-0686	520	
CUDA card	Nvidia Tesla K20c	3,500	
Case	Cooler Master HAF X RC-942-KKN1	200	
Power	Corsair AX1200i	320	
Keyboard/Mouse	Logitech MK520 Combo	41.99	
Monitor	Asus PB278Q 27"	649	
Speaker	Creative T10	40	
Operating System	Windows 8 Pro x64	149	

All the data shown in the table are provided by the published documents from the manufactures
(http://www.techpowerup.com/cpudb/858/core-i7-3930k.html;
http://www.techpowerup.com/gpudb/564/tesla-k20c.html). The price info is as of June 30th, 2013.

In the field of neuroscience, GPU computing has been successfully used for

computer-intensive tasks, including large-scale modeling and simulation of neural

`

network, high-speed imaging and real-time reconstructions (Nageswaran et al., 2009; Wilson, 2011a; Wilson, 2011b; Yang et al., 2011a, b; Baladron et al., 2012; Tomer et al., 2012; Fang and Lee, 2013). However, to our best knowledge, no or few studies have tapped into the GPU computation for neural circuit mapping data analysis while large scale neural circuit mapping experiments in vitro (Shepherd et al., 2005; Xu et al., 2010; Franke et al., 2012; Kuhlman et al., 2013a) and in vivo (Ohki et al., 2005; Nauhaus et al., 2008; Nauhaus et al., 2009) produce large amounts of data in short times that require tremendous computation power for post-hoc processing and analysis. The ability to take advantage of GPU-enabled computation in a desktop computer system presents a sufficient and cost-effective solution to individual neuroscience research laboratories that have no access to or cannot afford the access to high-performance computing centers. To promote a wider application of GPUs in neuroscience research, in this paper, we first introduce how to assemble a GPU-enabled desktop computer system with detailed hardware and software information. We then compare CPU and GPU-enabled computational performance of our system in benchmark testing and practical applications. We specifically present an approach of using GPUs in Matlab to achieve accelerated processing of large amounts of neural circuit mapping data. Finally, we present an analysis of numerical accuracy between GPU and CPU computation to verify the precision of GPU computation.

Materials and Methods

In this section, we describe the configuration and assembly of a GPU-enabled desktop computer system. We also describe our data acquisition and relevant analysis,

111

`

and detail on the algorithms used to optimize the data organization, exploit the memory hierarchy and integrate GPU computation.

System Components

Our system consists of an Intel i7-3930K CPU and an NVidia Tesla K20c GPU (Fig 4.1). The CPU has 6 physical cores which share a 12MB L3 cache. It communicates with 32 GB system memory at a bandwidth of 49.64 GB/sec. Note that the CPU memory bandwidth varies at different memory clocks. The GPU has 2496 physical cores that are clustered in 13 Stream Multiprocessors (SMX), which share a 1.5MB L2 cache and communicate with a 5 GB graphic memory with 208 GB/sec bandwidth. The system memory and GPU are connected through a PCI-E 2.0 x16 bus with a transfer speed of 8 GB/s each way. Please see Table 4.2A for detailed comparison of specifications.

For such a custom built desktop computer system, we have selected components (see Table 4.1) to maximize the performance while keeping the cost within a reasonable range. The CPU is from Intel's high performance product line. We have carefully over-clocked it and the CPU performance increased by 25-29% as tested using GPUBench (see below). The RAM used is also a high-clocked version from a reputable manufacturer to match the over-clocked CPU. The whole system is cooled by 7 fans with the CPU cooled by a closed-loop liquid cooler. Such intense cooling is necessary since overheating can trigger the protection mechanism in the CPU, resulting in reduced performance, less accurate computation and even chip degradation. The motherboard should support two graphic cards running concurrently at PCIE x16 2.0. A full size tower case is required to fit all the components including the heavy-duty cooling

`

and ventilation system. The whole computer system needs to prove stable by running

intensive computation tasks for 48 hours and the maximum recorded CPU core

temperature needs to be below 75 °C, recommended by the Intel documentation. The

final cost of the entire system (as per Table 4.1) was around $7500, and the Tesla K20c

GPU, although donated by NVidia, had a market value of $3500 by the time the system

was assembled.

Figure 4.1
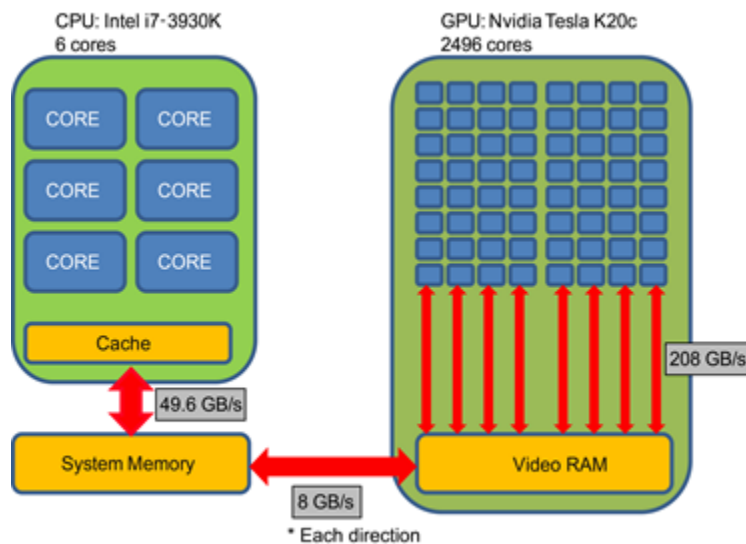
Figure 4.1. Architectural structures of the central processing unit (CPU) and the graphic processing unit (GPU) in our custom-made desktop computer system.
We use the CPU of Intel i7-3930K (6 cores) and the GPU of NVidia Tesla K20c (2496 cores). The double arrows indicate memory transfer for computation. The transfer speeds between the cache and the system memory (i.e., RAM), between GPU cores and the video RAM (VRAM), and between the VRAM and the system memory are 49.64 GB/sec, 208GB/sec and 8 GB/sec, respectively.

System Assembly

`

      The general computer assembly has been described in many existing guides (e.g., http://www.gskill.us/forum/showthread.php?t=10512). It is a good practice to assemble basic components on the bench and have them individually tested outside of the tower case.   After the initial test, we can now fit every component into the case. Although the layout of the components is fixed with the specified tower case and motherboard, it is important to route connection cables between components in a tangle-free manner. It is equally important to determine the location of the CPU liquid cooler radiator and air flow directions. Ambient cool air needs to be drawn by the fan from the case bottom, and should be heated up as it travels through the hard drives, GPUs, the CPU radiator and RAMs. The cooling fans placed at the top and rear of the tower case draws the heated air out of the case. Dust filters at the front of the incoming fan helps to reduce dust accumulation on internal components. After the system assembly is completed, we recommend to overclock the system to achieve performance gains. Finally, it is important to test the stability for a custom assembled system. Many tools are available for free on the internet, and the common choices include Intel Burn Test, Linx, prime95 and Memtest.

      The necessary software includes the operating system software, driver software, Matlab (Mathworks, Natick, MA) and CUDA Software Development Kit (SDK) for support of GPU computing. We use Windows 8 x64 due to its large user volume and better support for Solid-State hard drives. After Window 8 is installed, it is recommended to run the embedded system assessment test to ensure that the operating system (OS) can fully evaluate the hardware performance. Without such a test, the OS may use a default performance profile, limiting the hardware capability.

`

The drivers for the motherboard, graphic card and Tesla Card are available for download at the manufacturer's websites, and they should be specific to your component choices. We use a system monitoring software, Aida64 (http://www.aida64.com/) to keep track of the system status. It provides monitoring data of the CPU and GPU temperatures, voltages, cooling performance, and other parameters. This software has a safe-operating mechanism which alerts and puts the computer to a standby mode when any overheating is detected.

Figure 4.2
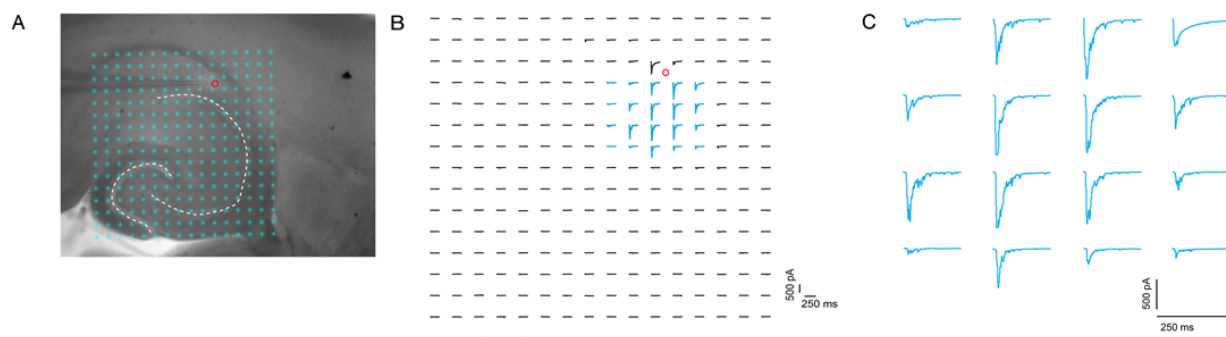
Figure 4.2. Illustration of laser scanning photostimulation (LSPS) combined with whole cell recordings to map local circuit input to a hippocampal CA1 interneuron. A shows a mouse hippocampal slice image with the superimposed photostimulation sites (16×16 cyan *, spaced at 100 µm×100 µm). The glass electrode was recording from an interneuron in the oriens lacunosum-moleculare (OLM) layer of CA1. The red circle indicates the cell body location. B shows an array of photostimulation-evoked response traces from the photostimulation locations shown in A, with the cell held at −70 mV in voltage clamp mode to detect inward excitatory synaptic currents (EPSCs). Only the 250 ms of the recorded traces after the onset of laser photostimulation (1 ms, 20 mW) are shown. C shows the enlarged and expanded traces from the highlighted traces in B. This type of experimentation generates large amounts of data, and requires intensive computation for post-hoc data analysis.

`

We use Matlab software (version r2013b) as a GPU computing platform as the software is commonly used in neuroscience research and the new version contains the latest Parallel Computing Toolbox with many GPU enabled functions. In order for Matlab to have access to the Tesla card, CUDA driver from NVidia website (https://developer.nvidia.com/cuda-downloads) has been downloaded and installed. A simple benchmark using GPUBench (provided by the Parallel Computing Team of Matlab) is performed to ensure every hardware component is running without any unexpected throttling.

GPU computation for accelerated processing of experimental data

Different from most previous neuroscience applications in neuronal network modeling and simulation, this custom system is intended for using GPU-parallel computation in actual experimental data analysis that requires intensive computation. We have developed and applied photostimulation-based mapping techniques for local cortical circuit connectivity analysis. Particularly, laser scanning photostimulation (LSPS) combined with whole cell recording in living brain slice preparations allows high resolution mapping of regional distributions of presynaptic input sources to single neurons (Fig 4.2). Because the simultaneous recording from a postsynaptic neuron with photostimulation of clusters of presynaptic neurons at many different locations, the LSPS methodology provides quantitative measures of spatial distribution of excitatory or inhibitory inputs.

The experimental procedure and the design of our laser scanning photostimulation system has been described previously (Shi et al., 2010; Xu et al., 2010; Kuhlman et al., 2013b). A laser unit (model 3501, DPSS Lasers, Santa Clara,

116

`

CA) was used to generate a 355 nm UV laser for glutamate uncaging. Once stable whole cell recordings were achieved with good access resistance (usually <20 MΩ), the microscope objective was switched from 60× to 4× for laser scanning photostimulation. At low magnification (4× objective lens, 0.16 NA; UplanApo, Olympus), the slice images were acquired by a high-resolution digital CCD camera (Retiga 2000, Q-imaging, Austin, TX) and used for guiding and registering photostimulation sites in cortical slices. For each recorded neuron, we usually map photostimulation-evoked inputs from a grid of 1 mm x 1mm with 16 x 16 stimulation sites (Fig.4. 2). Various laser stimulation positions were achieved through galvanometer-driven X-Y scanning mirrors (Cambridge Technology, Cambridge, MA), as the mirrors and the back aperture of the objective were in conjugate planes, thereby translating mirror positions into different scanning locations at the objective lens focal plane. During mapping experiments, photostimulation was applied to the 16×16 patterned sites (centered at the recorded neuron) in a nonraster, nonrandom sequence, while whole-cell voltage-clamp recordings were made from the recorded postsynaptic neurons with EPSCs and IPSCs measured at the holding potential of −70 mV and 0 mV, respectively, across photostimulation sites. Data were acquired with a Multiclamp 700B amplifier (Molecular Devices, Sunnyvale, CA), data acquisition boards (models PCI MIO 16E-4 and 6713, National Instruments, Austin, TX), and custom-modified version of Ephus software (Ephus, available at https://www.ephus.org/). Data were digitized at 10 kHz, and stored on a computer. Electrophysiological signals were recorded for 1000 ms in length for each stimulation. Each map dataset of 256 traces is about 20.48 MB in size. Although the example data size is not large, it served a demonstration purpose.

`

      As for the analysis of photostimulation map data, a new technique that combines the design of a bank of approximate matched filters with the detection and estimation theory was implemented for automated detection and extraction of photostimulation-evoked EPSCs or IPSCs (Shi et al., 2010).   Specifically, the Matlab program, "synaptic_event_detection", uses a bank of existing matched templates to detect synaptic event in the signal traces. During the detection stage with the CPU computation, the data trace under investigation is first high-pass filtered (>10 Hz) with a 5th order, infinite impulse response Butterworth filter. The role of this filter is to minimize the effect of the direct uncaging response, whose duration is much longer than that of synaptically mediated indirect responses. To minimize the phase distortions, this filter is implemented as a zero-phase forward and reverse digital filter. The high-pass filtered signal is then convolved with all the filters from the bank, with potential EPSCs or IPSCs providing a better fit to the templates and thus exhibiting larger convolution amplitudes. The convolution traces (one for each filter) are time-shifted to minimize the difference between the time of the convolution peak and a potential EPSC/IPS peak, and thus facilitate a more precise estimation of event occurrence times. Time-shifted convolution traces are then compared to detection thresholds. For each convolution trace, the samples that exceed the detection threshold form the so-called suprathreshold time segments. Within each eligible suprathreshold segment, a synaptic event was extracted and the center of mass of each convolution trace is found and declared as an occurrence time candidate of an EPSC/IPSC. For more technical information, please refer to Shi et al. (2010). Of the above processing steps, the convolution of matched

`

filters with high-passed signal traces requires the most intensive computation, which we have targeted for GPU implementation.

Figure 4.3
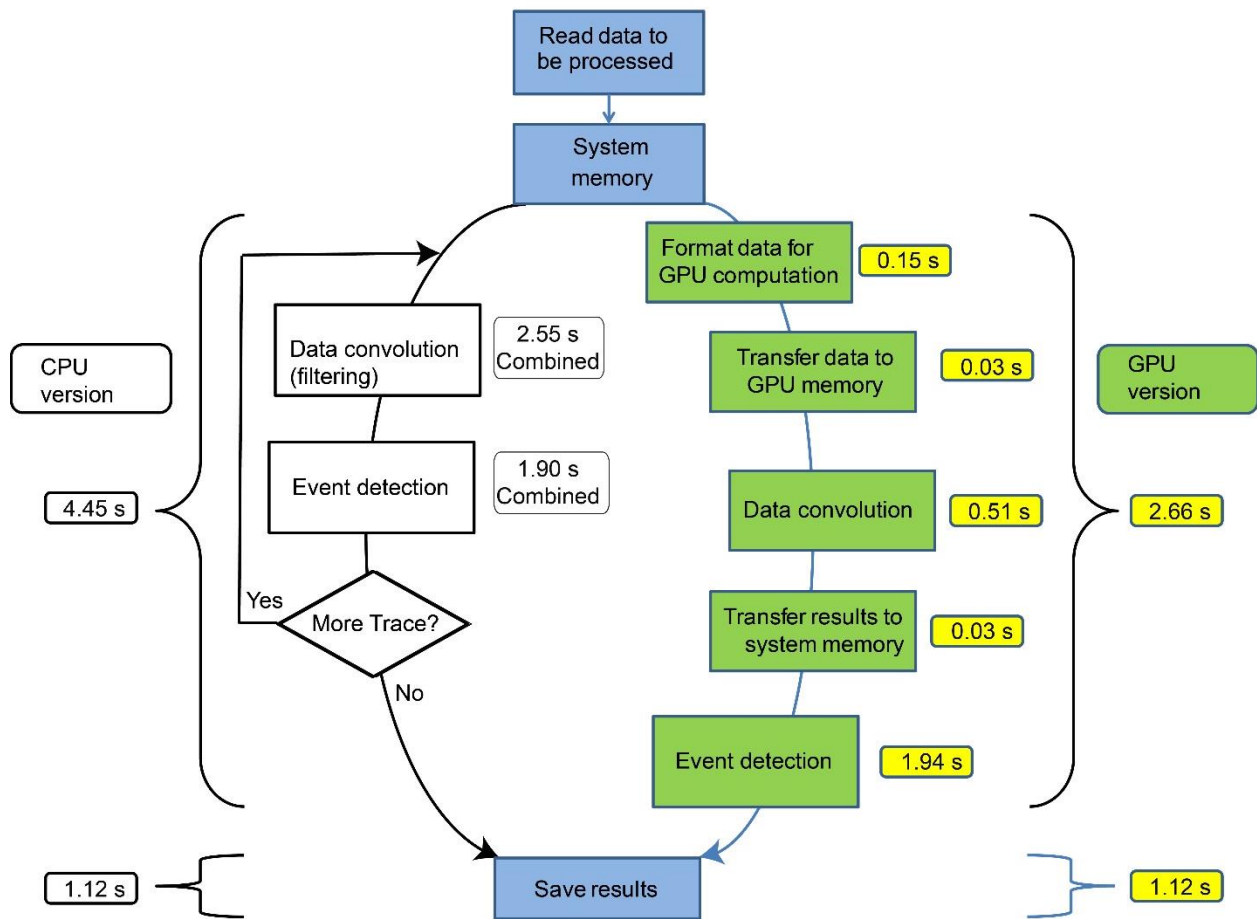
Figure 4.3. Example data processing flowchart for CPU and GPU computation. The data used here are from a typical LSPS map data set (shown in Figure 4.2B) with 256 signal traces (each containing 10000 sample points). The two versions share the steps of 'Read Raw electrophysiology trace', 'System Memory' and 'Save results'. They differ in major computation processes, with the left branch for CPU processing and the right branch for GPU processing. The computation that takes place in the GPU is coded by the green color. The processing time of each step is noted in yellow. For CPU computation in a FOR loop, the processing time for each iteration is summed up to get the combined time. The total processing times of CPU and GPU branches are marked outside of the brackets.

`

GPU-oriented Programming Considerations

The CPU and GPU architectures are illustrated in Fig.4.1. The stream processors of a GPU can only access the data that are stored in its video memory, cache or shared memory. The video memory (VRAM) is large enough (5 GB on the K20c GPU) to store the data and results relevant to the computation. To use a GPU for computation, the data needs to be explicitly transferred to VRAM from the system memory (RAM) through the PCIE 2.0 bus. The transfer rate of PCIE 2.0 is 8.0GB/s for each direction, which is much lower compared with the GPU-VRAM or CPU-RAM speed (Fig.4.1). There is also an initiation latency of data transfer, with the average measured latency being 0.3 ms. To maximize the GPU performance, it is critical to reduce the number of data transfers between RAM and VRAM.

We modified the "synaptic_event_detection" program in light of the above consideration of effective GPU computation (Fig 4.3). All the high-passed signal traces from each map data set are concatenated as one large vector and transferred to VRAM altogether. The same operation is done for the matched filters, which are originally stored in a Matlab cell array. An auxiliary vector is created to store the lengths of matched filters, and help index individual matched filters in the filter vector. In GPU-enabled computation, the large vector of signal traces is convolved with each matched filter and the resultant trace is then transferred back to RAM for event detection and extraction. The code for such GPU-tailored modifications is shown in Appendix 2. A complete CPU code of the "synaptic_event_detection" program is described in our previous publication (Shi et al., 2010) and available at our website: http://xulab.anat.uci.edu/synapticeventdetection/index.htm).
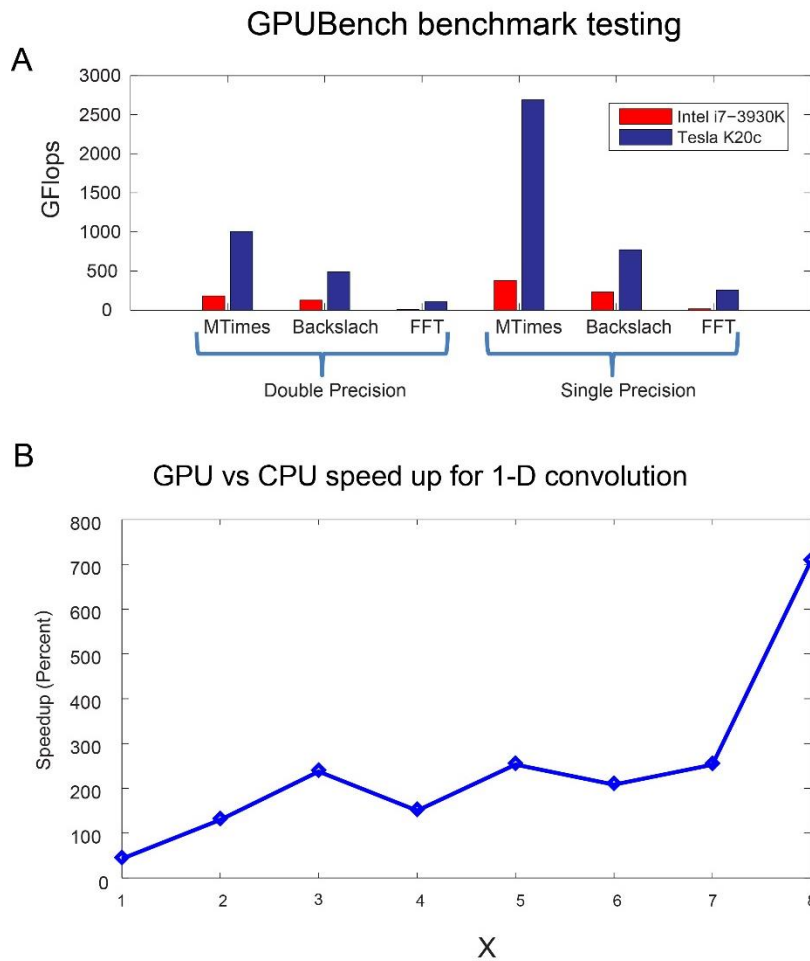
Figure 4.4

Figure 4.4. Basic comparisons of CPU versus GPU performance. A. Benchmark testing comparison of the CPU and GPU processing capabilities, assessed by their performance (GFlops) in three widely used computation, MTimes, Backslash and FFT, in the software platform of Matlab. B. GPU versus CPU speed up of 1-D convolution. Vectors of different lengths were generated by using the Matlab function, *rand()*. The vector length = 2^X * 10000 (X $\in$ [1, 2, ... 8]). The x-axis represents the value of X. The filter vector with its length of 20000 points was generated by the *rand()* function as well. The y-axis is the speed up of GPU convolution versus CPU convolution on the same vector and filter pair. The time of GPU convolution included the time of transferring data to and back from the GPU memory.

Figure 4.5
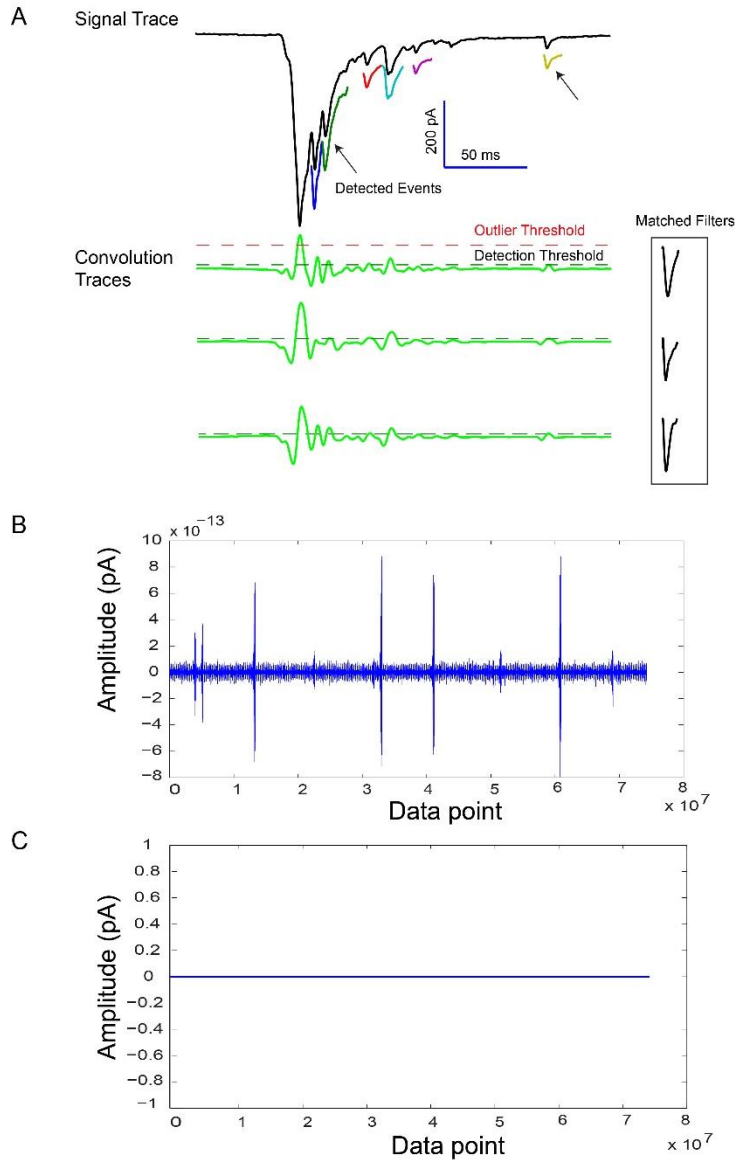
Figure 4.5. Data convolution accuracy via GPU computing. A. Example data trace convolution. The top portion shows the actual signal trace with 6 EPSC events (color-coded) identified and extracted shown below. Note the first, large peak is determined to be a direct uncaging response. The bottom portion shows three convolved traces of the signal trace to the 3 example matched filters shown by the right side, with potential EPSCs having better fitting of the templates and exhibiting larger convolution amplitudes. For the subsequent event detection, the convolution traces are compared

to a detection threshold and an outlier threshold (see the Method). **B-C.** The difference of CPU versus GPU convolution of the same data trace. The convolution trace is based on concatenated convolved traces (i.e., the results of 256 individual traces with 29 matched filters). Each signal trace contains 10000 sample points. The lengths of matched filters range from 651 to 3194 data points. The x-axis represents data points while the y-axis shows the difference in convolution amplitude in the unit of pA. In B the y-axis scale is set to [-8, 10] $*10^{-13}$, while the scale in C is set to [-1, 1].

Results

CPU versus GPU Performance Benchmarking in Matlab

To compare the potential speedup of using GPUs, we first examined the performance of CPU versus GPU-enabled computation using 'GPUBench' in Matlab. Basic scientific computations were performed through different GPUBench tests including MTimes, Backslash and fast Fourier transform (FFT). MTimes involves the multiplication of two matrices, A and B, whereas Backslash involves the matrix "division", A/B. The Backslash operation essentially finds the solution of a system A*X=B by Gaussian elimination. FFT computes the discrete Fourier transform (DFT) of a vector X. A, B and X were generated using Matlab's random number function, *rand()*. GPUBench uses the Matlab integrated timer command (*tic*, *toc*) to measure the processing time of GPU and CPU kernels. The performance of both kernels in GFlops is then calculated by dividing the number of floating point operations by the actual processing time. The processing time does not include the allocation/deallocation of RAM or VRAM, since the memory spaces are allocated at the beginning and are not reallocated during benchmarking. Also, the GPU benchmark does not include the time to transfer the data to VRAM and the computational results back to RAM.

The performance of both single and double precision floating point computation was evaluated in different tests (Fig 4.4A; Table 4.2B). Compared to CPU performance

in terms of GFlops, GPU-enabled computation achieved a speed up of 705%, 315%

and 2207%, respectively, in single precision computation of MTimes, backslash and

FFT, while their respective speed up was 577%, 388% and 1326% in double precision

computation. These dramatically increased speeds are due to powerful massively

parallel coprocessors in the GPU.

Table 4.2. System and performance comparison of CPU and GPU-enabled computing

A. The manufacturer specifications

	CORES			Memory		Processing Power(peak)(GFlops)		Power Consumption (Peak)(W)
	# of Cores	Frequency	# of Transistors	Bandwidth	Size	Single Precision	Double Precision	
CPU (Intel I7-3930k)	6	3.2GHz	2.27 Billion	Up to 51.2GB/s	Up to 64GB			130
GPU (NVidia Tesla K20c)	2496	706MHz	7.1 Billion	208 GB/s	5GB	3520	1170	225

B. CPU and GPU benchmark testing results with GPUBench

	Results for data-type 'double' (In GFLOPS)			Results for data-type 'single' (In GFLOPS)		
	MTimes	Backslash	FFT	MTimes	Backslash	FFT
CPU	174.38	126.78	7.92	375.05	245.17	11.53
Tesla K20c	1004.98	486.86	105.08	2657.88	772.11	254.95

C. 1D-convolution benchmark results

x	1	2	3	4	5	6	7	8
CPU	0.006	0.024	0.0624	0.0644	0.187	0.2834	0.6574	3.5734
Tesla K20c	0.014	0.018	0.026	0.042	0.073	0.134	0.257	0.503

Note that the speedup is also shown in Figure 4B. The benchmark data length = 2^x * 10000. The results are the running times of the convolution in seconds.

`

Convolution Speed Comparison

For LSPS map data analysis, we use the custom-made Matlab program, "synaptic_event_detection", which uses a bank of existing matched templates to detect synaptic events in signal traces. Since convolution using the Matlab function, *conv()*, is a computational core of the program for synaptic event detection, we are interested in examining the performance of CPU and GPU-enabled computation in convolving data vectors of different lengths with an 1-dimensional (1-D) template of a fixed length. As the convolution computation is not included in the GPUBench software, we implemented a simple benchmark code (see Appendix 1) that performs 1-D convolution in Matlab.   Vectors of different lengths were generated by using the Matlab *rand()* function. The lengths of data vectors are $2^X * 10000$ ($X \in [1, 2, \ldots 8]$). A second vector was generated by the Matlab *rand()* function to be used as a convolution filter with its length being 20000.   The data vectors of different lengths were convoluted with this fixed filter. Again, the time of memory allocation/deallocation is not included in actual computation time; the GPU computation time includes the necessary data transfer between RAM and VRAM. As shown in Fig 4.4B and Table 4.2C, GPU constantly outperformed CPU in convolving data with a vector length of 40000 and higher. The speed up of GPU computation tends to increase with the larger vector length.   When the data vector length is $2^8 * 10000$ (the total length of 256 traces contained in one typical LSPS map data set), the speed up is about 700%.

Acceleration of Electrophysiological Data Processing

To examine the performance gains in actual experimental data analysis, we compared the processing speed of the CPU version of the "Synaptic Event Detection"

`

program versus its GPU-enabled version (see Appendix 2 for code comparison). As

described in Methods, the GPU version of this function was modified to minimize the

number of data transfer over PCIE x16 2.0 bus. All individual traces (256 traces from

one map data set) were first concatenated to a large trace. The data of both the signal

trace and matched filters are of double precision floating point types. During the

automated event detection stage of the "Synaptic Event Detection" program, the key

step that requires intensive computation is to convolve signal traces with a bank of

matched filters (Fig 4.5A). Typically, as illustrated in Fig 4.3, the CPU completed the

convolution of 256 signal traces with each of the 29 matched filters in a total of 2.55

seconds. In comparison, the GPU completed the convolution in 0.51 seconds, which

corresponds to a speed increase of 500% for this operation. Note that the data transfer

overhead was 0.03 seconds each way and the cost for reformatting data for the GPU

computation was 0.15 seconds. Since both event detection cores are on the CPU, the

processing time is comparable at 1.90 seconds and 1.94 seconds in the CPU and GPU

versions, respectively. The GPU version takes much less time (59% of the CPU

version) for processing all 256 electrophysiological traces that are contained in one data

map. This data processing acceleration would make a huge difference in computational

times in consideration of our batch analysis of hundreds of different data maps.

Although both CPUs and GPUs are compatible with IEEE 754-2008 Floating-

Point Standard, it is important to compare the accuracy of GPU computation results to

those of CPU as the CPU and GPU use different architectures for double floating point

computation. We used CPU results as a standard and examined how much the GPU

results deviated from them. The convolution of the same signal trace using 29 different

`

matched filters was acquired from both CPU and GPU versions of the detection

program. The difference was calculated by comparing the convolution traces of using

the GPU versus the CPU program.   As shown in Fig 4.5B, the maximum difference

between CPU and GPU convolved traces is 81.5± 3.72 * 10^{-13} pA. These tiny

differences may result from different floating point rounding modes used by the CPU

and GPU (Yablonski, 2011). In practice, these numerical differences have no impact on

our data analysis. When we used the synaptic events that were detected and extracted

in both programs for quantification and visualization, there is no difference across the

data maps and they are identical (Fig 4.6). Thus, GPU enabled computation enhances

our ability of processing large data sets derived from photostimulation circuit mapping

experiments. It also allows us to increase data processing speeds while retaining data

precision.

Image Processing Application

GPUs have been used for enhancing image visualization through custom-written

programs (Eilemann et al., 2012). In this paper, we also show GPUs can be effectively

adapted to improve the performance of image processing in Adobe Photoshop. This is

major commercially available software that is widely used in academic research for

routine image edits and analysis. The Photoshop software has adopted GPU

computation since the release of the CS4 version. However, the latest version of

Photoshop CC cannot utilize the Tesla K20c card. We used its sibling GTX680 card (a

high-end consumer-grade GPU installed in our desktop system) to complete this test.

GTX680 shares the same microarchitecture of Tesla K20c but it has a lower

configuration with 1536 physical cores running at 1006MHz with 2GB VRAM and costs

`

a fraction of the price of the Tesla K20c. We examined how much the GPU could speed up general Photoshop operations on two testing images of different sizes. The images are in .tif formats with 24 bit depth for the RGB mode; image 1 has 8176 pixels x 6132 pixels with a size of 150MB, and image 2 has 16352 x 12264 with a size of 573MB. To ensure consistent benchmark results, we used a fixed series of Photoshop actions (http://cdn.pugetsystems.com/articles/PugetBench.zip) to apply blurry effects to the tested images. These actions included Field blur, Iris blur and Tilt-Shift effect. We found that GPU-enabled computation achieved 165% speedup (16 sec versus 26 sec) in completion of the three actions on the smaller image, and 196% speedup on the larger image (52 sec versus 102 sec), respectively.

Discussion

Although GPUs have been used in several neuroscience fields including neural network simulations and high speed imaging (Nageswaran et al., 2009; Baladron et al., 2012), our work addresses the GPU application in neural circuit mapping and electrophysiology-based data processing. To our best knowledge, this is the first demonstration in this subfield of neuroscience. In addition, we extend previous studies by presenting a comparison of numerical accuracy between GPU and CPU computation to verify the precision of GPU computation. This is an important aspect of GPU application, but has not been rigorously tested before.

We utilize GPU and CPU co-processing to speed up large-scale neural circuit mapping data analysis, taking LSPS mapping data analysis as an example. A GPU-enabled desktop computer system was designed and assembled toward this purpose. We described GPU-oriented program considerations, and presented the algorithms for

`

integrating GPU processing with detailed flow-chart diagrams of the implementation for an accelerated version of the synaptic event detection program. Our results indicate that cost-effective GPU computation facilitates large-scale data with increased speeds and with unaltered accuracy. In addition, we showed that even a high-end consumer-grade GPU is capable of speeding up Adobe Photoshop's performance by 50-90%, depending on the operations and the image sizes.

Compared with CPUs, the newest GPUs have an order of magnitude higher computation power and memory bandwidth. However, GPUs are designed as special-purpose co-processors and their programming interfaces are harder to use than those on the CPUs. Although GPU manufacturers and other organizations have developed various development kits that allows users with programming knowledge of high-level languages to take control of many stream processors of a GPU, it still requires steep learning to understand the GPU programming paradigm, data structure and complex optimization rules.   As Matlab is a commonly used mathematical programming suite and its new parallel computing toolbox contains many functions that support GPU-enabled computing, we chose to use Matlab as a computing platform. We modified the existing Matlab programs to utilize GPU computation with merely three basic steps: 1) transfer data to the GPU, 2) compute and 3) gather results. As the GPU on-board memory limits the capabilities of processing large volumes of data, preprocessing data with CPUs is necessary. However, the efficiency may be significantly hampered by the relative high-latency of the data exchange between CPUs and GPUs. Therefore we optimize the Matlab GPU program and follow the rule of "Communicate less, compute more". For our synaptic event detection program, the GPU takes over the intensive

`

computation load from the CPU and returns the results in a quick and accurate manner

to the system memory (with a 5x speed increase) for further CPU processing. In

addition, as Matlab-derived CUDA code is suboptimal and can be further improved, we

plan to re-write the Matlab GPU kernel in CUDA code and then have it run in the Matlab

environment. Such an approach could achieve a balance between execution efficiency

and code re-writing effort.

Figure 4.6
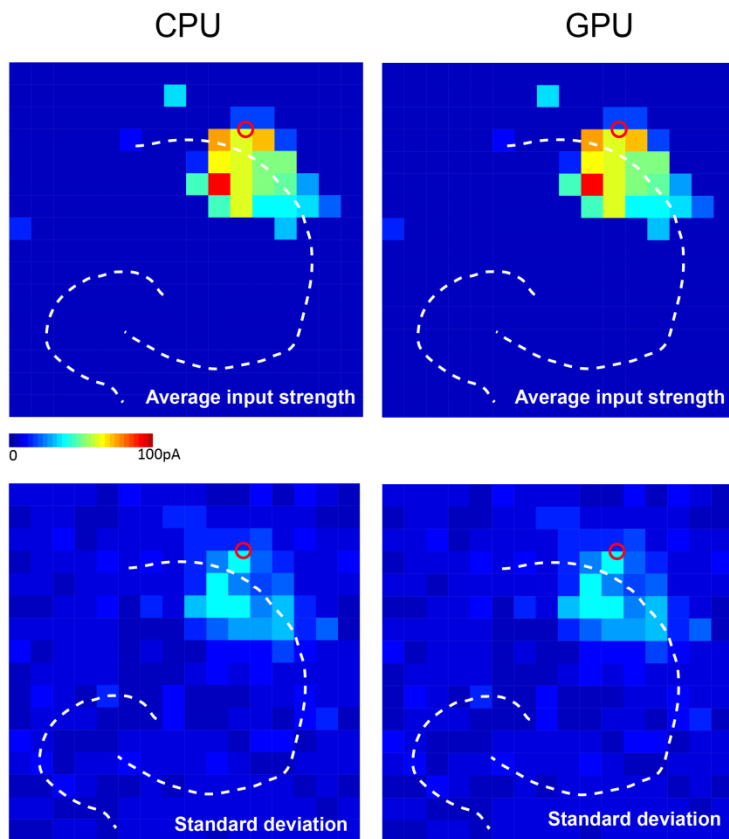
Figure 4.6. Visualization of the final detected events by using CPU and GPU-enable computation via the "Synaptic Event Detection" program. A-B, Color-coded maps of average input strength to the recorded cell, based on the detected EPSC events using CPU and GPU-enable computation, respectively. Warm colors indicate stronger excitatory synaptic input from the photostimulation sites. The averaged map was constructed with 8 raw data maps as shown in Figure 2B. C-D, The standard deviation maps of input strength across the 8 raw maps. These map results are identical.

`

Although we focus on data analysis of synaptic event data sets derived from LSPS experiments, the performance gain enabled by GPU computation should be likely extended to data analysis of multiple electrode array (MEA) recordings and large-scale single cell resolution calcium imaging experiments (Ohki et al., 2005; Nauhaus et al., 2008; Franke et al., 2012). MEA and bulk loading calcium imaging techniques offer the possibility to simultaneously record from large numbers of neurons (e.g., up to several thousand neurons) with relative ease, but at the expenses of increased efforts to detect and extract single neuronal activities from the recorded ensembles. Their data processing that requires intensive computation for spike sorting and calcium transient event detection can be similarly accelerated with GPUs using the algorithms outlined in this paper. Furthermore, while the speed-up and accuracy demonstrated in the present study using the particular LSPS data analysis leads the GPU to be considerable for electrophysiology-based neural circuit mapping, GPU-enabled desktop computer systems will be potentially essential for real-time closed-loop experiments, with the potential for running data analysis in real time while collecting data from technically challenging, large scale recordings. Furthermore, GPU-enabled desktop computer systems will facilitate real-time closed-loop experiments, with the potential for running data analysis in real time while collecting data from technically challenging recordings. In addition, we record from rare types of neurons and we would like to maximize the number of different protocols carried out for each recording. One limitation is that we only estimate when we have data sufficient for achieving required statistical power for any given protocol. Ideally if we could confirm such statistical thresholds by concurrent

131

`

real time analysis enabled by the GPU system, we could maximize the amount of data extracted from a given recording.

In conclusion, we believe that when appropriately applied, affordable GPU-enabled computation is efficient and powerful. Thus we advocate for its wider applications in neuroscience research.

Chapter 5:
Conclusion and future directions

My dissertation studies investigated the global spontaneous activity and their

underlying developing circuits in hippocampus. In Chapter 1, we reported a global

spontaneous network activity, which we termed GNA based on its global network

activation and propagation observed through VSD imaging. GNA normally initiates from

distal CA3 and propagates bi-directionally to DG and CA1. The events appear robustly

from P2 and the frequency reaches peak at around P5-6 and disappeared beyond P18.

Both duration and peak amplitude of each occurrence decrease as mouse aging.

However, the propagation speed increases with aging. The adult-like pattern of

unidirectional circuit propagation from DG to CA3 to CA1 appears at about 2 weeks.

Local field potential recording indicated that GNA is closely correlated with neuronal

ensemble behavior in local circuits. However, single-cell recording indicates GDPs are

not coupled with GNA events. Unlike the GDPs or SPWs recorded with other

techniques, mouse GNA cannot be blocked by GABA receptor antagonists. Instead we

observed a major contribution of AMPA receptor to both of initiation and propagation of

GNA. Mapping the development of local afferent input of CA3 pyramidal neurons and

DG granule cells over the time during which GNA is active reveals that weakening and

disappearance of bi-directional GNA concurs with the maturity of the trisynaptic circuitry,

i.e. formation of unidirectional information flow. The data support the hypothesis that

GNA in the developing hippocampus immediately precedes the unidirectional trisynaptic

circuit organization.

To further understand the underlying pathway for back-projection from CA3 to

DG in the developing hippocampus, we further investigated circuit connections of hilar

`

mossy cells, the only glutamatergic neuron type in the dentate hilus, during

hippocampal development. We identified significant developmental changes in local

excitatory and inhibitory inputs to mossy cells. Young mossy cells (P7) receive dominant

excitatory input from CA3 while mature mossy cells (p13-p14, p21-p28) receive

dominant excitatory input from DG. The inhibitory afferents to mossy cell reaches peak

at around p13-p14 and mature neurons receive more inhibiton than young mossy cells.

Similarly, DG provides the dominant inhibitory input. The developmental change of

mossy cell conforms to the disappearance of bi-directional propagation of GNA and

suggest that mossy cell is underlying pathway of CA3-Mossy Cell-DG backprojection

which might be masked by inhibition.

Although we investigated the spontaneous activity in developing hippocampus

and the development of underlying circuit, it is still not clear the function of spontaneous

activity to the formation of mature spontaneous circuits. Further manipulation technique

would be necessary to alter the spontaneous pattern so that we could gain some

insights on this matter. Moreover, the function of mossy cell is hippocampal system still

remains unclear. Further experiments using rabies tracing and optogenetics would be

helpful in mapping the cell type specific afferents input to and efferent from mossy cells.

If we could record from various hippocampal interneurons while stimulating mossy cells

selectively, we could better understand the 'recurrent network' formed between mossy

cells, granule cells and various hippocampal interneurons, thus helping understand the

role mossy cells in epileptogenesis.

To facilitate data processing and analysis for the large scale circuit mapping

studies (e.g., LSPS studies), we have developed a novel matched filtering technique

`

(Synaptic_Event_Detection software) that enables dependable automatic detection of synaptic events with minimal human supervision. The current technique has overcome the limitations of previously described threshold and template comparison techniques in detection of complex evoked synaptic signals with variable amplitudes and superimposed events. Our approach greatly improved the accuracy and efficiency in processing neural circuit mapping and electrophysiology-based data. The sensitivity and specificity of the method were evaluated on both simulated and experimental data, with its performance comparable to that of visual event detection performed by human operators. In addition, our technique has been further applied to the detection and analysis of inhibitory postsynaptic current (IPSC) responses. Further, we demonstrate how to use GPU to improve computation speed of the Matlab based Synaptic_Event_Detection software. We also present evidence of numerical accuracy, which again is not a given knowledge, due to changes in the code & very different hardware. Since Matlab is perhaps the most widely used programming platform for basic neuroscientists, we introduced a relatively simple yet effective Matlab-based approach to utilize GPU computation. We also take efforts to introduce how to assemble a GPU-enabled desktop computer system with detailed hardware and software information.

Our software can be modified to further apply to detection of other electrophysiological events such as extracellular action potentials, and event-related local field and electroencephalogram potentials as well as optical imaging signals. Clearly, the application of our technique to other domains will require modifications, including the design of an appropriate filter bank and adjustment of sensitivity/specificity

`

thresholds. These modifications, however, are rather easy to implement using our user-friendly software. To obtain better speed up of our GPU program, we can also re-write the Matlab GPU kernel in CUDA code and then have it run in the Matlab environment. Such an approach could avoid running inefficient Matlab code and achieve a balance between execution efficiency and code re-writing effort.

`

Reference

Abdul-Ghani MA, Valiante TA, Pennefather PS (1996) Sr2+ and quantal events at excitatory synapses between mouse hippocampal neurons in culture. J Physiol 495 (Pt 1):113-125.

Aguado JM, Ramos JM, Garcia-Corbeira P, Ales JM, Fernandez-Guerrero ML, Soriano F (1994) [The clinical spectrum of focal infection due to nontyphoid Salmonella: 32 years' experience]. Medicina clinica 103:293-298.

Amaral DG (1978) A Golgi study of cell types in the hilar region of the hippocampus in the rat. J Comp Neurol 182:851-914.

Arias FJ, Rojo MA, Ferreras JM, Iglesias R, Munoz R, Soriano F, Mendez E, Barbieri L, Girbes T (1994) Isolation and characterization of two new N-glycosidase type-1 ribosome-inactivating proteins, unrelated in amino-acid sequence, from Petrocoptis species. Planta 194:487-491.

Atouf F, Tazi A, Polak M, Czernichow P, Scharfmann R (1995) Dexamethasone regulates the expression of neuronal properties of a rat insulinoma cell line. Journal of neuroendocrinology 7:957-964.

Bankman IN, Johnson KO, Schneider W (1993) Optimal detection, classification, and superposition resolution in neural waveform recordings. IEEE Trans Biomed Eng 40:836-841.

Beggs HE, Soriano P, Maness PF (1994) NCAM-dependent neurite outgrowth is inhibited in neurons from Fyn-minus mice. The Journal of cell biology 127:825-833.

Behrens CJ, van den Boom LP, de Hoz L, Friedman A, Heinemann U (2005) Induction of sharp wave-ripple complexes in vitro and reorganization of hippocampal networks. Nat Neurosci 8:1560-1567.

Ben-Ari Y (2002) Excitatory actions of gaba during development: the nature of the nurture. Nat Rev Neurosci 3:728-739.

Ben-Ari Y, Cherubini E, Corradetti R, Gaiarsa JL (1989) Giant synaptic potentials in immature rat CA3 hippocampal neurones. J Physiol 416:303-325.

Ben-Ari Y, Gaiarsa JL, Tyzio R, Khazipov R (2007) GABA: a pioneer transmitter that excites immature neurons and generates primitive oscillations. Physiol Rev 87:1215-1284.

Ben-Ari Y, Khazipov R, Leinekugel X, Caillard O, Gaiarsa JL (1997) GABAA, NMDA and AMPA receptors: a developmentally regulated 'menage a trois'. Trends Neurosci 20:523-529.

Benitez R, Nenadic Z (2008) Robust unsupervised detection of action potentials with probabilistic models. IEEE Trans Biomed Eng 55:1344-1354.

Bischofberger J, Engel D, Li L, Geiger JR, Jonas P (2006) Patch-clamp recording from mossy fiber terminals in hippocampal slices. Nat Protoc 1:2075-2081.

Bolea S, Sanchez-Andres JV, Huang X, Wu JY (2006) Initiation and propagation of neuronal coactivation in the developing hippocampus. J Neurophysiol 95:552-561.

Bolea S, Avignone E, Berretta N, Sanchez-Andres JV, Cherubini E (1999) Glutamate controls the induction of GABA-mediated giant depolarizing potentials through AMPA receptors in neonatal rat hippocampal slices. J Neurophysiol 81:2095-2102.

Bonifazi P, Goldin M, Picardo MA, Jorquera I, Cattani A, Bianconi G, Represa A, Ben-Ari Y, Cossart R (2009) GABAergic hub neurons orchestrate synchrony in developing hippocampal networks. Science 326:1419-1424.

Bonnefond A, Sand O, Guerin B, Durand E, De Graeve F, Huyvaert M, Rachdi L, Kerr-Conte J, Pattou F, Vaxillaire M, Polak M, Scharfmann R, Czernichow P, Froguel P (2012) GATA6 inactivating mutations are associated with heart defects and, inconsistently, with pancreatic agenesis and diabetes. Diabetologia 55:2845-2847.

Bosco D, Soriano JV, Chanson M, Meda P (1994) Heterogeneity and contact-dependent regulation of amylase release by individual acinar cells. Journal of cellular physiology 160:378-388.

Bravo R, Soriano V (1994) [Diagnosis of perinatal infection by the human immunodeficiency virus]. Medicina clinica 102:575-577.

Brigman JL, Daut RA, Wright T, Gunduz-Cinar O, Graybeal C, Davis MI, Jiang Z, Saksida LM, Jinde S, Pease M, Bussey TJ, Lovinger DM, Nakazawa K, Holmes A (2013) GluN2B in corticostriatal circuits governs choice learning and choice shifting. Nat Neurosci 16:1101-1110.

Brivanlou IH, Dantzker JL, Stevens CF, Callaway EM (2004) Topographic specificity of functional connections from hippocampal CA3 to CA1. Proc Natl Acad Sci U S A 101:2560-2565.

Brotons B, Perez JA, Sanchez-Toril F, Soriano S, Hernandez J, Belenguer JL (1994) [The prevalence of chronic obstructive pulmonary disease and asthma. A cross-sectional study]. Archivos de

`

bronconeumologia 30:149-152.

Brustis JJ, Elamrani N, Balcerzak D, Safwate A, Soriano M, Poussard S, Cottin P, Ducastaing A (1994) Rat myoblast fusion requires exteriorized m-calpain activity. European journal of cell biology 64:320-327.

Buckmaster PS, Soltesz I (1996) Neurobiology of hippocampal interneurons: a workshop review. Hippocampus 6:330-339.

Buckmaster PS, Tam E, Schwartzkroin PA (1996) Electrophysiological correlates of seizure sensitivity in the dentate gyrus of epileptic juvenile and adult gerbils. J Neurophysiol 76:2169-2180.

Buckmaster PS, Wenzel HJ, Kunkel DD, Schwartzkroin PA (1996) Axon arbors and synaptic connections of hippocampal mossy cells in the rat in vivo. J Comp Neurol 366:271-292.

Buckmaster PS, Strowbridge BW, Kunkel DD, Schmiege DL, Schwartzkroin PA (1992) Mossy cell axonal projections to the dentate gyrus molecular layer in the rat hippocampal slice. Hippocampus 2:349-362.

Buhl DL, Buzsaki G (2005) Developmental emergence of hippocampal fast-field "ripple" oscillations in the behaving rat pups. Neuroscience 134:1423-1430.

Buzsaki G (1986) Hippocampal sharp waves: their origin and significance. Brain Res 398:242-252.

Callaway EM, Katz LC (1993) Photostimulation using caged glutamate reveals functional circuitry in living brain slices. Proc Natl Acad Sci U S A 90:7661-7665.

Carnoy C, Ramphal R, Scharfman A, Lo-Guidice JM, Houdret N, Klein A, Galabert C, Lamblin G, Roussel P (1993) Altered carbohydrate composition of salivary mucins from patients with cystic fibrosis and the adhesion of Pseudomonas aeruginosa. American journal of respiratory cell and molecular biology 9:323-334.

Chakraborty G, Magagna-Poveda A, Parratt C, Umans JG, MacLusky NJ, Scharfman HE (2012) Reduced hippocampal brain-derived neurotrophic factor (BDNF) in neonatal rats after prenatal exposure to propylthiouracil (PTU). Endocrinology 153:1311-1316.

Chen Z, Friedrich GA, Soriano P (1994) Transcriptional enhancer factor 1 disruption by a retroviral gene trap leads to heart defects and embryonic lethality in mice. Genes & development 8:2293-2301.

Chevaleyre V, Siegelbaum SA (2010) Strong CA2 pyramidal neuron synapses define a powerful disynaptic cortico-hippocampal loop. Neuron 66:560-572.

Chrobak JJ, Buzsaki G (1994) Selective activation of deep layer (V-VI) retrohippocampal cortical neurons during hippocampal sharp waves in the behaving rat. J Neurosci 14:6160-6170.

Clements JD, Bekkers JM (1997) Detection of spontaneous synaptic events with an optimally scaled template. Biophys J 73:220-229.

Cochran SL (1993) Algorithms for detection and measurement of spontaneous events. J Neurosci Methods 50:105-121.

Coleman MP, Buckmaster EA, Ogunkolade BW, Tarlton A, Lyon MF, Brown MC, Perry VH (1996) High-resolution mapping of the genes Kcnb3 and Ly63 on distal mouse chromosome 4. Mammalian genome : official journal of the International Mammalian Genome Society 7:552-553.

Csicsvari J, Hirase H, Mamiya A, Buzsaki G (2000) Ensemble patterns of hippocampal CA3-CA1 neurons during sharp wave-associated population events. Neuron 28:585-594.

Dantzker JL, Callaway EM (2000) Laminar sources of synaptic input to cortical inhibitory interneurons and pyramidal neurons. Nat Neurosci 3:701-707.

de Lecea L, Soriano E, Criado JR, Steffensen SC, Henriksen SJ, Sutcliffe JG (1994) Transcripts encoding a neural membrane CD26 peptidase-like protein are stimulated by synaptic activity. Brain research Molecular brain research 25:286-296.

del Rio JA, de Lecea L, Ferrer I, Soriano E (1994) The development of parvalbumin-immunoreactivity in the neocortex of the mouse. Brain research Developmental brain research 81:247-259.

Elexpuru A, Soriano M, Villalobo A (1994) Characterization of the epidermal growth factor receptor from Ehrlich ascites tumor cells. Biological chemistry Hoppe-Seyler 375:293-298.

Endean E, Toursarkissian B, Buckmaster M, Aziz S, Gellin G, Hill B (1996) Regulation of polyamine synthesis and transport by fibroblast growth factor in aortic smooth muscle cells. Growth factors 13:229-242.

Esteban J, Zapardiel J, Soriano F (1994) Two cases of soft-tissue infection caused by Arcanobacterium haemolyticum. Clinical infectious diseases : an official publication of the Infectious Diseases Society of America 18:835-836.

Esteban J, Cuenca-Estrella M, Ramos JM, Soriano F (1994) Granulomatous infection due to

`

Propionibacterium acnes mimicking malignant disease. European journal of clinical microbiology & infectious diseases : official publication of the European Society of Clinical Microbiology 13:1084.

Esteban J, Ramos JM, Fernandez-Guerrero ML, Soriano F (1994) Isolation of Nocardia sp. from blood cultures in a teaching hospital. Scandinavian journal of infectious diseases 26:693-696.

Fernandez Guerrero ML, Arbol F, Verdejo C, Fernandez Roblas R, Soriano F (1994) Treatment of experimental endocarditis due to penicillin-resistant Streptococcus pneumoniae. Antimicrobial agents and chemotherapy 38:1103-1106.

Filhoulaud G, Guillemain G, Scharfmann R (2009) The hexosamine biosynthesis pathway is essential for pancreatic beta cell development. The Journal of biological chemistry 284:24583-24594.

Frotscher M, Soriano E, Misgeld U (1994) Divergence of hippocampal mossy fibers. Synapse 16:148-160.

Gadea I, Ruiz P, Perez A, Gomez P, Soriano F (1994) Infectious mononucleosis due to herpes simplex virus type 1 in a child. European journal of clinical microbiology & infectious diseases : official publication of the European Society of Clinical Microbiology 13:520-521.

Galindez J, Soriano V, Gonzalez-Lahoz J (1994) [AIDS in the elderly]. Revista clinica espanola 194:138-139.

Gallego J, Soriano G, Zubieta JL, Delgado G, Villanueva JA (1994) Magnetic resonance angiography in meningovascular syphilis. Neuroradiology 36:208-209.

Garaschuk O, Hanse E, Konnerth A (1998) Developmental profile and synaptic origin of early network oscillations in the CA1 region of rat neonatal hippocampus. J Physiol 507 (Pt 1):219-236.

Garcia EJ, Delcan JL, Elizaga J, Abeytua M, Soriano J, Garcia Robles JA, Botas J, Lopez-Bescos L, Echeverria T, Beloscar A (1994) [Primary coronary angioplasty in acute anterior myocardial infarction: immediate results]. Revista espanola de cardiologia 47:40-46.

Garcia-Samaniego J, Soriano V, Soto J, Munoz F (1994) [Phenytoin hypersensitivity syndrome]. Anales de medicina interna 11:541-542.

Garcia-Samaniego J, Soriano V, Bravo R, Gonzalez-Lahoz J, Munoz F (1994) Viral replication in patients with multiple hepatitis virus infections. Gastroenterology 107:322-323.

Garcia-Samaniego J, Soriano V, Enriquez A, Lago M, Martinez ML, Muno F (1994) Hepatitis B and C virus infections among African immigrants in Spain. The American journal of gastroenterology 89:1918-1919.

Garcia-Samaniego J, Soriano V, Silva E, Enriquez A, Munoz F, Gonzalez-Lahoz J, Di Bisceglie A (1994) Significance of HCV RIBA-2 indeterminate results in high-risk individuals: assessment by a new third-generation RIBA assay and PCR. Vox sanguinis 66:148-149.

Gibson JR, Beierlein M, Connors BW (1999) Two networks of electrically coupled inhibitory neurons in neocortex. Nature 402:75-79.

Gil V, Belda J, Soriano JE, Munoz C, Martinez JL, Merino J (1994) [Validity of epidemiologic criteria in the detection of hypertension]. Revista clinica espanola 194:157-163.

Gil V, Munoz C, Martinez JL, Belda J, Soriano JE, Merino J (1994) [Factors involved in the hypertensive patient non-compliance with treatment]. Medicina clinica 102:50-53.

Gil-Benso R, Lopez-Gines C, Soriano P, Almenar S, Vazquez C, Llombart-Bosch A (1994) Cytogenetic study of angiosarcoma of the breast. Genes, chromosomes & cancer 10:210-212.

Giolli RA, Peterson GM, Ribak CE, McDonald HM, Blanks RH, Fallon JH (1985) GABAergic neurons comprise a major cell type in rodent visual relay nuclei: an immunocytochemical study of pretectal and accessory optic nuclei. Experimental brain research 61:194-203.

Gomez C, Gutierrez M, Martinez-Acacio P, Soriano V (1994) Evaluation of a new saliva collection device for HIV antibody screening purposes. Vox sanguinis 66:244.

Gomez-Tortosa E, Gadea I, Gegundez MI, Esteban A, Rabano J, Fernandez-Guerrero ML, Soriano F (1994) Development of myelopathy before herpes zoster rash in a patient with AIDS. Clinical infectious diseases : an official publication of the Infectious Diseases Society of America 18:810-812.

Gonzalez-Islas C, Wenner P (2006) Spontaneous network activity in the embryonic spinal cord regulates AMPAergic and GABAergic synaptic strength. Neuron 49:563-575.

Gorenstein C, Ribak CE (1985) Dendritic transport. II. Somatofugal movement of neuronal lysosomes induced by colchicine: evidence for a novel transport system in dendrites. J Neurosci 5:2018-2027.

`

Gorenstein C, Bundman MC, Lew PJ, Olds JL, Ribak CE (1985) Dendritic transport. I. Colchicine stimulates the transport of lysosomal enzymes from cell bodies to dendrites. J Neurosci 5:2009-2017.

Grove EA, Tole S (1999) Patterning events and specification signals in the developing hippocampus. Cereb Cortex 9:551-561.

Guelar A, Miro JM, Mallolas J, Zamora L, Cardenal C, Gatell JM, Soriano E (1994) [Therapeutic alternatives for cases of cerebral toxoplasmosis in patients with AIDS: clarithromycin and atovaquone]. Enfermedades infecciosas y microbiologia clinica 12:137-140.

Gutierrez M, Soriano V, Bravo R, Vallejo A, Gonzalez-Lahoz J (1994) Seroreversion in patients with end-stage HIV infection. Vox sanguinis 67:238-239.

Guy CT, Muthuswamy SK, Cardiff RD, Soriano P, Muller WJ (1994) Activation of the c-Src tyrosine kinase is required for the induction of mammary tumors in transgenic mice. Genes & development 8:23-32.

Hald J, Galbo T, Rescan C, Radzikowski L, Sprinkel AE, Heimberg H, Ahnfelt-Ronne J, Jensen J, Scharfmann R, Gradwohl G, Kaestner KH, Stoeckert C, Jr., Jensen JN, Madsen OD (2012) Pancreatic islet and progenitor cell surface markers with cell sorting potential. Diabetologia 55:154-165.

Harte-Hargrove LC, Maclusky NJ, Scharfman HE (2013) Brain-derived neurotrophic factor-estrogen interactions in the hippocampal mossy fiber pathway: implications for normal brain function and disease. Neuroscience 239:46-66.

Haumaitre C, Lenoir O, Scharfmann R (2009) Directing cell differentiation with small-molecule histone deacetylase inhibitors: the example of promoting pancreatic endocrine cells. Cell cycle 8:536-544.

Heinis M, Simon MT, Ilc K, Mazure NM, Pouyssegur J, Scharfmann R, Duvillie B (2010) Oxygen tension regulates pancreatic beta-cell differentiation through hypoxia-inducible factor 1alpha. Diabetes 59:662-669.

Heinis M, Soggia A, Bechetoille C, Simon MT, Peyssonnaux C, Rustin P, Scharfmann R, Duvillie B (2012) HIF1alpha and pancreatic beta-cell development. FASEB journal : official publication of the Federation of American Societies for Experimental Biology 26:2734-2742.

Heredia A, Hewlett IK, Soriano V, Epstein JS (1994) Idiopathic CD4+ T lymphocytopenia: a review and current perspective. Transfusion medicine reviews 8:223-231.

Heredia A, Muller J, Soriano V, Lee SF, Castro A, Pedreira J, Poffemberger KL, Epstein J, Hewlett IK (1994) Absence of evidence of retroviral infection in idiopathic CD4+ T-lymphocytopenia syndrome. Aids 8:267-268.

Hernandez-Garcia C, Soriano C, Morado C, Ramos P, Fernandez-Gutierrez B, Herrero M, Banares A, Jover JA (1994) Methotrexate treatment in the management of giant cell arteritis. Scandinavian journal of rheumatology 23:295-298.

Higashino-Matsui Y, Shirato K, Suzuki Y, Kawashima Y, Someya Y, Sato S, Shiraishi A, Jinde M, Matsumoto A, Ideno H, Tachiyashiki K, Imaizumi K (2012) Age-related effects of fasting on ketone body production during lipolysis in rats. Environmental health and preventive medicine 17:157-163.

Holowach J, Howe MC, Laatsch RH, McDougal DB, Jr. (1966) Effects of various anions and cations on the release of four dehydrogenases from brain mitochondria by a non-ionic detergent. Biochimica et biophysica acta 118:230-239.

Hsu M, Sik A, Gallyas F, Horvath Z, Buzsaki G (1994) Short-term and long-term changes in the postischemic hippocampus. Annals of the New York Academy of Sciences 743:121-139; discussion 139-140.

Hwang TN, Copenhagen DR (1999) Automatic detection, characterization, and discrimination of kinetically distinct spontaneous synaptic events. J Neurosci Methods 92:65-73.

Ignelzi MA, Jr., Miller DR, Soriano P, Maness PF (1994) Impaired neurite outgrowth of src-minus cerebellar neurons on the cell adhesion molecule L1. Neuron 12:873-884.

Ikrar T, Olivas ND, Shi Y, Xu X (2011) Mapping inhibitory neuronal circuits by laser scanning photostimulation. J Vis Exp:e3109.

Imamoto A, Soriano P, Stein PL (1994) Genetics of signal transduction: tales from the mouse. Current opinion in genetics & development 4:40-46.

Ishizuka N, Weber J, Amaral DG (1990) Organization of intrahippocampal projections originating from CA3 pyramidal cells in the rat. J Comp Neurol 295:580-623.

`

Jain P, Vig S, Datta M, Jindel D, Mathur AK, Mathur SK, Sharma A (2013) Systems biology approach reveals genome to phenome correlation in type 2 diabetes. PLoS One 8:e53522.

Javier Baladron DF, and Olivier Faugeras (2012) Three Applications of GPU Computing in Neuroscience. Comput Sci Eng 14:8.

Jin X, Prince DA, Huguenard JR (2006) Enhanced excitatory synaptic connectivity in layer v pyramidal neurons of chronically injured epileptogenic neocortex in rats. J Neurosci 26:4891-4900.

Jinde S, Zsiros V, Nakazawa K (2013) Hilar mossy cell circuitry controlling dentate granule cell excitability. Frontiers in neural circuits 7:14.

Jinde S, Zsiros V, Jiang Z, Nakao K, Pickel J, Kohno K, Belforte JE, Nakazawa K (2012) Hilar mossy cell degeneration causes transient dentate granule cell hyperexcitability and impaired pattern separation. Neuron 76:1189-1200.

Jindeel A, Narahara KA (2012) Nontraumatic amputation: incidence and cost analysis. The international journal of lower extremity wounds 11:177-179.

Jindeel A, Narahara KA (2013) Lower extremity amputation: a complete series from a tertiary hospital. The international journal of lower extremity wounds 12:322-323.

Kanaka-Gantenbein C, Dicou E, Czernichow P, Scharfmann R (1995) Presence of nerve growth factor and its receptors in an in vitro model of islet cell development: implication in normal islet morphogenesis. Endocrinology 136:3154-3162.

Kanaka-Gantenbein C, Tazi A, Czernichow P, Scharfmann R (1995) In vivo presence of the high affinity nerve growth factor receptor Trk-A in the rat pancreas: differential localization during pancreatic development. Endocrinology 136:761-769.

Kay SM (1998) Fundamentals of statistical signal processing: Detection theory. Englewood Cliffs, NJ: Prentice-Hall.

Kiefer F, Anhauser I, Soriano P, Aguzzi A, Courtneidge SA, Wagner EF (1994) Endothelial cell transformation by polyomavirus middle T antigen in mice lacking Src-related kinases. Current biology : CB 4:100-109.

Kultas-Ilinsky K, Ribak CE, Peterson GM, Oertel WH (1985) A description of the GABAergic neurons and axon terminals in the motor nuclei of the cat thalamus. J Neurosci 5:1346-1369.

Kunkel DD, Scharfman HE, Schmiege DL, Schwartzkroin PA (1993) Electron microscopy of intracellularly labeled neurons in the hippocampal slice preparation. Microscopy research and technique 24:67-84.

Laatsch RH, Cowan WM (1966) Electron microscopic studies of the dentate gyrus of the rat. I. Normal structure with special reference to synaptic organization. J Comp Neurol 128:359-395.

Laatsch RH, Cowan WM (1966) A structural specialization at nodes of Ranvier in the central nervous system. Nature 210:757-758.

Laguna F, Soriano V, Gonzalez-Lahoz JM (1994) Misdiagnosis of pancreatitis in patients receiving treatment with pentavalent antimonial agents. Clinical infectious diseases : an official publication of the Infectious Diseases Society of America 19:978-979.

Laguna F, Soriano V, Valencia E, Gonzalez-Lahoz JM (1994) [Gastrointestinal leishmaniasis in patients infected with the human immunodeficiency virus]. Revista clinica espanola 194:510-511.

Laguna F, Lopez-Velez R, Soriano V, Montilla P, Alvar J, Gonzalez-Lahoz JM (1994) Assessment of allopurinol plus meglumine antimoniate in the treatment of visceral leishmaniasis in patients infected with HIV. The Journal of infection 28:255-259.

Laguna F, Garcia-Samaniego J, Soriano V, Valencia E, Redondo C, Alonso MJ, Gonzalez-Lahoz JM (1994) Gastrointestinal leishmaniasis in human immunodeficiency virus-infected patients: report of five cases and review. Clinical infectious diseases : an official publication of the Infectious Diseases Society of America 19:48-53.

Lammers BP, Buckmaster DR, Heinrichs AJ (1996) A simple method for the analysis of particle sizes of forage and total mixed rations. Journal of dairy science 79:922-928.

Lamsa K, Palva JM, Ruusuvuori E, Kaila K, Taira T (2000) Synaptic GABA(A) activation inhibits AMPA-kainate receptor-mediated bursting in the newborn (P0-P2) rat hippocampus. J Neurophysiol 83:359-366.

Lee MG, Chrobak JJ, Sik A, Wiley RG, Buzsaki G (1994) Hippocampal theta activity following selective lesion of the septal cholinergic system. Neuroscience 62:1033-1047.

Lee H, Dvorak D, Kao HY, Duffy AM, Scharfman HE, Fenton AA (2012) Early cognitive experience prevents adult deficits in a neurodevelopmental schizophrenia model. Neuron 75:714-724.

`

Lein ES, Callaway EM, Albright TD, Gage FH (2005) Redefining the boundaries of the hippocampal CA2 subfield in the mouse using gene expression and 3-dimensional reconstruction. J Comp Neurol 485:1-10.

Leinekugel X, Khalilov I, Ben-Ari Y, Khazipov R (1998) Giant depolarizing potentials: the septal pole of the hippocampus paces the activity of the developing intact septohippocampal complex in vitro. J Neurosci 18:6349-6357.

Leinekugel X, Medina I, Khalilov I, Ben-Ari Y, Khazipov R (1997) Ca2+ oscillations mediated by the synergistic excitatory actions of GABA(A) and NMDA receptors in the neonatal hippocampus. Neuron 18:243-255.

Leinekugel X, Khazipov R, Cannon R, Hirase H, Ben-Ari Y, Buzsaki G (2002) Correlated bursts of activity in the neonatal hippocampus in vivo. Science 296:2049-2052.

Li GH, Jackson MF, MacDonald JF (2007) Weighted least squares fitting with multiple templates for detection of small spontaneous signals. J Neurosci Methods 164:139-148.

Li XG, Somogyi P, Ylinen A, Buzsaki G (1994) The hippocampal CA3 network: an in vivo intracellular labeling study. J Comp Neurol 339:181-208.

Liao D, Jones A, Malinow R (1992) Direct measurement of quantal changes underlying long-term potentiation in CA1 hippocampus. Neuron 9:1089-1097.

Linke R, Soriano E, Frotscher M (1994) Transient dendritic appendages on differentiating septohippocampal neurons are not the sites of synaptogenesis. Brain research Developmental brain research 83:67-78.

Logigian EL, Wolinsky JS, Soriano SG, Madsen JR, Scott RM (1994) H reflex studies in cerebral palsy patients undergoing partial dorsal rhizotomy. Muscle & nerve 17:539-549.

Lowell CA, Soriano P, Varmus HE (1994) Functional overlap in the src gene family: inactivation of hck and fgr impairs natural immunity. Genes & development 8:387-398.

Lui SM, Soriano A, Cowan JA (1994) Electronic properties of the dissimilatory sulphite reductase from Desulfovibrio vulgaris (Hildenborough): comparative studies of optical spectra and relative reduction potentials for the [Fe4S4]-sirohaem prosthetic centres. The Biochemical journal 304 (Pt 2):441-447.

Maier N, Nimmrich V, Draguhn A (2003) Cellular and network mechanisms underlying spontaneous sharp wave-ripple complexes in mouse hippocampal slices. J Physiol 550:873-887.

McNamara JO, Scharfman HE (2012) Temporal Lobe Epilepsy and the BDNF Receptor, TrkB. In: Jasper's Basic Mechanisms of the Epilepsies, 4th Edition (Noebels JL, Avoli M, Rogawski MA, Olsen RW, Delgado-Escueta AV, eds). Bethesda (MD).

Meyer JH, Soriano JM, Janknecht P, Funk J (1994) [Results of cyclocryocoagulation]. Klinische Monatsblatter fur Augenheilkunde 205:14-18.

Miro JM, Buira E, Mallolas J, Gallart T, Moreno A, Zamora L, Vilella R, Gatell JM, Soriano E (1994) [CD4+ lymphocytes and opportunistic infections and neoplasms in patients with human immunodeficiency virus infection]. Medicina clinica 102:566-570.

Moran I et al. (2012) Human beta cell transcriptome analysis uncovers lncRNAs that are tissue-specific, dynamically regulated, and abnormally expressed in type 2 diabetes. Cell metabolism 16:435-448.

Moreno A, Mensa J, Almela M, Vilardell J, Navasa M, Claramonte J, Cruceta A, Serrano R, Garcia-Valdecasas JC, Soriano E, et al. (1994) [138 episodes of bacteremia or fungemia in patients with solid organ (renal or hepatic) transplantation]. Medicina clinica 103:161-164.

Myers CE, Scharfman HE (2009) A role for hilar cells in pattern separation in the dentate gyrus: a computational approach. Hippocampus 19:321-337.

Myers CE, Scharfman HE (2011) Pattern separation in the dentate gyrus: a role for the CA3 backprojection. Hippocampus 21:1190-1215.

Nagai T, Tada M, Kirihara K, Araki T, Jinde S, Kasai K (2013) Mismatch Negativity as a "Translatable" Brain Marker Toward Early Intervention for Psychosis: A Review. Frontiers in psychiatry 4:115.

Nageswaran JM, Dutt N, Krichmar JL, Nicolau A, Veidenbaum A (2009) Efficient Simulation of Large-Scale Spiking Neural Networks Using CUDA Graphics Processors. Ieee Ijcnn:3201-3208.

Nenadic Z, Burdick JW (2005) Spike detection using the continuous wavelet transform. IEEE Trans Biomed Eng 52:74-87.

Nenadic Z, Burdick JW (2006) A control algorithm for autonomous optimization of extracellular recordings. IEEE Trans Biomed Eng 53:941-955.

`

Nenadic Z, Ghosh B, Ulinski P (2000) Spatiotemporal dynamics in a model of turtle visual cortex. *Neurocomputing* 32-33:479-486.

Nenadic Z, Ghosh BK, Ulinski PS (2002) Modeling and estimation problems in the turtle visual cortex. IEEE Trans Biomed Eng 49:753-762.

Nenadic Z, Ghosh BK, Ulinski P (2003) Propagating waves in visual cortex: a large-scale model of turtle visual cortex. J Comput Neurosci 14:161-184.

Nicolson TJ et al. (2009) Insulin storage and glucose homeostasis in mice null for the granule zinc transporter ZnT8 and studies of the type 2 diabetes-associated variants. Diabetes 58:2070-2083.

Ochiishi T, Saitoh Y, Yukawa A, Saji M, Ren Y, Shirao T, Miyamoto H, Nakata H, Sekino Y (1999) High level of adenosine A1 receptor-like immunoreactivity in the CA2/CA3a region of the adult rat hippocampus. Neuroscience 93:955-967.

Ohki K, Chung S, Ch'ng YH, Kara P, Reid RC (2005) Functional imaging with cellular resolution reveals precise micro-architecture in visual cortex. Nature 433:597-603.

Oppenheim AV, Schafer RW (2009) Discrete-time signal processing, Third edition Edition. Upper Saddle River, NJ: Prentice-Hall, Inc.

Oriol A, Ribera JM, Hernandez A, Soriano V, Milla F, Feliu E (1994) Aplastic anemia after non-A, non-B, and non-C hepatitis. Haematologica 79:168-169.

Osusky R, Soriano D, Ye J, Ryan SJ (1994) Cytokine effect on fibronectin release by retinal pigment epithelial cells. Current eye research 13:569-574.

Paxinos G, Franklin KBJ (2001) The Mouse Brain in Stereotaxic Coordinates. San Diego, CA: Academic Press.

Peterson GM, Ribak CE, Oertel WH (1985) A regional increase in the number of hippocampal GABAergic neurons and terminals in the seizure-sensitive gerbil. Brain Res 340:384-389.

Plaja A, Vidal R, Soriano D, Bou X, Vendrell T, Mediano C, Pueyo JM, Labrana X, Sarret E (1994) Terminal deletion of 6p: report of a new case. Annales de genetique 37:196-199.

Planas AM, Soriano MA, Ferrer I, Rodriguez-Farre E (1994) Kainic acid inhibits protein amino acid incorporation in select rat brain regions. Neuroreport 5:2333-2336.

Planas AM, Soriano MA, Ferrer I, Rodriguez Farre E (1994) Regional expression of inducible heat shock protein-70 mRNA in the rat brain following administration of convulsant drugs. Brain research Molecular brain research 27:127-137.

Polak M, Scharfmann R, Seilheimer B, Eisenbarth G, Dressler D, Verma IM, Potter H (1993) Nerve growth factor induces neuron-like differentiation of an insulin-secreting pancreatic beta cell line. Proc Natl Acad Sci U S A 90:5781-5785.

Rachdi L, Aiello V, Duvillie B, Scharfmann R (2012) L-leucine alters pancreatic beta-cell differentiation and function via the mTor signaling pathway. Diabetes 61:409-417.

Ramos JM, Garcia-Corbeira P, Fernandez-Roblas R, Soriano F (1994) [Bacteremia caused by anaerobes: analysis of 131 episodes]. Enfermedades infecciosas y microbiologia clinica 12:9-16.

Ramos JM, Garcia-Corbeira P, Aguado JM, Arjona R, Ales JM, Soriano F (1994) Clinical significance of primary vs. secondary bacteremia due to nontyphoid Salmonella in patients without AIDS. Clinical infectious diseases : an official publication of the Infectious Diseases Society of America 19:777-780.

Ratzliff A, Howard AL, Santhakumar V, Osapay I, Soltesz I (2004) Rapid deletion of mossy cells does not result in a hyperexcitable dentate gyrus: implications for epileptogenesis. J Neurosci 24:2259-2269.

Ravassard P, Czernichow P, Scharfmann R (2012) [First immortalised cell lines phenotypically and functionally equivalent to human insulin-secreting pancreatic beta cells]. Medecine sciences : M/S 28:149-151.

Ravassard P, Emilie B-N, Hazhouz Y, Pechberty S, Mallet J, Czernichow P, Scharfmann R (2009) A new strategy to generate functional insulin-producing cell lines by somatic gene transfer into pancreatic progenitors. PLoS One 4:e4731.

Ribak CE (1985) Axon terminals of GABAergic chandelier cells are lost at epileptic foci. Brain Res 326:251-260.

Ribak E, Leibowitz E (1985) Shearing stellar interferometer. 1: Digital data analysis scheme. Applied optics 24:3088.

Ribak CE, Seress L, Amaral DG (1985) The development, ultrastructure and synaptic connections of the mossy cells of the dentate gyrus. Journal of neurocytology 14:835-857.

Ribak E, Leibowitz E, Hege EK (1985) Shearing stellar interferometer. 2: Optoelectronic phase-locked system. Applied optics 24:3094.

Ribak J, Hornung S, Kark J, Froom P, Wolfstein A, Ashkenazi IE (1985) The association of age, flying time, and aircraft type with hearing loss of aircrew in the Israeli Air Force. Aviation, space, and environmental medicine 56:322-327.

Roberts RC, Ribak CE, Oertel WH (1985) Increased numbers of GABAergic neurons occur in the inferior colliculus of an audiogenic model of genetic epilepsy. Brain Res 361:324-338.

Roberts RC, Kim HL, Ribak CE (1985) Increased numbers of neurons occur in the inferior colliculus of the young genetically epilepsy-prone rat. Brain Res 355:277-281.

Rojo MA, Arias FJ, Iglesias R, Ferreras JM, Munoz R, Escarmis C, Soriano F, Lopez-Fando J, Mendez E, Girbes T (1994) Cusativin, a new cytidine-specific ribonuclease accumulated in seeds of Cucumis sativus L. Planta 194:328-338.

Rovira N, Soriano ME, Planas JM (1994) Ontogenic and regional changes in kinetic constants of alpha-methyl-D-glucoside transport in chicken small intestine. Biochemical Society transactions 22:262S.

Ruiz MP, Soriano F (1994) [Clinical significance of bacteremia caused by streptococci of the viridans group]. Enfermedades infecciosas y microbiologia clinica 12:426-432.

Sadgrove MP, Laskowski A, Gray WP (2006) Examination of granule layer cell count, cell density, and single-pulse BrdU incorporation in rat organotypic hippocampal slice cultures with respect to culture medium, septotemporal position, and time in vitro. J Comp Neurol 497:397-415.

Saez MJ, de Frutos M, Martinez P, Soriano V (1994) Evaluation of a new fluorescence immunoassay for CD4+ and CD8+ T cell counts in clinical samples. Vox sanguinis 67:86-87.

Sakakibara E, Nishida T, Sugishita K, Jinde S, Inoue Y, Kasai K (2012) Acute psychosis during the postictal period in a patient with idiopathic generalized epilepsy: postictal psychosis or aggravation of schizophrenia? A case report and review of the literature. Epilepsy & behavior : E&B 24:373-376.

Sanchez-Vives MV, Nowak LG, McCormick DA (2000) Membrane mechanisms underlying contrast adaptation in cat area 17 in vivo. J Neurosci 20:4267-4285.

Sans M, Gatell JM, Rafel M, Mallolas J, Soriano E (1994) [Varicella pneumonia in adults infected by HIV-1. Presentation of 2 cases]. Enfermedades infecciosas y microbiologia clinica 12:26-30.

Scharfman HE (1993) Characteristics of spontaneous and evoked EPSPs recorded from dentate spiny hilar cells in rat hippocampal slices. J Neurophysiol 70:742-757.

Scharfman HE (1993) Activation of dentate hilar neurons by stimulation of the fimbria in rat hippocampal slices. Neuroscience letters 156:61-66.

Scharfman HE (1993) Spiny neurons of area CA3c in rat hippocampal slices have similar electrophysiological characteristics and synaptic responses despite morphological variation. Hippocampus 3:9-28.

Scharfman HE (1994) EPSPs of dentate gyrus granule cells during epileptiform bursts of dentate hilar "mossy" cells and area CA3 pyramidal cells in disinhibited rat hippocampal slices. J Neurosci 14:6041-6057.

Scharfman HE (1995) Electrophysiological evidence that dentate hilar mossy cells are excitatory and innervate both granule cells and interneurons. J Neurophysiol 74:179-194.

Scharfman HE (1995) Electrophysiological diversity of pyramidal-shaped neurons at the granule cell layer/hilus border of the rat dentate gyrus recorded in vitro. Hippocampus 5:287-305.

Scharfman HE (2007) The CA3 "backprojection" to the dentate gyrus. Prog Brain Res 163:627-637.

Scharfman HE (2012) "Untangling" Alzheimer's disease and epilepsy. Epilepsy currents / American Epilepsy Society 12:178-183.

Scharfman HE (2012) Alzheimer's disease and epilepsy: insight from animal models. Future neurology 7:177-192.

Scharfman HE, McCloskey DP (2009) Postnatal neurogenesis as a therapeutic target in temporal lobe epilepsy. Epilepsy research 85:150-161.

Scharfman HE, Myers CE (2012) Hilar mossy cells of the dentate gyrus: a historical perspective. Frontiers in neural circuits 6:106.

Scharfman HE, Pierce JP (2012) New insights into the role of hilar ectopic granule cells in the dentate gyrus based on quantitative anatomic analysis and three-dimensional reconstruction. Epilepsia 53 Suppl 1:109-115.

`

Scharfman A, Lamblin G, Roussel P (1995) Interactions between human respiratory mucins and pathogens. Biochemical Society transactions 23:836-839.

Scharfman WB, Rauch AE, Ferraris V, Burkart PT (1993) Treatment of a patient with factor IX deficiency (hemophilia B) with coronary bypass surgery. The Journal of thoracic and cardiovascular surgery 105:765-766.

Scharfman HE, Kramar EA, Luine V, Srivastava DP (2013) Introduction to 'steroid hormone actions in the CNS: the role of brain-derived neurotrophic factor (BDNF)'. Neuroscience 239:1-2.

Scharfman HE, Malthankar-Phatak GH, Friedman D, Pearce P, McCloskey DP, Harden CL, Maclusky NJ (2009) A rat model of epilepsy in women: a tool to study physiological interactions between endocrine systems and seizures. Endocrinology 150:4437-4442.

Scharfmann R, Rachdi L, Ravassard P (2013) Concise review: in search of unlimited sources of functional human pancreatic beta cells. Stem cells translational medicine 2:61-67.

Scharfmann R, Tazi A, Polak M, Kanaka C, Czernichow P (1993) Expression of functional nerve growth factor receptors in pancreatic beta-cell lines and fetal rat islets in primary culture. Diabetes 42:1829-1836.

Schwartzkroin PA, Buckmaster PS, Strowbridge BW, Kunkel DD, Owens J, Jr., Pokorny J (1996) Possible mechanisms of seizure-related cell damage in the dentate hilus. Epilepsy research Supplement 12:317-324.

Seress L (1977) The postnatal development of rat dentate gyrus and the effect of early thyroid hormone treatment. Anatomy and embryology 151:335-339.

Seress L, Ribak CE (1985) A combined Golgi-electron microscopic study of non-pyramidal neurons in the CA 1 area of the hippocampus. Journal of neurocytology 14:717-730.

Seress L, Ribak CE (1985) A substantial number of asymmetric axosomatic synapses is a characteristic of the granule cells of the hippocampal dentate gyrus. Neuroscience letters 56:21-26.

Shepherd GM, Svoboda K (2005) Laminar and columnar organization of ascending excitatory projections to layer 2/3 pyramidal neurons in rat barrel cortex. J Neurosci 25:5670-5679.

Shepherd GM, Stepanyants A, Bureau I, Chklovskii D, Svoboda K (2005) Geometric and functional organization of cortical circuits. Nat Neurosci 8:782-790.

Shi Y, Nenadic Z, Xu X (2010) Novel use of matched filtering for synaptic event detection and extraction. PLoS One 5:e15517.

Sik A, Ylinen A, Penttonen M, Buzsaki G (1994) Inhibitory CA1-CA3-hilar region feedback in the hippocampus. Science 265:1722-1724.

Silberberg G, Markram H (2007) Disynaptic inhibition between neocortical pyramidal cells mediated by Martinotti cells. Neuron 53:735-746.

Simonato M, Loscher W, Cole AJ, Dudek FE, Engel J, Jr., Kaminski RM, Loeb JA, Scharfman H, Staley KJ, Velisek L, Klitgaard H (2012) Finding a better drug for epilepsy: preclinical screening strategies and experimental trial design. Epilepsia 53:1860-1867.

Sipila ST, Huttu K, Soltesz I, Voipio J, Kaila K (2005) Depolarizing GABA acts on intrinsically bursting pyramidal neurons to drive giant depolarizing potentials in the immature hippocampus. J Neurosci 25:5280-5289.

Soggia A, Flosseau K, Ravassard P, Szinnai G, Scharfmann R, Guillemain G (2012) Activation of the transcription factor carbohydrate-responsive element-binding protein by glucose leads to increased pancreatic beta cell differentiation in rats. Diabetologia 55:2713-2722.

Soriano P (1994) Abnormal kidney development and hematological disorders in PDGF beta-receptor mutant mice. Genes & development 8:1888-1896.

Soriano R (1994) Syringe feeding: current clinical practice and recommendations. Geriatric nursing 15:85-87.

Soriano V, Garcia-Samaniego J (1994) [Therapy with interferon in HIV-infected patients with chronic viral hepatitis]. Revista clinica espanola 194:887-889.

Soriano F, Ponte C (1994) Use of amoxicillin/clavulanate for treatment of infections due to Yersinia enterocolitica. Clinical infectious diseases : an official publication of the Infectious Diseases Society of America 19:227.

Soriano E, Frotscher M (1994) Mossy cells of the rat fascia dentata are glutamate-immunoreactive. Hippocampus 4:65-69.

Soriano E, Whyte J, McHugh NJ (1994) Frequency and clinical associations of anti-chromo antibodies in connective tissue disease. Annals of the rheumatic diseases 53:666-670.

145

`

Soriano F, Zapardiel J, Ponte C (1994) Use of selective media for isolating Corynebacterium urealyticum from urine specimens. Journal of clinical microbiology 32:2630-2631.

Soriano V, Ordi J, Grau J (1994) Tests for HIV in lupus. The New England journal of medicine 331:881.

Soriano V, Gutierrez M, Bravo R (1994) [Serological diagnosis of HIV-1 infection]. Revista clinica espanola 194:558-567.

Soriano MA, Planas AM, Rodriguez-Farre E, Ferrer I (1994) Early 72-kDa heat shock protein induction in microglial cells following focal ischemia in the rat brain. Neuroscience letters 182:205-207.

Soriano V, Valencia E, Laguna F, Gonzalez-Lahoz J (1994) High morbidity and mortality associated with non-AIDS defining conditions in HIV-infected patients in Spain. Genitourinary medicine 70:355-356.

Soriano V, Gutierrez M, Tuset C, Calderon E (1994) [Htlv-I]. Revista clinica espanola 194:551-557.

Soriano E, Del Rio JA, Martinez A, Super H (1994) Organization of the embryonic and early postnatal murine hippocampus. I. Immunocytochemical characterization of neuronal populations in the subplate and marginal zone. J Comp Neurol 342:571-595.

Soriano V, Valencia E, Alba A, Gonzalez-Lahoz J (1994) [Xanthomonas maltophilia endocarditis in an AIDS patient]. Medicina clinica 102:399.

Soriano MA, Tortosa A, Planas AM, Rodriguez-Farre E, Ferrer I (1994) Induction of HSP70 mRNA and HSP70 protein in the hippocampus of the developing gerbil following transient forebrain ischemia. Brain Res 653:191-198.

Soriano SG, McManus ML, Sullivan LJ, Scott RM, Rockoff MA (1994) Doppler sensor placement during neurosurgical procedures for children in the prone position. Journal of neurosurgical anesthesiology 6:153-155.

Soriano F, Fernandez-Roblas R, Lopez JC, Garcia-Corbeira P, Aguilar L (1994) Comparative in-vitro activity of rufloxacin with five other antimicrobial agents against bacterial enteric pathogens. The Journal of antimicrobial chemotherapy 34:157-160.

Soriano V, Garcia-Samaniego J, Gutierrez M, Bravo R, Gonzalez-Lahoz J (1994) High morbidity and mortality of chronic viral liver disease in HIV-infected individuals in Spain. The Journal of infection 28:100-102.

Soriano V, Gutierrez M, Bravo R, Diaz F, Olivan J, Gonzalez-Lahoz J (1994) Severe myopathy in an injection drug user coinfected with human immunodeficiency virus type 1 and human T cell leukemia virus type II. Clinical infectious diseases : an official publication of the Infectious Diseases Society of America 19:350-351.

Soriano V, Gutierrez M, Heredia A, Bravo R, Hewlett I, Gonzalez-Lahoz J (1994) Evaluation of different supplementary assays for the confirmation of HIV-1 and HIV-2 infections. Vox sanguinis 66:82-83.

Soriano V, Dronda F, Gonzalez-Lopez A, Chaves F, Bravo R, Gutierrez M, Heredia A, Hewlett I (1994) HIV-1 causing AIDS and death in a seronegative individual. Vox sanguinis 67:410-411.

Soriano V, Bravo R, Samaniego JG, Gonzalez J, Odriozola PM, Arroyo E, Vicario JL, Castro A, Colmenero M, Carballo E, et al. (1994) CD4+ T-lymphocytopenia in HIV-infected patients receiving interferon therapy for chronic hepatitis C. HIV-Hepatitis Spanish Study Group. Aids 8:1621-1622.

Soto A, Zapardiel J, Soriano F (1994) Evaluation of API Coryne system for identifying coryneform bacteria. Journal of clinical pathology 47:756-759.

Stefan Eilemann AB, Marwan Abdellah, Juan Hernando, Maxim Makhinya, Renato Pajarola, and Felix Schürmann (2012) Parallel Rendering on Hybrid Multi-GPU Clusters. Eurographics Symposium on Parallel Graphics and Visualization:9.

Stein PL, Vogel H, Soriano P (1994) Combined deficiencies of Src, Fyn, and Yes tyrosine kinases in mutant mice. Genes & development 8:1999-2007.

Super H, Soriano E (1994) The organization of the embryonic and early postnatal murine hippocampus. II. Development of entorhinal, commissural, and septal connections studied with the lipophilic tracer DiI. J Comp Neurol 344:101-120.

Susanna R, Jr., Nicolela MT, Soriano DS, Carvalho C (1994) Automated perimetry: a study of the glaucoma hemifield test for the detection of early glaucomatous visual field loss. Journal of glaucoma 3:12-16.

Tan J, Soriano A, Lui SM, Cowan JA (1994) Functional expression and characterization of the assimilatory-type sulfite reductase from Desulfovibrio vulgaris (Hildenborough). Archives of

`

biochemistry and biophysics 312:516-523.

Tazi A, Czernichow P, Scharfmann R (1995) Similarities and discrepancies in the signaling pathway for nerve growth factor in an insulin producing cell line and a neural crest-derived cell line. Journal of neuroendocrinology 7:29-36.

Tole S, Christian C, Grove EA (1997) Early specification and autonomous development of cortical fields in the mouse hippocampus. Development 124:4959-4970.

Udaykumar, Heredia A, Soriano V, Bravo R, Epstein JS, Hewlett IK (1994) Enhanced diagnostic efficiency of the polymerase chain reaction by co-amplification of multiple regions of HIV-1 and HIV-2. Journal of virological methods 49:37-46.

Ung GM (2010) How to Build the Ultimate Gaming PC, Step by Step. In. maximumpc.com.

Valencia ME, Laguna F, Camacho J, Castejon A, Soriano V, Adrados M, Gonzalez Lahoz J (1994) [Serum activity of the lactate dehydrogenase enzyme in patients with human immunodeficiency virus infection]. Anales de medicina interna 11:580-583.

Valencia ME, Guinea J, Soriano V, Martinez ML, Moreno V, Laguna F, Enriquez A, Gonzalez Lahoz J (1994) [Study of 164 episodes of infectious endocarditis in drug addicts: comparison of HIV positive and negative patients]. Revista clinica espanola 194:535-539.

Vallejo A, Gutierrez M, Soriano V (1994) HTLV-I/II infection among immigrants to Spain. Vox sanguinis 67:79-80.

Villanueva C, Balanzo J, Torras X, Soriano G, Sainz S, Vilardell F (1994) Value of second-look endoscopy after injection therapy for bleeding peptic ulcer: a prospective and randomized trial. Gastrointestinal endoscopy 40:34-39.

Villanueva C, Martinez FJ, Torras X, Sainz S, Soriano G, Gonzalez D, Balanzo J (1994) [Nadolol as an adjuvant to sclerotherapy of esophageal varices for prevention of recurrent hemorrhaging]. Revista espanola de enfermedades digestivas : organo oficial de la Sociedad Espanola de Patologia Digestiva 86:499-504.

Weiler N, Wood L, Yu J, Solla SA, Shepherd GM (2008) Top-down laminar organization of the excitatory network in motor cortex. Nat Neurosci 11:360-366.

West JR, Nornes HO, Barnes CL, Bronfenbrenner M (1979) The cells of origin of the commissural afferents to the area dentata in the mouse. Brain Res 160:203-215.

Wilson JA (2011) Using General-Purpose Graphic Processing Units for BCI Systems. 33rd Annual International Conference of the IEEE EMBS:4.

Xie X, Hider RC, Smart TG (1994) Modulation of GABA-mediated synaptic transmission by endogenous zinc in the immature rat hippocampus in vitro. J Physiol 478 (Pt 1):75-86.

Xu X, Callaway EM (2009) Laminar specificity of functional input to distinct types of inhibitory cortical neurons. J Neurosci 29:70-85.

Xu X, Olivas ND, Levi R, Ikrar T, Nenadic Z (2010) High precision and fast functional mapping of cortical circuitry through a combination of voltage sensitive dye imaging and laser scanning photostimulation. J Neurophysiol 103.

Yang O, Cuccia D, Choi B (2011) Real-time blood flow visualization using the graphics processing unit. Journal of biomedical optics 16:016009.

Yoshimura Y, Callaway EM (2005) Fine-scale specificity of cortical networks depends on inhibitory cell type and connectivity. Nat Neurosci 8:1552-1559.

Yoshimura Y, Dantzker JL, Callaway EM (2005) Excitatory cortical neurons form fine-scale functional networks. Nature 433:868-873.

Zapardiel J, Nieto E, Gegundez MI, Gadea I, Soriano F (1994) Problems in minimum inhibitory concentration determinations in coryneform organisms. Comparison of an agar dilution and the Etest. Diagnostic microbiology and infectious disease 19:171-173.

Zertal-Zidani S, Busiah K, Edelman A, Polak M, Scharfmann R (2013) Small-molecule inhibitors of the cystic fibrosis transmembrane conductance regulator increase pancreatic endocrine cell development in rat and mouse. Diabetologia 56:330-339.

Zhuang Y, Soriano P, Weintraub H (1994) The helix-loop-helix gene E2A is required for B cell formation. Cell 79:875-884.